CHARACTERIZING THE MARTIAN ENVIRONMENT THROUGH SURFACE SPACECRAFT OBSERVATIONS

CHARISSA L. CAMPBELL

A DISSERTATION SUBMITTED TO
THE FACULTY OF GRADUATE STUDIES
IN PARTIAL FULFILMENT OF THE REQUIREMENTS
FOR THE DEGREE OF

DOCTOR OF PHILOSOPHY

GRADUATE PROGRAM IN PHYSICS & ASTRONOMY
YORK UNIVERSITY
TORONTO, ONTARIO

November 2023

Abstract

Over the course of a Mars Year (MY) atmospheric temperatures vary enough between the furthest (Aphelion) and closest (Perihelion) points in Mars' orbit due to an Earth-like obliquity and elliptical orbit, creating two distinct seasons. Aphelion has cooler temperatures and a cross-equatorial Hadley cell revealing equatorial water-ice clouds. Perihelion has warmer temperatures that support increased dust activity such as dust-devils or dust storms. These two seasons have been observed from orbit and surface, with surface vehicles crucially important for understanding surface-to-atmosphere interactions. Aerosols were examined for wind direction and speed using movies from the Mars Science Laboratory (MSL) rover and InSight lander due to their proximity. Similar Easterly wind directions during the Aphelion season for both landing sites helped pinpoint that observed aerosols were most likely aloft in the middle atmosphere, affected by the same large-scale circulation via Hadley cells. However, mission constraints such as power and data volume limit the amount of returnable data and the ability to fully understand these aerosols. Automated methods appear to show promising results based on an algorithm developed by a team from Curtin university and tested with known wind directions from MSL atmospheric movies. The Onboard Rover Cloud Algorithm (ORCA) could be used on future missions to significantly decrease data volume by simply returning a set of wind parameters without first downlinking images. To further expand low-cost options, an optical meteorological station was created based on the Phoenix Mars mission experiment that imaged the lidar beam shining within aerosols to calculate ice-water content. The Mars Atmospheric Panoramic camera and Laser Experiment (MAPLE) has a panoramic camera and multiple class 3R lasers to maximize returnable science in a minimal way. Field testing in dense fog in Newfoundland showed that MAPLE's lasers could detect fog decks up to 100 m above the camera during nighttime conditions. The lasers were unable to be resolved during the day, but a power calculation determined that all three lasers on MAPLE could be suitable for Martian polar conditions. Understanding the constraints of obtaining Martian atmospheric data enables low-cost options such as MAPLE to further our knowledge of these aerosols.

Acknowledgements

I would like to dedicate this dissertation to the people that have always been there for me and cheered me on while trying to complete a PhD, not only during a pandemic, but while also starting a family. To Ryan and Arthur, you are the greatest gifts to me and I dedicate everything to you and I am so excited to start our next Chapter together.

To Grandma Carol, even though it has been almost a decade since I last knew you, I know you are soaking up everything I have done and given me the energy to keep going even when it is hard. I still think about you every day and how proud you would be of me.

To Paga, you were correct, I did make it to Mars by using rover's eyes to capture the sky above. Every call we do always discusses the weather between the two sides of the country and now we can add our favourite planet as well, Mars.

To the current and past PVL crew, it has been amazing getting to know, befriend, rant and grow together as graduate students. Just remember to take it one day at a time and that it will all be worth it in the end!

Table of Contents

Abstract ii

Acknowledgements iii

Table of Contents iv

List of Tables vi

List of Figures viii

1 Introduction 1
- 1.1 The Martian Environment . . . 1
- 1.2 Surface Mars Missions . . . 9
- 1.3 Limitations of Current Surface Studies . . . 13
- 1.4 Dissertation Roadmap . . . 15

2 WD 17
- 2.1 Overview . . . 17
  - 2.1.1 The Mars Science Laboratory (MSL, Curiosity) Mission . . . 17
  - 2.1.2 The InSight Lander . . . 20
  - 2.1.3 Author Contribution . . . 24
- 2.2 Methods . . . 25
  - 2.2.1 The MSL Mission . . . 25
  - 2.2.2 The InSight Lander . . . 30
- 2.3 Results and Discussion . . . 34
  - 2.3.1 The MSL Mission . . . 34
  - 2.3.2 The InSight Lander . . . 45
  - 2.3.3 Comparison between MSL and InSight . . . 53
- 2.4 Conclusions . . . 56

3 ORCA 58
- 3.1 Overview . . . 58
  - 3.1.1 Author Contribution . . . 59
- 3.2 Methods . . . 60
  - 3.2.1 The Onboard Rover Cloud Algorithm (ORCA) . . . 60
  - 3.2.2 The Mars Science Laboratory (MSL) Mission Zenith Movie (ZM) Dataset . . . 62
  - 3.2.3 Applying the Algorithm to ZMs Acquired by MSL . . . 63
- 3.3 Results and Discussion . . . 64
  - 3.3.1 ORCA Wind Direction Results . . . 65
  - 3.3.2 ORCA Angular Wind Velocity Results . . . 68
  - 3.3.3 Investigating ORCA on a Sol-by-Sol Basis . . . 70

3.4 Conclusions . . . 75

4 MAPLE **77**
4.1 Overview . . . 77
4.1.1 Author Contribution . . . 79
4.2 Methods . . . 80
4.2.1 MAPLE Camera and Lasers . . . 80
4.2.2 Constructing Housing for MAPLE . . . 90
4.2.3 Argentia, Newfoundland Field Site . . . 95
4.3 Argentia, NL Field Testing Results and Discussion . . . 101
4.3.1 Field Testing - June 28, 2022 . . . 101
4.3.2 Field Testing - June 29, 2022 . . . 104
4.3.3 Field Testing - June 30, 2022 . . . 116
4.3.4 Field Testing - July 3, 2022 . . . 122
4.3.5 Field Testing - July 4, 2022 . . . 131
4.3.6 Applying to Other Planetary Bodies . . . 134
4.4 Conclusions . . . 137

5 Future Work **140**
5.1 Martian Aerosol Analysis with Surface Missions . . . 140
5.2 Investigating an Automated Analysis Approach for Aerosol Movement in Martian Surface Imagery . . . 141
5.3 Learning From Martian Surface Missions to Develop a Low-Cost Optical Meteorological Station 141

6 Conclusions **142**

Bibliography **146**

List of Tables

2.1 Wind Direction comparison between ZM observations and REMS measured winds during the Bagnold Dune campaign from (Newman et al., 2017). Figure numbers in the REMS Wind Direction column are referencing figures from Newman et al. (2017). 39
2.2 A table of the InSight and MSL movies that were taken on the same sol. Matches were made based on similar L_s values ($\pm 0.5^{\circ}$) 54

4.1 Specifications of the Basler camera acA4024-29uc, taken from BaslerAG (2023) 81
4.2 Spectral characteristics of the IR cut off filter for the Basler acA4024-29uc camera (BaslerAG, 2023). The IR cutoff is at 690 nm which means that lasers used by MAPLE cannot be higher than this wavelength. 82
4.3 Specifications of the Thorlabs visible lasers used with MAPLE for field site testing. 87
4.4 Table of calculated conversion values based on the power output and equation 4.1. 89
4.5 The original experimental matrix for the MAPLE NL field site. The orientation of the lasers in the Pelican case (see Figure 4.9) split the eight lasers into four on either side of the camera. Two class 3R and two class 2 were included on each side so to limit operations, two lasers (one from each side) were used at the same time. All four lasers from each class will be used for a run. An x in a laser column indicates that it should be on during that specific run number. A total of 10 frames will be taken for each run number. 98
4.6 Line-of-Sight results from the first field test day at the Argentia site. The class 3R lasers travelled further than the class 2. This is because the class 3R lasers have higher power. Therefore it would be better to use the higher powered lasers to ensure the furthest distance from MAPLE can be measured. 103
4.7 Experimental matrix for the impromptu nighttime experiments on June 29, 2022. Similar to Table 4.5, lasers with x indicate they were on for that particular run. The class 3R lasers were only used. 105
4.8 Table showing the parameters for the LWC equation (Eqn 4.10) 112
4.9 Experimental matrix used on June 30, 2022 for daytime experiments at the Argentia, NL fieldsite. To maximize the chance of seeing the lasers in the day, only the class 3R green and red laser were used as they had a higher spectral response for the Basler camera (Figure 4.2). Background images were also taken for image subtraction to attempt to pull out any visible laser in the imagery. Both 200 and 500 microsecond exposure times were used. 117
4.10 Experimental matrix for July 3, 2022 night experiments. Based on the success of June 29, 2022 measurements, more lasers were included in this matrix. 123
4.11 Experimental matrix for July 4 daytime Argentia field site experiment. Both up and side orientation was used and background images were taken for both (run 1 and 10). Only the class 3R lasers were used to maximize the power within the fog to try to capture any scattering in the images. 131
4.12 Background radiance as measured in the nighttime imagery on June 29, 2022. Since the lasers are visible in this imagery, these values can act as the background values in Equation 4.13 to measure the needed power for other planetary bodies or environments. 136

4.13 The needed power for varying environments to ensure the different coloured (red, green, blue) lasers are seen against the background. 136

List of Figures

1.1 The orbit of Mars split over 360°. Aphelion and Perihelion are noted as the furthest and closest point in orbit. Source de Météorologie Dynamique (2008) . . . 3
1.2 Diagram showcasing the circulation cells on Earth. Hugging the equator are the Hadley cells while Ferrel cells are in the subtropics. At the poles are the polar cells. Credit: Center for Multiscaling Modeling of Atmospheric Processes/Colorado State University . . . 5
1.3 Figure 12 from Haberle (1997) showcasing how the Hadley cells change on Mars when at equinox or solstice. . . . 6
1.4 Map of elevation from the Mars Orbiter Laser Altimeter (Smith et al., 2001). . . . 7
1.5 Figure 11.1 from Haberle et al. (2017) describing how water is transported throughout a MY. 10
1.6 NASA Mars missions including the most recent Perseverance mission. Only the Curiosity and Perseverance missions are operational at the time of this dissertation. Credit: NASA/JPL-Caltech . . . 11
1.7 Figure 1 from Whiteway et al. (2009) where Panel B indicates two cloud decks (<1km and 4km). These clouds would be within the PBL and thus the lidar is a useful instrument for characterizing this important part of the Martian atmosphere. . . . 12

2.1 Figure 2a from Anderson (2010) showcasing the topography of Gale crater. The landing ellipse for MSL is shown in the NW corner of the crater, with north at the top of the map. The difference in elevation between the north and south side of the crater could attributed to being right on Mars' dichotomy boundary. . . . 18
2.2 Figure 3d in Kloos et al. (2018) shows gravity waves observed by MSL on sol 1302. . . . 19
2.3 Figure 1 from Banerdt et al. (2020) showing InSight's location (star) versus other previous/current missions such as Spirit and MSL (Curiosity). InSight is located on the plains, just north of MSL. . . . 22
2.4 The InSight lander with its instruments. TWINS is labelled as Temperature/Wind Sensors and the two cameras are the Instrument Context Camera under the deck and the Instrument Deployment Camera on its arm. Credit: NASA/JPL-Caltech . . . 23
2.5 An example of water-ice clouds observed by the InSight lander. Taken by the Instrument Context Camera (ICC), aerosol movement can be seen in the top right of the image. Credit: NASA/JPL-Caltech . . . 24
2.6 Figure 3 from Maki et al. (2012) shows the location of the NCAMs on the Remote Sensing Mast (RSM). . . . 26
2.7 Figure 2 from Maki et al. (2012) where the spectral range of the NCAM is 600-800 nm. The NCAMs are black-and-white so only one wavelength is shown. . . . 27
2.8 An example of a Zenith Movie (ZM) taken on sol 1748 at 06:46 LTST. This is an example of a movie with strong, consistent water-ice cloud features. MFS processing helps bring out more features to analyze within the movie. . . . 29
2.9 Orientation of the cardinal directions (N = North, E = East, W = West, S = South) depending on the azimuthal direction of MSL. The orientation of the rover was noted per movie to ensure that the correct cardinal direction was represented in calculated wind directions. . . . 30

2.10 Figure 6 from Maki et al. (2018) describing the colour wavelength responsivity of the InSight cameras. The cameras work best with red light, which is best suited for Martian geological studies. Unfortunately, the best wavelength for this work would be blue, which is less responsive due to the decrease in quantum efficiency of the CCD in that colour (Maki et al., 2018). 31
2.11 Figure 1 of Maki et al. (2018) shows the location of the ICC and IDC on InSight. The IDC is located on InSight's arm allowing it to move. The ICC is mounted on its underside and has a fixed position. 32
2.12 Frames 1-4 of a twilight movie taken on sol 146. These frames have been cropped to only include the sky and processed using a non-adaptive ±10% stretch (Lemmon et al., personal communication). Aerosols can be seen moving from the left side of the frame to the right. The ICC has an azimuthal pointing of 180°, thus the perpendicular movement of the aerosols indicates an Easterly direction. 33
2.13 Results for the Aphelion season (L_s 0°-180°) split between AM (< 12:00 LTST) and PM (> 12:00 LTST). Easterly and Westerly winds were common in the morning (top) and predominate over north and south winds, but strong Easterly predominate over all other wind directions in our data in the afternoon (bottom). Wind velocities are shown by the colourbar which is based on 40 km altitude. 35
2.14 Results for the Perihelion season (L_s 180°-359°) split between AM (¡ 12:00 LTST) and PM (¿ 12:00 LTST). Winds were highly variable in both speed and direction in the morning (top), with somewhat more consistent wind speeds and direction, predominantly from the West in the afternoon (bottom). This change between Aphelion winds (from the East) could be due to changing Hadley cells between the seasons. Wind speeds are shown by the colourbar which is based on an assumed altitude of 40 km for every cloud deck. 36
2.15 Viudez REMS Results 40
2.16 MarsWRF results for time bins 06:00, 09:00, 15:00, 18:00 LMST for varying altitudes as a function of solar longitude. The lowest altitude represents REMS (1.5 meters) and describe how winds would behave near the surface. The three upper altitude levels corresponds to altitudes where clouds are often observed in models and in previous work (Campbell et al., 2020). 42
2.17 MarsWRF wind speed and direction results during AM timebins (each panel, above) as compared to ZM wind speed and direction results (each panel, below). The ZM winds were graphed in the same manner as the modelled results where the wind direction is represented by the direction of the arrow (up = North) and the length of the arrow is the speed of that wind observation. The ZM wind speed and direction arrows are combined from multiple MYs with the specific MY indicated by the colour of the arrow. 43
2.18 MarsWRF wind speed and direction results during PM timebins (each panel, above) as compared to ZM wind speed and direction results (each panel, below). These results are graphed in the same manner as Figure 2.17. 44
2.19 Results from InSight movies investigating aerosol movement. Top: The whole dataset with the wind direction results superimposed. Bottom: Only movies with wind directions are shown. The direction of the arrow represents the direction towards which the winds travelling, with an arrow pointing to the top meaning southerly winds is travelling towards the North. Wind directions were only recorded for InSight movies within the Aphelion season so the x-axis reflects that change. 47
2.20 InSight wind direction results in the form of a wind rose. Each circle within the rose represents the % of data that have that direction within the dataset. For example, 20% of the movies in this dataset have aerosols moving from the East, comparable to results from MSL from the Aphelion season. 48

2.21 Table 21 from Banfield, 2019 describing the operational flags used for the TWINS data. Wind data with Flags 2, 3, 4 and 5 were included in our TWINS analysis as it meant that both TWINS booms were operational and measuring winds at that time. 49
2.22 TWINS results from L_s 0°-90° shown in black with ICC results shown in red. 51
2.23 TWINS results from L_s 90°-180° shown in black with ICC results shown in red. 52
2.24 Results showcase MSL (blue) and InSight (grey). Results that are close in time on this diagram agree with each other, which indicate that MSL and InSight are observing aerosols driven by similar circulation dynamics. The arrows represent the direction towards which the winds are travelling, with up indicating aerosols travelling towards North. 55
2.25 Wind rose plot of InSight and MSL results in the same manner as previous wind rose plots. However, since wind speed was not deducible in InSight results the colours represent the MSL (blue) and InSight (grey) missions. Results compare well with one another, with SW winds predominating. 56

3.1 ORCA Pipeline 62
3.2 An example of a Zenith Movie (ZM) processed using the Mean-Frame Subtraction technique as discussed in Chapter 2.2.1. MFS processing helps bring out more features to analyze within the movie, which in this case is thin wispy clouds. A raw example can be seen in Figure 2.8. . 63
3.3 Results for automated wind direction (blue) vs manual wind direction (green). The automated error bars represent the standard deviation. The manual error bars are cited from Campbell et al. (2020) as ±5°. 65
3.4 Standard deviation of wind direction for every movie in the dataset. Left investigates patterns with time (LTST), Centre investigates patterns with solar longitude, and Right is the histogram. The y-axis is the standard deviation value, thus the maximum value the algorithm fluctuated by was 80°. The majority of the standard deviation values lie between 35° and 40° or 5° and 15°. 67
3.5 Similar to Figure 3.3, but for angular wind velocity. Error bars for manual results are cited from Campbell et al. (2020) while automated result error bars is the calculated standard deviation. 68
3.6 Similar to Figure 3.4, but for angular wind velocity. The maximum value the angular wind velocity could fluctuate is 0.28°/s, however, the majority of standard deviation for this parameter is lower than 0.02°/s. 70
3.7 Example on Sol 1924 that has strong, consistent cloud features. The algorithm was able to measure wind direction that matched manual results. A low standard deviation is associated with this example, meaning that the automated value did not change much per frame. This is apparent in both the wind direction and pixel distance results as the arrow doesn't change much between each frame. 71
3.8 Sol 310 showing how lighting changes affect the algorithm calculations. For the wind direction, the automated (mean) value matched with manual value but had a large standard deviation. For pixel distance, the algorithm did not match manual values and had a large standard deviation, especially in frames 3 and 5. Overall this indicates that the algorithm needs more training with these types of movies. 72
3.9 Sol 1743 is an example with a camera artifact that is common in ZMs. Both models fluctuated significantly, as shown by the varying direction or size between frames. Neither the wind direction nor the pixel distance matched with manual results, and both had high standard deviations. This high error indicates the algorithm must be trained more to ignore these artifacts 74

3.10 Sol 1216 is an example of multiple cloud decks viewed in the movie. They are moving opposite of each other, but the most prominent deck moves from the bottom right to the upper left. The algorithm appears to measure the pixel distance very well with low standard deviation, which could be due to both decks moving at the same rate. For the wind direction, the algorithm gets confused on which deck to follow and flips between each direction. More training is needed for the wind direction output. 75

4.1 An example of a frame taken with the Basler camera by previous post-doc Christina Smith. This was taken outside at York University when aerosols (clouds) were in the sky. 81
4.2 Spectral response to Basler camera acA4024-29uc (BaslerAG, 2023). The camera performs best with green colours, which is expected with a Bayer-filter camera that has two green filters versus one for blue and one for red. 82
4.3 An image of an aquarium as taken by the MAPLE camera. Gridded sheets with 10cm x 10cm squares were used to translate to a polar angle conversion of 14 pixels per polar angle. 83
4.4 The same image as Figure 4.3 but with a perfect circle overlaid to determine any distortion from the camera. Since the circle appears to follow similar lines within the grids, it was determined to be equiangular. 84
4.5 Figure from (Facts, 2023) describing the eye injury hazard for the different class lasers. We want MAPLE to be as safe as possible so class 2 and 3R will only be used because of their low hazard for eye injury. 86
4.6 An image of the inside of an integrating sphere as seen by the MAPLE camera. The green laser was used to output a consistent spectral radiance to determine how well the camera responds to this wavelength (550 nm). 88
4.7 The calculated conversion values when converting DN to spectral radiance. A range of wavelengths were included to determine how well the MAPLE camera characterizes visible wavelengths. 89
4.8 The yellow pelican case chosen for Newfoundland field site testing. Source: Pelican (2023) . . 90
4.9 Rough schematics created for MAPLE based on the pelican case, camera, lasers, batteries and the raspberry pi used to control the camera. Several aspects were considered, such as putting a screen for the raspberry pi on the outside of the case. However, not everything was included for the Newfoundland field site. 91
4.10 The setup for the camera and laser integration with the Pelican case. The camera would be mounted in the middle, with the lasers attached to the perpendicular parts. 92
4.11 *Left:* the size of the Thorlabs part that holds the laser mount was measured against the top of the case. *Right:* The three locations for the window were verified with the Thorlabs equipment inside the case to ensure they were the correct size. 93
4.12 *Left:* Polycarbonate windows were sized to the correct size of the two rectangular laser window location. The window for the camera was a panoramic camera case. The hole for this window was filed down to ensure a snug fit with the window. *Middle:* Caulking was used to glue and seal all three windows from the inside of the case. *Right:* Caulking was also applied to the outside of the case to better seal the system since MAPLE will be visiting a high humidity location. 93
4.13 A waterproof phone has been set up with a raspberry pi to act as a screen to control the camera. The Basler software has a linux-based option, allowing for camera parameters to be modified if need be. The blackbox with a circular image is an image taken with the Raspberry Pi and Basler camera. 94
4.14 A rough top-down view of the MAPLE components, the location of the Raspberry Pi and battery packs. The raspberry pi is in the lower right part of the case, with it's corresponding battery on the lower left part of the case. The batteries for all the lasers will be stacked in both the left and right upper parts of the case. 95

4.15 A map of the Argentia runway courtesy of WOOD PLC. This was used to convey to port authority where the lasers would be located with respect to port traffic. The black rectangle represents our starting point with the WOOD PLC truck and pylons would be used to mark down the runway. To avoid construction on the NE side of the port, the lasers could not point that way, but in the direction of the blue line. 97
4.16 The two orientations of MAPLE during field testing in Argentia, NL. *Top:* the up orientation has MAPLE pointing the camera and lasers up into the atmosphere. The goal would be the capture fog decks at heights above the camera, which should be measurable by the change in intensity of the lasers per distance. *Bottom:* the sideways orientation has MAPLE pointing the camera and lasers down the runway, through any fog on the surface. This orientation could capture visibility and how it changes with distance. 100
4.17 Exposure times of 50, 200, 500 and 1000 microseconds with the Basler camera on the first day at Argentia, NL. The class 3R laser is powered on for all four images but is not visible in the raw imagery. This daytime issue was noted for future experiments and the 200 microsecond and 500 microsecond exposure times were used for testing. 102
4.18 Fog on the night of June 29, 2022 as observed from the hotel room. Pictured is the Placentia lift bridge. The fog caused scattering from the lights, showing haziness. 104
4.19 Image showing the green laser taken by the MAPLE camera on June 29, 2022. Left shows the actual laser pointing up into the atmosphere while Right has the simulated laser overlaid onto the actual laser. 106
4.20 The class 3R red laser in use on June 29, 2022. The normalized intensity (bottom) is modelled as a function of distance from the camera based on the laser path in the top image. Light pollution from nearby light sources appears to affect distances near the camera and may need to be investigated further. 108
4.21 Similar to 4.20 but for the class 3R green laser. Light pollution does not affect the green laser as much. This could be due to minimal light pollution around the horizon near the start of the green laser. Fog decks were measured at 1 meter and 40 meter above the surface. The thick fog layer confirms the near-surface aerosol measured by the class 3R green laser. 109
4.22 Similar to 4.20, but for the class 3R blue laser. Light pollution slight affects results but not to the extent as the red laser in Figure 4.22. The blue laser measured similar cloud decks as the green laser (Figure 4.21). 110
4.23 Red laser LWC analysis with Spectral Radiance (a), Optical Depth (c), and Transmittance (d).113
4.24 Green laser LWC analysis with Spectral Radiance (a), Optical Depth (c), and Transmittance (d). 114
4.25 Blue laser LWC analysis with Spectral Radiance (a), Optical Depth (c), and Transmittance (d).115
4.26 Background images taken on June 30, 2022 at the Argentia, NL site. These would be Run 2 (bottom), 7 (top,left), and 8 (top,bottom) in Experimental matrix 4.9. 118
4.27 Raw (Left) and background-subtracted (Right) images for the runs laid out in Matrix 4.9. No laser beam was detected in this image which could be due to limited near-fog at this time. . . 118
4.28 Same as 4.27, but for side orientation. No laser beam was detected. 119
4.29 Same as 4.28, but with higher exposure (500 microseconds). Results continued to show null results on observing the laser within the subctracted image. 119
4.30 Same as 4.28, but with the class 3R red laser. Similar to the green laser, the red laser was unable to be detected with background subtraction. 120
4.31 Same as 4.30, with a higher exposure, which still does not show any laser in imagery. 120
4.32 An image captured at the end of the field test where fog can be seen further in the distance with peaks observed above. In comparison with Figure 4.33, the fog observed is over the Placentia bay. Thus, it could be of interest to investigate fog measurements over bodies of water as they hold onto fog longer throughout the day. 121

4.33 A google map overlay of the Argentia, NL field site to roughly determine where fog in Figure 4.32 is located. The blue star represents the field site, the orange triangle is the cranes, with fog most likely over the bay. 122
4.34 Top: The class 3R red laser being used during the night of July 3, 2022. Bottom: Normalized intensity as a function of distance from the camera is modelled based on the location of the laser in the top image. This night showed more noise compared to the June 29, 2022 experiments (Figure 4.20) and the laser was significantly less bright. The only change between the two days was the closing of the pelican case lid. 124
4.35 Similar to 4.34, but for the class 3R green laser. This example still had noise below 1 meter from the surface. A fog deck was measured 3 meters above MAPLE. 125
4.36 Similar to 4.34, but for the class 3R blue laser. Noise was still shown at altitudes close to the surface, yet a fog deck was still measureable at the same altitude as 4.35. 126
4.37 Red laser LWC analysis with Spectral Radiance (a), Optical Depth (c), and Transmittance (d). 128
4.38 Green laser LWC analysis with Spectral Radiance (a), Optical Depth (c), and Transmittance (d). 129
4.39 Blue laser LWC analysis with Spectral Radiance (a), Optical Depth (c), and Transmittance (d). 130
4.40 Background images taken in the Up and Side orientations for the July 4, 2022 Argentia daytime experiment. 132
4.41 Raw (Left) and background-subtracted (Right) images for the runs laid out in Matrix 4.11. No laser beam was detected in any of the subtracted images, but a faint laser point is noticeable in the middle of the green, subtracted image (top). This day was foggier than the rest indicating that more aerosols on top of more power could be the solution to daytime measurements. . . 133
4.42 Similar to 4.41, but for the side orientation. No laser beam or points were deduced in these imagery which could be due to limited aerosols and/or too low power for the lasers. 134

1 Introduction

1.1 The Martian Environment

The atmosphere of Mars has been studied by spacecraft both from the surface and from orbit to gain better insight on the seasonal and diurnal behaviour of the Martian environment. These spacecraft have described an environment that is very different from Earth in many ways. For instance, the atmosphere of Mars is extremely thin with an average surface pressure of 6.36 millibars (636 Pa) and is composed of CO_2 (95%), N_2 (2.6%), Ar_2 (1.9%), and O_2 (0.16%). Furthermore, unlike the Earth, the Martian atmosphere is in equilibrium with surface deposits. Cooler temperatures during winter pole are below the CO_2 frost point in the Martian atmosphere resulting in the deposition of CO_2 at the polar caps, through both direct deposition and snowfall. Alternatively, warmer temperatures during summer pole causes CO_2 sublimation at the polar caps. This process results in more than 25% of the atmospheric mass cycling through the polar caps each year (Tillman et al., 1993). Changes in pressure bear witness to this cycling, and the pressure observed at the surface can vary by more than 30% at some locations (e.g. Haberle et al. (2014)) over a Martian Year (MY). Pressure also varies on shorter timescales with a $> 10\%$ variation over a sol (Martian day) as reported by the Pathfinder rover at Ares Vallis (Schofield et al., 1997) and the Curiosity rover at the Gale Crater landing site (Gómez-Elvira et al., 2014).

However, Mars also shares similarities with Earth. For instance, a sol (Martian day) is 24 hours and 39 minutes, which is the most similar to Earth's out of any planet in our solar system. Mars also has an Earth-like obliquity of 25.2° which enables familiar summer and winter seasons. Without this axial tilt solar insolation would be directed towards the equatorial regions, with minimal energy at the poles. However,

for both Mars and Earth, insolation reaches different parts of the planet throughout a year causing seasons. Another factor to seasonal changes on a planet is through orbital eccentricity.

Orbital eccentricity describes the shape of a planetary orbit around its host star. In the case of Earth, its eccentricity is $e = 0.0167$ (Williams, 2024), which is closer to a circular orbit which occurs when $e = 0$. Therefore the closest (perihelion) and furthest (aphelion) points in Earth's orbit around the Sun only vary by 3% and thus the majority of seasonal changes on the Earth is driven by obliquity. On the other hand, Mars has a highly elliptical orbit with $e = 0.09$ (Williams, 2023), which has a more oval shape. This causes the perihelion and aphelion points of Mars' orbit to vary by 20% (Appelbaum and Flood, 1990) leading to more insolation being received by Mars during perihelion. This was found to increase atmospheric temperatures by 20-40 K during perihelion because of the 40% increase in solar insolation (Clancy et al., 1996, Haberle et al., 2017). Therefore, even though Earth's seasons are mainly affected by just obliquity, Mars has both the obliquity and eccentricity affecting its seasons, revealing very unique seasonal behaviours.

Seasonal descriptions on Mars are handled differently in comparison to Earth. A MY consists of 668.6 sols (de Météorologie Dynamique, 2008). It is customary within planetary science to enumerate individual MYs. For instance, year 1 began on April 11, 1955 (Clancy et al., 2000) and, at the time of writing this manuscript, it is currently MY 37. To keep track of time through an orbit, Martian scientists use Solar Longitude (L_s). The orbit is divided into 360° (Figure 1.1) where $L_s = 0°$ is northern spring, $L_s = 90°$ is northern summer, $L_s = 180°$ is northern fall and $L_s = 270°$ is northern winter (de Météorologie Dynamique, 2008). Aphelion occurs at $L_s = 71°$ near northern summer solstice and Perihelion occurs at $L_s = 251°$ near southern summer solstice. The high eccentricity of Mars' orbit means that the Perihelion and Aphelion points are 1.38 AU and 1.66 AU, respectively (Williams, 2023).

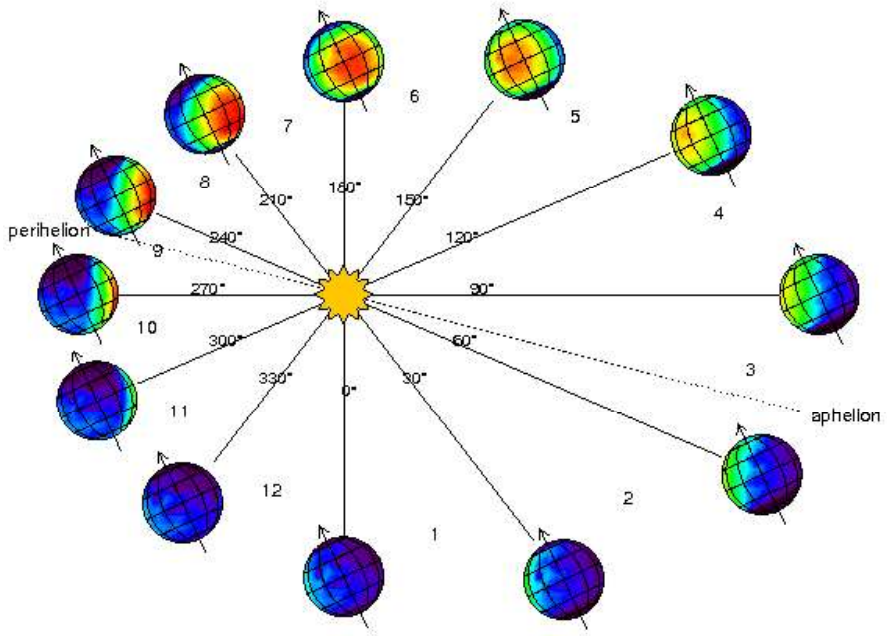

Figure 1.1: The orbit of Mars split over 360°. Aphelion and Perihelion are noted as the furthest and closest point in orbit. Source de Météorologie Dynamique (2008)

For those observing the atmosphere from the surface or from orbit, the year can be divided into two different seasons. Perihelion is warm, dusty and cloud-free while Aphelion is cool, cloudy and dust-free (Smith, 2004). The cooler Aphelion season occurs from L_s $45° - 150°$ and is often referred to as the Aphelion Cloud Belt (ACB) season as equatorial latitudes observe frequent cloud activity due to the atmospheric cooling (Clancy et al., 1996). The warmer Perihelion season occurs from L_s $180° - 300°$ and is known as the dusty storm season, when opacity and heating due to the dust typically reaches a maximum (Smith, 2004). Opacity describes how opaque or thin an atmosphere is based on various factors such as scattering due to aerosols within the atmosphere. This is determined based on how much light intensity reaches the surface of a planet based on the difference between the top of the atmosphere. This has been done on Mars from the surface (e.g. Lemmon et al. (2015), Lemmon et al. (2024)) by taking into account the Beer-Lambert law as shown in Equation 4.12 where τ is the optical depth/opacity and I is the incoming intensity/radiance from

the Sun. I_0 would be the flux at the top of the atmosphere before the light interacts with any aerosols. If the atmosphere has more aerosols, the light gets scattered and the flux gets diffused. An example of this would be rainbows within the sky due to light getting scattered through water droplets. In terms of Mars, the main aerosol that scatters light is from dust particles. Martian water-ice clouds in the atmosphere have only recently been observed to scatter incident intensity as seen by a halo by the Perseverance rover (Lemmon et al., 2022). By studying the two seasons on Mars, dust and cloud, we can study their respective aerosols in more detail such as aerosol wind movement or scattering within the atmosphere.

$$I_\lambda(x) = I_\lambda(0)e^{-\tau(x)} \tag{1.1}$$

While the ACB season is primarily driven by a broad atmospheric cooling due to Mars' distance from the sun, the clouds that form are enhanced by increased sublimation at the northern polar residual (or perennial) cap at the same time of the MY. Indeed, this asymmetry between the north and south Martian atmosphere was noted by Jakosky and Farmer (1982) where the northern hemisphere had up to twice as much water as the south based on water mapping by the Viking Orbiter Mars Atmospheric Water Detectors (MAWD) instrument. This pattern was confirmed by the Mars Global Surveyor (MGS) Thermal Emission Spectrometer (TES) that investigated the atmosphere for two MYs (Smith, 2004). The asymmetry in water vapour content was explained through warmer temperatures at Perihelion encouraging water transportation to the North while cooler temperatures at Aphelion favoured water saturation at equatorial locations, limiting how much water can be transported to the southern hemisphere (Clancy et al., 1996). This transport process is thought to be at least partially connected to the mirroring asymmetry between the northern and southern polar caps, though the difference in elevation, topography and atmospheric circulation also plays a significant role.

A similarity Mars shares with Earth is global atmospheric circulation. The high obliquity for both Earth and Mars causes the atmosphere to heat irregulary from the Sun, with equatorial locations warmer than the poles. Earth's thicker atmosphere and varying distribution of land and water limits the latitudinal size of Earth's circulation cells. As shown in Figure 1.2, three major cells (Hadley, Ferrel and Polar) are on either

side of the equator. Hadley cells are located against the equator and are responsible for moving the warmest air polewards. At the poles, a small circulation cell (Polar cell) circulates the cool air. In between exists the Ferrel cell which is driven by friction from both the Hadley and Polar cells. Winds within global circulation cells are affected by the rotation of the planet. As the Earth spins, the Coriolis force affects winds within the atmosphere, causing them to sway from their original rising position. For Earth, Easterly winds occur within the Hadley and Polar cells while Westerly winds are within the Ferrel cell (Figure 1.2).

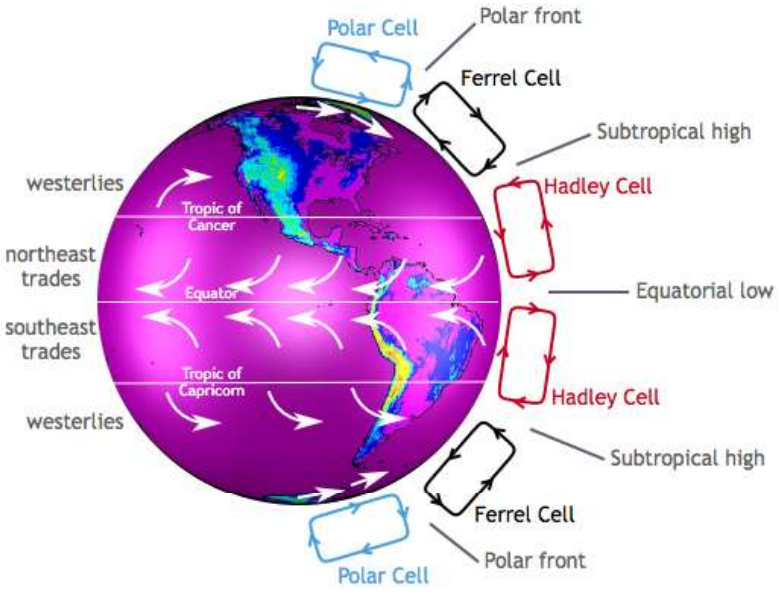

Figure 1.2: Diagram showcasing the circulation cells on Earth. Hugging the equator are the Hadley cells while Ferrel cells are in the subtropics. At the poles are the polar cells. Credit: Center for Multiscaling Modeling of Atmospheric Processes/Colorado State University

Similar atmospheric circulation do occur Mars, but the lack of ocean and Mars' small size changes the behaviour of the cells. Mars' Hadley cells have been modelled to become one large cross-equatorial cell during solstice with a brief period at equinox where two Hadley cells are modelled, similar to Earth (Haberle et al., 1993, Richardson and Wilson, 2002). This is shown in Figure 1.3. The single Hadley cell is not symmetric on the equator, with the rising branch in the centre of the Southern hemisphere in Perihelion and in the centre of the Northern hemisphere in Aphelion (Haberle et al., 2017). The direction of wind within circulation

cells is the same between Earth and Mars because of the similar rotational period (Haberle et al., 2017). Therefore Easterly winds are expected with the Martian cross-equatorial Hadley cell. The behaviour of the single cross-equatorial Hadley cell has been modelled to be twice as strong during Perihelion in comparison to Aphelion (Haberle et al., 1993, Richardson and Wilson, 2002). This is due to a variety of factors including higher solar insolation ($\tilde{4}0\%$ change) that creates a dust heating feedback loop and topographical differences between the Northern and Southern hemispheres (Haberle et al., 1993, Richardson and Wilson, 2002).

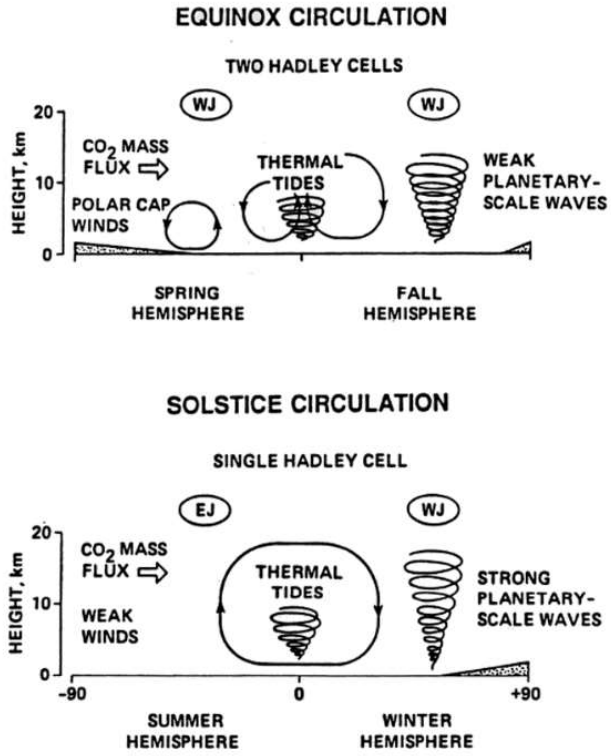

Figure 1.3: Figure 12 from Haberle (1997) showcasing how the Hadley cells change on Mars when at equinox or solstice.

The differences in elevation between the North and South hemisphere affects both local and global circulation. As shown in Figure 1.4, the Northern hemisphere is low in elevation and relatively crater free while the Southern hemisphere is higher in elevation with plenty of craters creating a hemispherical dichotomy. These higher elevations in the south leads to stronger circulation, similar to a heat source, which

is opposite to the north where the flat plains have suppressed circulation, similar to a heat sink, (Haberle et al., 2017). This difference in elevation affects the Planetary Boundary Layer (PBL), which represents the lowest part of the atmosphere (<10 km) where surface-atmosphere interactions occur.

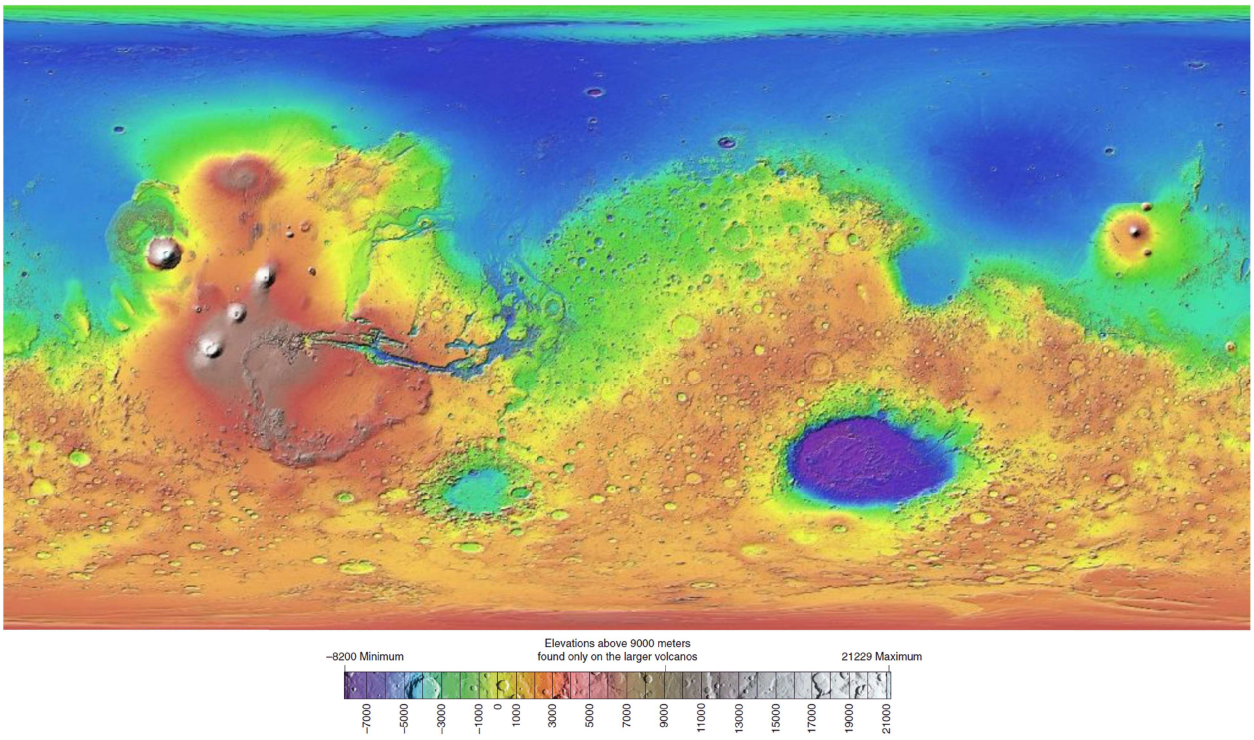

Figure 1.4: Map of elevation from the Mars Orbiter Laser Altimeter (Smith et al., 2001).

In comparison to the Earth's PBL, the Martian PBL is larger due to the thin atmosphere not suppressing its vertical extent. Martian daytime convection during Perihelion was investigated using the MGS orbiter and determined the PBL reached 8-10 km from the surface (Hinson et al., 1999). These altitudes for the PBL were more commonly seen in high plateaus (>8 km) but lower altitudes in the plains (5-6 km) (Haberle et al., 2017). During the night, the PBL is limited to the surface due to cooler temperatures (Haberle et al., 2017). Suppressed daytime PBLs have been observed in certain craters (e.g. Gale crater Rafkin et al. (2016)), which creates an enclosed local environment that are not as affected by large scale circulation. In these cases, aerosols within suppressed PBLs don't mix with aerosols above the crater, creating a dryer local environment. To better understand daytime convection and how the PBL interacts with the atmosphere,

dust activity such as dust-devils or dust storms can be observed.

Dust lifting mechanisms in the Martian atmosphere are caused by either dust-devils or surface winds. Dust devils are found on both Earth and Mars and are referred to as particle loaded convective vortices that are powered by solar insolation (Balme and Greeley, 2006). Compared to Earth, Martian dust devils can be an order of magnitude taller and wider with greater wind speeds, leading to speculation that they are the main mechanism for surface-to-atmosphere injection of dust (Balme and Greeley, 2006). Models have shown that Martian dust devils play a role in creating the background atmospheric dust haze (Kahre et al., 2006, Newman et al., 2002), but do not trigger dust storms despite their high frequency (Malin and Edgett, 2001, Thomas and Gierasch, 1985, Whelley and Greeley, 2008). Dust storm activity is classified based on size and can range through local, regional or planet-encircling dust storms (Cantor et al., 2001, Martin and Zurek, 1993). Planet-encircling can also be labelled as global and indicates a storm large enough to cover the entire planet, as seen in the MY25/2001 (Cantor, 2007), MY28/2007 and MY 34/2018 Global Dust Storms (GDS; (Guzewich et al., 2019)).

The behaviour of dust on Mars is also extremely useful for understanding the role of water in the Martian atmosphere. The majority of the water on Mars comes from the seasonal changes in the polar ice cap. As shown in Figure 1.5, the combination of cooler atmospheric temperatures and the single cross equatorial Hadley cell during Aphelion allows water-ice clouds to form at the equator. Tamppari et al. (2003) was able to prove this Hadley cell circulation based on water-ice cloud formation as viewed by the Viking Orbiter. Water-ice clouds can be observed over large geological formations (e.g. Tharsis region). These clouds are known as orographic and were observed at all times of a MY rather than just through the ACB season (Benson et al., 2003, Wang and Ingersoll, 2002). The diurnal patterns of Martian water-ice clouds have shown minimal change for orographic clouds (Benson et al., 2003), yet ACB clouds observed by Tamppari et al. (2003) had a distinct morning and afternoon pattern that seemed to be independent with each other. The morning clouds could be attributed to lower overnight atmospheric temperatures which then tapered off by midsol before increasing again by afternoon. This afternoon peak was attributed to the increase dust loading midsol, which then act as Cloud Condensation Nuclei (CCN) for the water-ice in the atmosphere to

condense on (Tamppari et al., 2003). This effectively removes the dust from the atmosphere (Clancy et al., 1996), which could be another reason why there is minimal dust activity during Aphelion versus Perihelion.

The unique seasons of aerosol activity on Mars has been extensively measured using orbiter spacecraft (e.g. Smith (2004)) for both the Aphelion (cloud) and Perihelion (dust). While orbiters are extremely useful for observing aerosols across all latitudes and longitudes and at all times of a MY, it can be challenging to observe near-surface altitudes. This limits orbiters to only observing altitudes > 10 km and arises because of occlusion by the terrain and as the result of high dust opacity along slant paths, especially for orbiters observing the limb (Kleinböhl et al., 2009). However, it is particularly critical to observe this lower part of the atmosphere since it is key to understanding surface-atmosphere interactions within the PBL. Therefore, surface missions that are in direct contact with the lower atmosphere, hold a key into understanding how aerosols behave in this important part of the atmosphere.

1.2 Surface Mars Missions

Not many surface missions have successfully landed and collected data from Mars which is shown in Figure 1.6. This is especially true for environmental studies as the majority of science done at Martian surface missions are geological heavy, limiting the number of observational points for the atmosphere. However, every surface planetary mission includes at least one camera to report the performance of the spacecraft or take imagery of nearby surroundings for scientific purposes. Nominally named engineering cameras, these cameras are also radiometrically calibrated to allow for scientific investigation of the nearby atmosphere (Maki et al., 2003). Thus, imagery from the surface could provide useful information ontop of any meteorological equipment already collecting near-surface atmospheric properties such as wind.

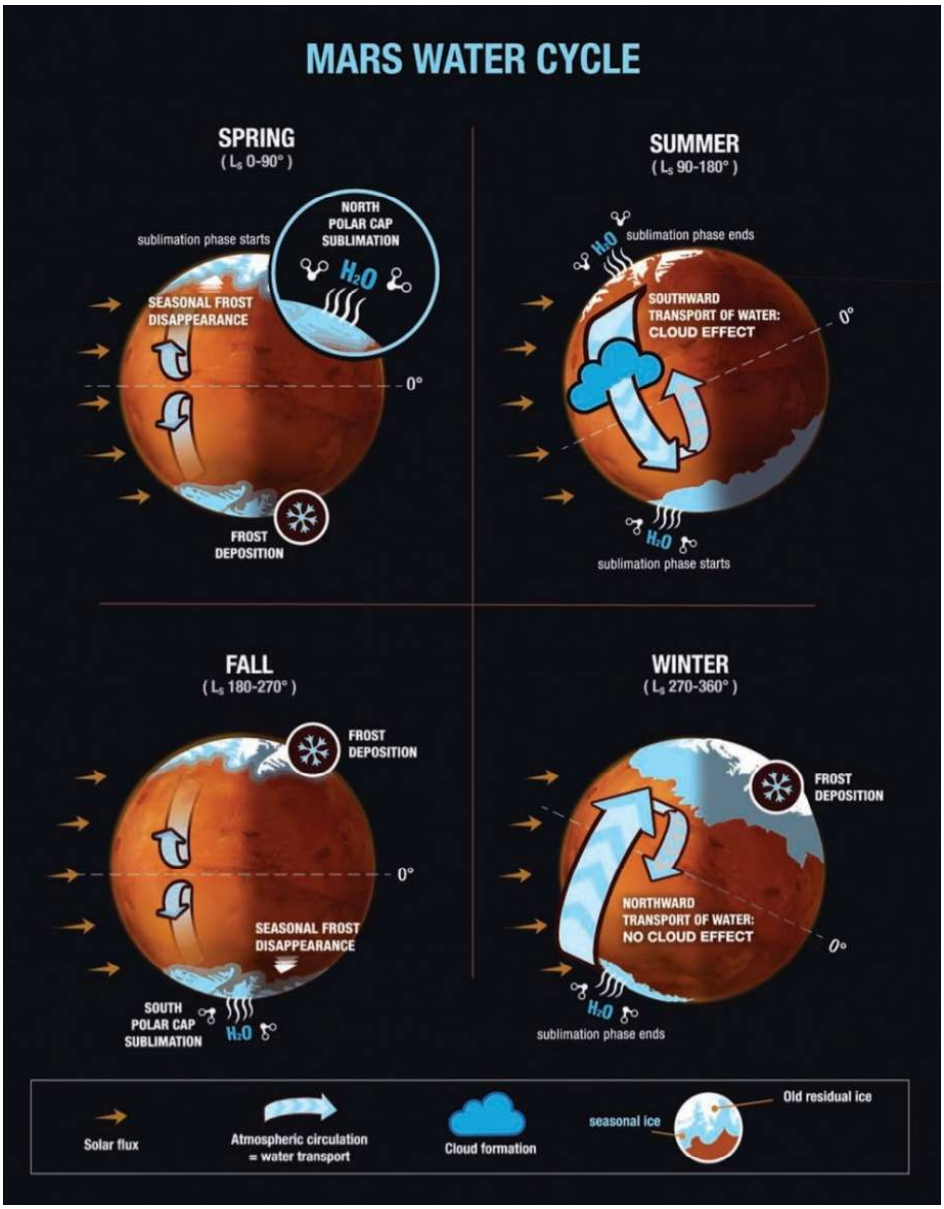

Figure 1.5: Figure 11.1 from Haberle et al. (2017) describing how water is transported throughout a MY.

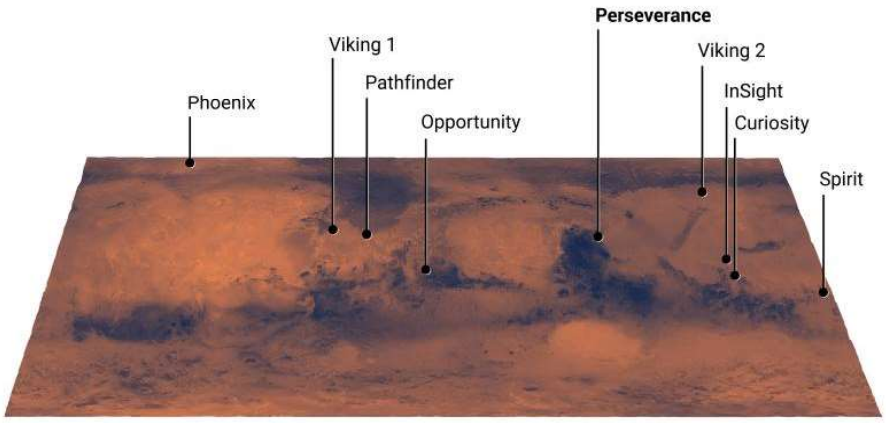

Figure 1.6: NASA Mars missions including the most recent Perseverance mission. Only the Curiosity and Perseverance missions are operational at the time of this dissertation. Credit: NASA/JPL-Caltech

One of the earliest Mars missions, Pathfinder, had an onboard meterological station but also used its camera to capture morning water-ice clouds (Schofield et al., 1997, Smith et al., 1997). Atmospheric opacity was measured through Pathfinder imagery by taking images of the sun (Smith et al., 1997), which has been a continued analysis on Mars using other missions (e.g. Wolfe and Lemmon (2023)). Using imagery for aerosols continued through missions such as the Mars Exploration Rovers (MER; Spirit and Opportunity) which introduced the Navigation Camera (NCAM) as not only an engineering based camera for drives, but it was also radiometrically calibrated for atmospheric studies (Maki et al., 2003). Over 5 MYs, Lemmon et al. (2015) utilized MER images to investigated aerosol activity per season. This agreed with previously seen results (e.g. Smith (2004)) that showed low dust but high water-ice cloud activity during Aphelion and high dust but low water-ice activity during Perihelion. The NCAM from MER became legacy hardware that had built-to-print copies for the Mars Science Laboratory (MSL, Curiosity) and InSight lander missions (Maki et al., 2012; 2018) and utilized flight space CCDs for the Phoenix lander mission (Lemmon et al., 2008).

The Phoenix lander mission was very important for Martian aerosol analysis due to its onboard lidar that captured the altitudes of water-ice clouds near the North polar cap. The lidar was in the green spectrum (532 nm) and returns a height profile based on scattering caused by overhead aerosols (Whiteway et al.,

2008). Results for this analysis are shown in Figure 1.7 where cloud decks were measured <1 km and 4 km in altitude. Adding to this, Moores et al. (2011) imaged the lidar beam while in use to estimate the ice-water content based on backscattering within the beam. Even though Phoenix was only operational for 157 sols, it provided useful information on near-surface aerosols, especially with the use of its onboard lidar.

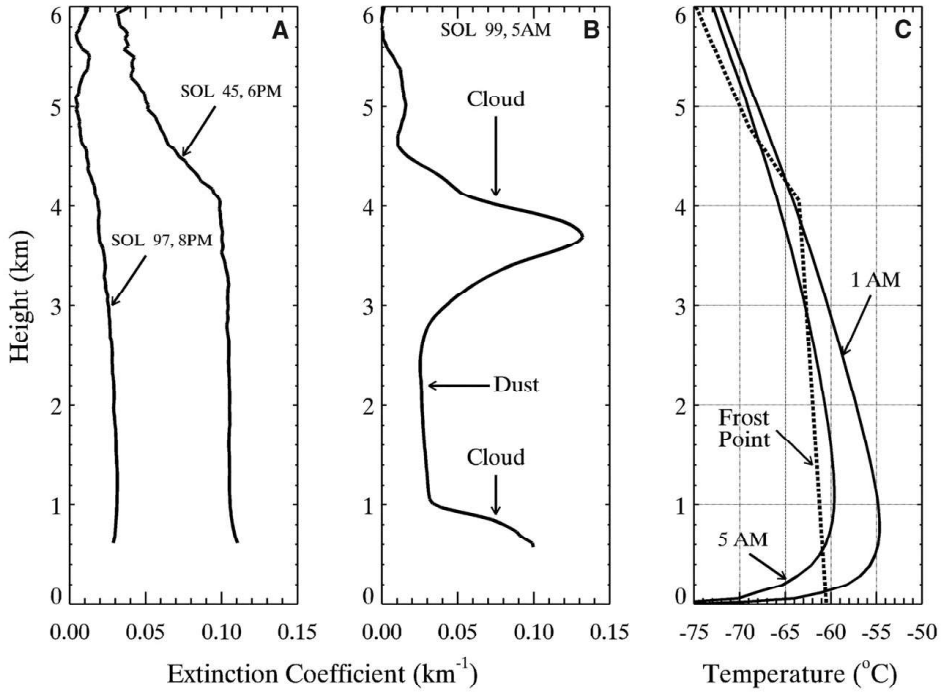

Figure 1.7: Figure 1 from Whiteway et al. (2009) where Panel B indicates two cloud decks (<1km and 4km). These clouds would be within the PBL and thus the lidar is a useful instrument for characterizing this important part of the Martian atmosphere.

Learning from the Phoenix mission, MSL utilized similar atmospheric movies to capture aerosol movement above its landing location, Gale crater. Known as the Zenith Movie (ZM) and Supra-Horizon Movie (SHM), the are taken with the NCAM and consist of eight frames captured directly above the rover (ZM) or just above the horizon (SHM) (Moores et al., 2015b). Over the years, similar movies with varying pointings have been added to the atmospheric movie umbrella. This includes the Phase Function Sky Survey (PFSS) that can estimate the shape of observed aerosols by investigating scattering through nine different pointings

around the rover (Cooper et al., 2019). The Cloud Altitude Observation (CAO) was also added that pairs a ZM and a east-pointing SHM to capture aerosol and shadow movement to directly calculate altitudes of aerosols (Campbell et al., 2020). For dust, the line-of-sight measurements by MSL (Moore et al., 2016, Moores et al., 2015a, Smith et al., 2020) is used to help determine if Gale Crater was a source or sink of dust. Since landing in 2012, MSL has been able to provide a large record of captured aerosols to calculate a variety of parameters that are still being recorded today.

More recent missions, such as the InSight lander and Perseverance rover, have upgraded MER legacy in order to to make advances such as RGB capability (Maki et al., 2018) and wider field of views (Maki et al., 2020, Rodriguez-Manfredi et al., 2021). These increased capabilities could expand our understanding of Martian aerosols from the surface as until InSight, the MER legacy cameras were mono channel (black-and-white). Adding colour to the analysis could help describe the type of aerosol observed, furthering Martian aerosol analysis from the surface.

1.3 Limitations of Current Surface Studies

Even with multiple missions studying the atmosphere, spacecraft are limited in how much science can be returned. Orbiters are useful for characterizing the atmosphere as a whole, but limitations described in Section 1.2 indicate that surface missions are extremely important for understanding the lower part of the Martian atmosphere. However, the high cost associated with creating, flying and operating a spacecraft limits how often they can be sent to Mars and therefore the number of different locations that can be investigated at any one time. Operational costs and spacecraft robustness also have to be considered to ensure that any mission is successful for a long enough period to acquire data for yearly and seasonal comparisons, preferably including both dust storm and non-dust storm years.

To fill in any gaps in Martian atmospheric studies, Global Climate Models (GCMs) are used. Several models exist (Neary and Daerden, 2018, Rafkin et al., 2001, Richardson et al., 2007, Spiga and Forget, 2009) and have been used to understand conditions for future and current landing sites. However, these still require physical Martian data to verify their accuracy and validate their performance. This creates a

feedback loop which can be solved by sending more missions to the surface. Haberle and Catling (1996) suggested that a minimum of 15 widely-displaced meteorological stations are needed to verify a GCM. Yet, there has only been less than 20 missions sent to the surface, with only two currently operational at the time of this dissertation. To properly verify a GCM and better understand surface-atmosphere interactions, more surface vehicles are needed on Mars. Low-cost, distributed options must be explored and can be developed by understanding how to fix limitations that current surface spacecraft currently have.

Camera capabilities have expanded throughout the years, though the basic operating principles remain the same. The MER (Maki et al., 2003), MSL (Maki et al., 2012), Phoenix (Lemmon et al., 2008) and InSight (Maki et al., 2018) cameras share a common CCD wafer. In the case of InSight, this wafer has been augmented by a bayer-patterned filter to return colour data from Mars (Maki et al., 2018). A variety of optics have also been used to obtain the most science from these cameras. The Phoenix SSI added a filter wheel (Lemmon et al., 2008), while Perseverance has a fisheye lens, boosting the FOV of the camera, giving it more atmosphere to observe in a single image (Maki et al., 2020, Rodriguez-Manfredi et al., 2021). This is extremely useful for maximizing the amount of sky being observed and minimizing operational constraints for obtaining an image. Most Martian missions are rarely focused on environmental studies, with the main objective geological based. Therefore, it is important to maximize camera capabilities for environmental studies since they are always included on spacecraft missions and thus could help expand Martian aerosol studies.

Other limitations such as operational constraints and data volume also have to be considered when investigating low-cost options. An example of this is atmospheric observation taken by MSL being restricted to 1-2 times per week because of priority and data volume. If observations were lower in data volume, more room on MSL's computer could be used to capture more observations. MSL's main priority is geological based studies (Grotzinger et al., 2012, Vasavada et al., 2012) so atmospheric observations are typically given lower priority. If a dedicated meteorological station is low-cost but can perform the same observations as MSL or other Mars missions, then it could significantly add more atmospheric data points from the surface of Mars. As shown back in Figure 1.6, the majority of Mars is still untouched from surface missions. With surface

vehicles also limited to only studying local conditions, more spacecraft need to be placed across the surface. Low-cost options could be the solution to laying down this groundwork for more local meteorological stations which would not only benefit accuracy with GCMs but further our knowledge of the Martian atmosphere as a whole.

1.4 Dissertation Roadmap

The goal of this dissertation is to examine Martian aerosol movement through surface spacecraft imagery while also learning what needs to be done to maximize more observations from Mars. This includes using imagery from the Mars Science Laboratory (MSL) and InSight missions to understand how Martian aerosols behave. Expanding this will be learning low-cost options such as data volume reduction from automated processes and pairing a panoramic camera and laser system to mimic Mars missions.

Chapter 2 will discuss imagery from MSL and InSight lander to determine wind direction based on aerosol movement. The large collection of atmospheric movies taken by MSL creates a record of observed aerosols over 5 MYs. Examining how aerosols behave over the course of a MY will help pinpoint if these said aerosols are affected by local circulation from Aeolis Mons or large-scale circulation from seasonal Hadley cells. For a comparison, images from the InSight lander will also be used because of its proximity to MSL. No Martian surface missions were close enough together during operations for a direct comparison till MSL and InSight and thus wind parameters will be compared to determine if they share similar circulation behaviours.

Chapter 3 investigates an automated analysis of wind parameters (direction and speed) to determine if computer techniques such as Machine Learning and Computer Vision can directly calculate aerosol movement in movies without first downlinking the movie. This would significantly decrease the amount of data volume needed to return such information, thus allowing more data to be collected. The limitation of Martian surface data could be aided by such a technique on future missions to enable a better understanding of the behaviour of aerosols in imagery.

Chapter 4 takes into account results from previous Martian surface missions and investigates a low-cost optical meteorological station. The Phoenix and MSL missions have shown that simple imagery of aerosols

can return an abundant of information such as wind movement and opacity. The Phoenix mission was equipped with a lidar to calculate water-ice cloud altitudes. Moores et al. (2011) was able to discern water-ice content by imaging the lidar in use so it could be of use to learn if a lower powered laser could also return similar information. Using the knowledge from both Phoenix and MSL, the Mars Panoramic camera and Laser Experiment (MAPLE) was constructed and taken to Argentia, Newfoundland to test with near-surface fog.

2 Martian Aerosol Analysis with Surface Missions

2.1 Overview

Two surface missions - The Mars Science Laboratory (MSL, Curiosity) rover and the InSight lander - have taken many images of the atmosphere through engineering activities such as workspace monitoring (InSight) or drive-direction images (MSL) that are intended to document engineering activities. Both missions have therefore observed aerosols. When multiple images are taken close together that capture the same area of the sky, a movie can be created to tell us how observed aerosols move in the Martian atmosphere. The images and movies acquired from both missions can be analyzed individually to understand local conditions.

However, even more can be learned about the Martian atmospheric circulation and the effect of local conditions and topography by comparing results from these two missions. MSL and InSight are especially well suited to this kind of study as they are in close geographic proximity (600 km (noa, 2019)) and were operational at the same time. MSL is in a crater which subjects the rover to crater-drived wind circulation patterns whereas InSight is located on the nearby plains, though subject to the same regional atmospheric flows. Both missions will be considered serparately and then the results obtained will be combined and compared to determine what differences, if any, can be seen between the crater and plains.

2.1.1 The Mars Science Laboratory (MSL, Curiosity) Mission

The MSL rover, Curiosity, is located in Gale Crater (5.4°S, 137.8°E). Gale crater is a typical Martian crater containing a large central mound that rises over 5 km above the encircling moat. Known as Aeolis Mon (Mt. Sharp), this central mound is broader than typical complex craters seen on other planetary bodies due to

the presence of layered sediments that were deposited three billion years ago when a lake filled the crater (Grotzinger et al., 2012, Vasavada, 2022). The crater itself is located directly on the Martian dichotomy boundary (Grotzinger et al., 2012) which separates the older, heavily cratered southern highlands from the younger, smoother northern plains. This leads to a sloped crater topography exhibited by a northern rim that is substantially lower than the southern rim as shown in Figure 2.1.

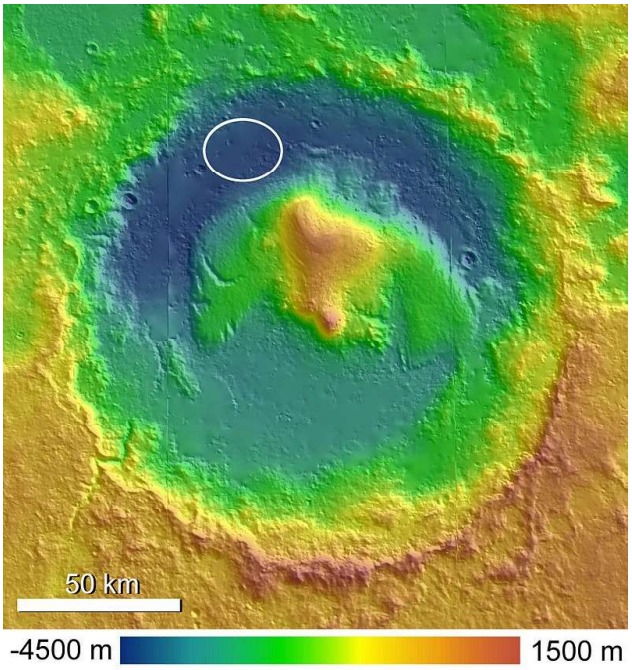

Figure 2.1: Figure 2a from Anderson (2010) showcasing the topography of Gale crater. The landing ellipse for MSL is shown in the NW corner of the crater, with north at the top of the map. The difference in elevation between the north and south side of the crater could attributed to being right on Mars' dichotomy boundary.

This crater topography affects water vapour by forcing air passing over Aeolis Mons to rise and cool, causing orographic clouds to condense. This is especially true with air travelling from the water-vapour rich north during the Aphelion Cloud Belt (ACB) season. Evidence of this behaviour has been exhibited by the presence of gravity wave clouds observed through movies taken at Gale crater (Kloos et al., 2018, Moores et al., 2015b). An example of this is shown in Figure 2.2 Nonetheless, such clouds are not especially common

in the MSL atmospheric movie dataset.

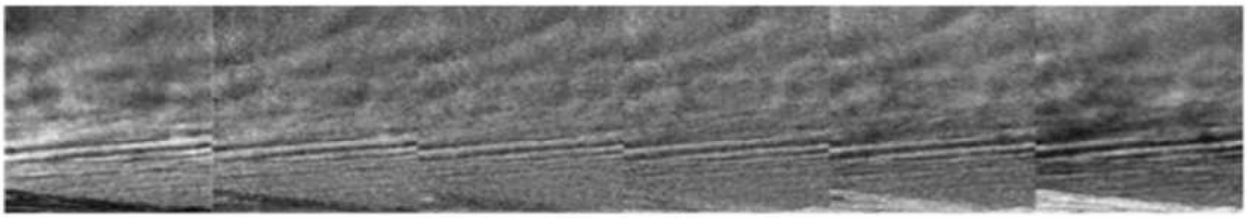

(d) Sol 1302 south-facing SHM

Figure 2.2: Figure 3d in Kloos et al. (2018) shows gravity waves observed by MSL on sol 1302.

Naturally, such flows happen frequently even when there is no condensing water vapour to reveal them in movies. For instance, Haberle et al. (2014) suggest that low altitude (100 m) gravity waves could exist in Gale crater as observed by the Rover Environmental Monitoring Suite (REMS). REMS measured an evening oscillation that occurred between 19:30 and 22:30 LTST with a mean wavelength of 5-6 km (Haberle et al., 2014). These are caused by down-slope flow from Aeolis Mons that leads to the formation of an especially stable layer near the crater floor. Considering a 5 km spacing between waves, Moores et al. (2015b) determined that observed sunset clouds with gravity waves would be > 20 km in altitude. The large discrepancy between these altitudes suggest that Aeolis Mons may only have little interaction on gravity waves within aloft aerosols as observed by (Moores et al., 2015b).

Global Climate Model (GCM) results for Gale crater (Moores et al., 2015a, Rafkin et al., 2016, Tyler and Barnes, 2013, Vasavada et al., 2012) show dry conditions near the surface with a suppressed Planetary Boundary Layer (PBL) of only a few kilometers depth, depending on the time of the year, as compared to nearly 10 km of PBL depth on the plains outside the crater. Haberle (2012) used the NASA-Ames GCM to show a complex diurnal cycle of surface winds caused by smaller-scale slope flows. Any larger-scale slope flows across the dichotomy boundary do not appear to affect winds inside the crater. This is supported by modelled results from (Moores et al., 2015a) that moist air from outside the crater is unable to enter due to the crater circulation. Moore et al. (2016) showed that Gale crater was more likely a dust sink rather than a dust source as line-of-sight measurements indicated little mixing within the crater in comparison to above

the crater. Smith et al. (2020) did show an increase in atmospheric mixing through further MSL imagery, yet this could be caused by the increasing altitude as MSL climbs Aeolis Mons. The minimal mixing found in imagery from MSL (Moore et al., 2016, Moores et al., 2015a, Smith et al., 2020) indicate dry conditions within the crater and thus any observed aloft aerosols in MSL atmospheric movies are most likely forming at altitudes well above the crater rim (Moores et al., 2015a). This agrees with Campbell et al. (2020) who found that the altitudes of water-ice clouds above Gale crater ranged between 15 and 40 km, well above Aeolis Mons and the PBL.

To further confirm this, wind analysis from REMS have shown that Aeolis Mons have a heavy influence on slope winds, with most winds recirculating back into the crater (Gómez-Elvira et al., 2014, Viúdez-Moreiras et al., 2019). However, damage to the wind sensor during landing meant that the instrument could only detect winds that flowed towards the front of the rover (Gómez-Elvira et al., 2014). This, in turn, creates a further dependency on GCMs which are required to simulate conditions within the crater, filling in the missing data on the ground. For instance, results using MRAMS (Pla-Garcia et al., 2016) and MarsWRF (Newman et al., 2017) were in agreement with REMS results that Aeolis Mons has an impact on winds. Other topographical features, such as the Bagnold Dunes (Newman et al., 2017) also affected surface-level winds. But how are upper level winds affected by topography and surface roughness? To investigate winds well above the rover in further detail, Zenith Movies (ZMs) taken by MSL can be analyzed and the direction of the winds aloft can be determined. This wind direction can then be compared to the surface wind results from REMS to further confirm how circulation both in and outside of Gale crater.

2.1.2 The InSight Lander

The InSight lander landed in Elysium Planitia (4.5°N, 135.6°E) in November 2018 and continued until end-of-mission in December 2022. As a lander, it does not move, and its main science objective was to investigate the interior of Mars by using seismology and heat flux measurements in the near-surface (Golombek et al., 2020). Being located on the plains, InSight is expected to experience more convective instability and PBL mixing through dust-devil lifting dust into the atmosphere. Seismometry is particularly sensitive to winds.

Notably, the signal in the Viking seismometers was strongly affected by winds and dust-devils (Lorenz et al., 2017). Therefore, InSight was equipped with the Temperature and Winds for InSight (TWINS) instrument which is used to decorrelate atmospheric effects from seismic signals (Banfield et al., 2018). It is composed of two sensor booms orientated horizontally and positioned diametrically opposite to each other on the lander deck such that both sensors are parallel. Both sensors are approximately 1.4 meters above ground level (Banfield et al., 2018). They are heritage equipment from the MSL REMS booms that use four hot film dice and a fifth cold die to calculate wind speed and direction (Gómez-Elvira et al., 2014). InSight was also outfitted with two cameras to view nearby terrain and to check on instrument status. Since InSight landed on the plains, these cameras could provide an opportunity to observe how aerosols behave with no major topographic features nearby. Figure 2.4 shows where the cameras and TWINS are located on the lander.

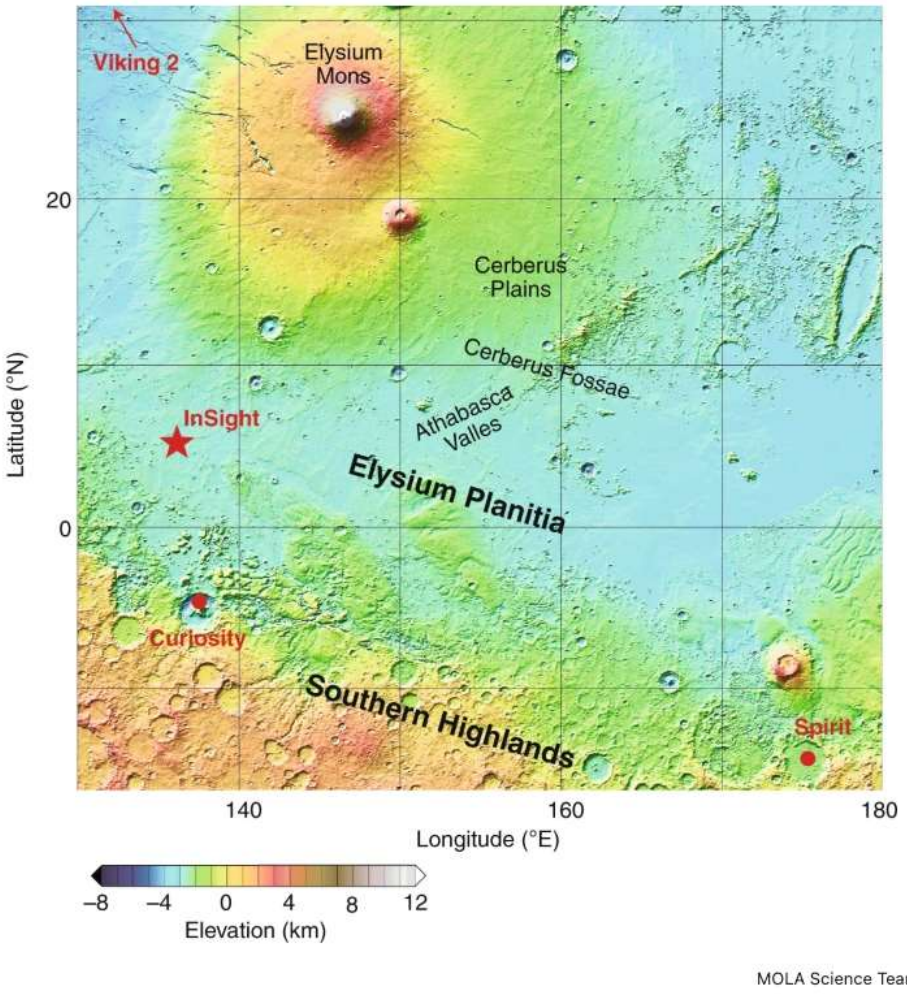

Figure 2.3: Figure 1 from Banerdt et al. (2020) showing InSight's location (star) versus other previous/current missions such as Spirit and MSL (Curiosity). InSight is located on the plains, just north of MSL.

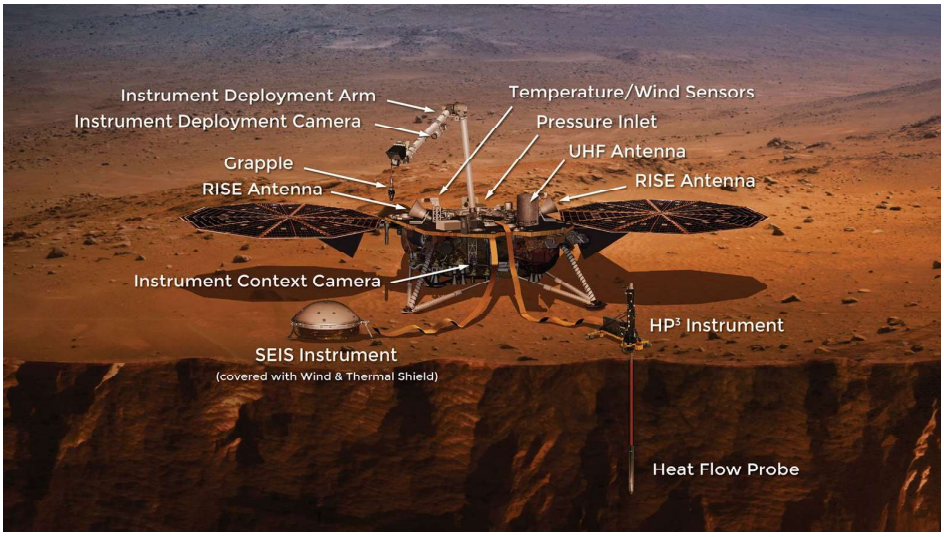

Figure 2.4: The InSight lander with its instruments. TWINS is labelled as Temperature/Wind Sensors and the two cameras are the Instrument Context Camera under the deck and the Instrument Deployment Camera on its arm. Credit: NASA/JPL-Caltech

Using the Laboratoire de Météorologie Dynamique (LMD) GCM (Forget et al., 1999), modelled near-surface wind results for Elysium Planitia showed variable sol-to-sol cycles, but regular seasonal cycles (Spiga et al., 2018). Wind directions did not behave similar to Pathfinder that observed winds move in a rotational manner (Schofield et al., 1997), which is deduced to InSight's location being featureless (Spiga et al., 2018). This means that local winds are primarily govern by large scale circulation rather than topography-induced circulations as seen in Section 2.1.1. If so, then near-surface winds may be more similar to aloft winds at InSight's location.

Utilizing a stationary camera on InSight that always views the same southern sky, movies can be analyzed for aloft aerosol movement. This can help characterize how aerosols in the middle atmosphere are moving with respect to large scale circulation from seasonal Hadley cells. Aphelion season winds typically have stable winds dependent on the northward branch of the Hadley circulation governing Easterly winds. Alternatively, during the Perihelion seasonal winds are stronger and change to Westerly. If InSight is mainly influenced by these Hadley branches, it would be of interest to investigate how aloft aerosols are behaving with respect to

the seasonal Hadley branches. Aerosols have already been observed using InSight's camera (Figure 2.5) and therefore can be explored further for aerosol movement over the course of a MY.

Figure 2.5: An example of water-ice clouds observed by the InSight lander. Taken by the Instrument Context Camera (ICC), aerosol movement can be seen in the top right of the image. Credit: NASA/JPL-Caltech

2.1.3 Author Contribution

For this Chapter of the dissertation, the goal was to investigate wind parameters from two nearby Martian missions to investigate atmospheric circulation. I was a Scientific Collaborator on the Mars Science Laboratory (MSL) and InSight missions to study atmospheric aerosols, specifically water-ice clouds, using imagery. This role included the ability to plan atmospheric movies to capture movement and reveal aloft wind directions. Wind data from Mars, especially aloft, is rare and current methods must rely heavily on atmospheric models to determine circulation and the behaviour of winds. However, the use of imagery to determine winds through the movement of aerosols could aid in acquiring direct winds from Mars.

My role in this Chapter involved creating movies and analyzing wind parameters if they showcased any aerosol movement. The MSL mission has set of dedicated atmospheric movies that are taken on a regular cadence and specific pointings. I investigated one set of movies (Zenith movies) for wind parameters across multiple Mars Years. On the other hand, the InSight mission did not have a dedicated observation so movies were sparse and typically only in the cloudy season. Images from the InSight mission were first processed by

Mark Lemmon, where he made noted sets of images (taken less than 15 minutes apart) that could be turned into a movie. These sets were sent to me to create the movie from already processed images and if aerosols were present, analyze further for wind direction. Graphs to show wind results were created by myself for both missions. Both missions were analyzed separately before being compared together.

In order to compare wind results from MSL further, a global climate model was used to simulate conditions in Gale crater. I seeked the help of Claire Newman who actively runs the Mars Weather Research and Forecasting (MarsWRF) model for different landing sites, including MSL. She agreed to run models simulating winds from the surface up to 40 km throughout a Mars Year. Results comparing the modelled results to the direct observation were done by me and was discussed with Claire to get input on the behaviour of wind in the atmosphere due to her expertise with wind measurements from the Rover Environmental Monitoring Station (REMS) onboard MSL. All graphs except the MarsWRF ones were produce by myself.

2.2 Methods

2.2.1 The MSL Mission

MSL has a dedicated cadence of atmospheric movies that capture aerosol activity through its Navigation Cameras (NCAMs). Typically the NCAM is used for engineering purposes such as terrain context or geological targeting (Maki et al., 2012). However, the NCAMs have also been radiometrically calibrated which allows them to be used for scientific purposes. There are two pairs of NCAMs which are used depending on which onboard flight computer MSL is using (described by the mission as either 'A' or 'B') since the NCAMs are hard-wired to only a single processing unit. Having two computers onboard ensures that there is always a spare brain to which the spacecraft can switch in case of any fault (Maki et al., 2012). Therefore, atmospheric movies and other products produced from NCAM images from MSL are labelled with either its A or B computer and either the Left or Right camera. The NCAM location on MSL is on the mast and is able to view a variety of locations due to the moveable mast (Figure 2.6).

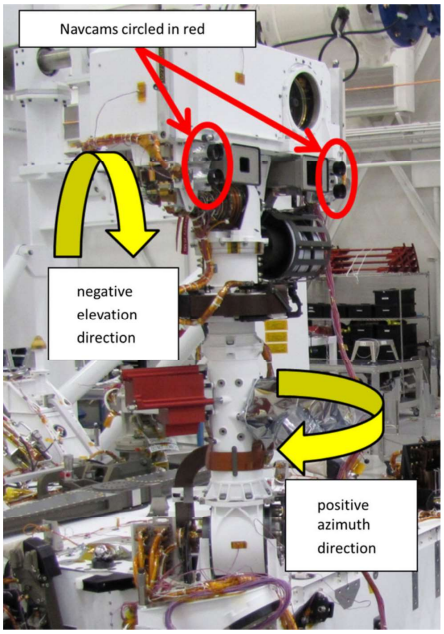

Figure 2.6: Figure 3 from Maki et al. (2012) shows the location of the NCAMs on the Remote Sensing Mast (RSM).

The NCAMs are build-to-print copies of the Mars Exploration Rover (MER) engineering cameras that use a broadband visible filter in the wavelength range of 600-800 nm as shown in Figure 2.7 (Maki et al., 2012). They are located on the Rover Sensing Mast (RSM) which sits 1.9 meters above the surface (Maki et al., 2012). The RSM is capable of 360° of azimuthal motion and 178° of elevation motion, allowing for any part of the ski to be observed by the imager. The NCAM boasts a comparatively large field of view of 45°×45° and has a relatively high signal-to-noise ratio of 200:1 for well exposed images (Maki et al., 2012) as compared to the Mast Cameras (MCAMs). These useful parameters of the NCAMs makes these imagers ideal for observing atmospheric aerosols that can translate over large angles during the time required to capture their motion (Kloos et al., 2016, Moores et al., 2015b).

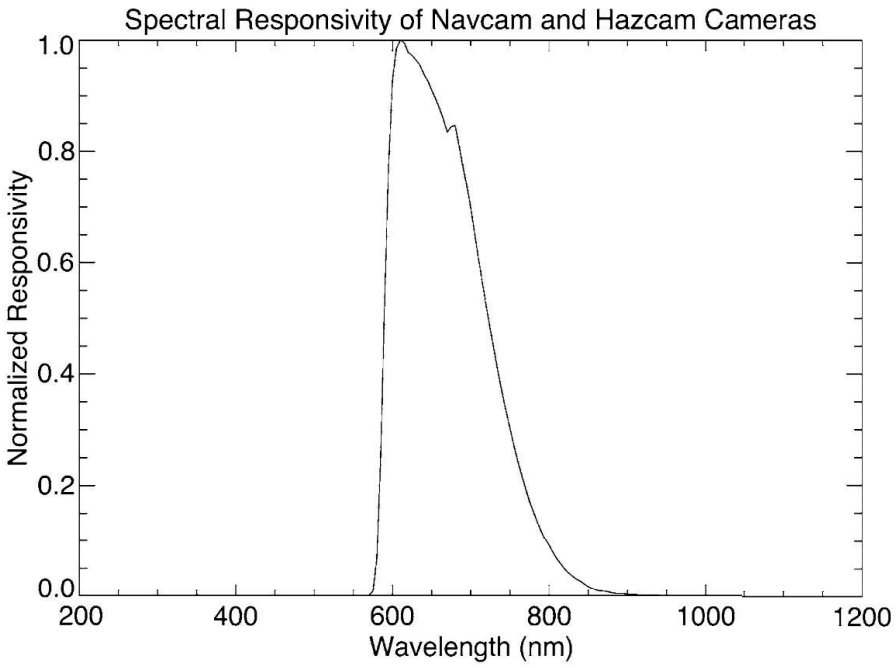

Figure 2.7: Figure 2 from Maki et al. (2012) where the spectral range of the NCAM is 600-800 nm. The NCAMs are black-and-white so only one wavelength is shown.

For this work, we used a specific product known as a Zenith Movie (ZM) to investigate aerosol movement. A ZM consists of eight vertically pointed frames taken by the NCAM. It has been previously used for calculating wind speed (Campbell et al., 2020), optical depth (Kloos et al., 2016; 2018) and as part of a larger observation that was able to constrain cloud altitudes (Campbell et al., 2020). A total of 650 ZMs have been acquired since the start of the mission.

Over the course of the mission, the specific camera parameters employed to capture ZMs have changed slightly based on a changes in operational restrictions. The duration of a movie has fluctuated between 88 seconds and 287 seconds which had to be noted for each movie to ensure movement was represented per second. The size of the movie has also changed. ZMs from the beginning of the mission till MY 35 were downsampled to 512x512 pixel images, but were upgraded to non-downsampled 1024x1024 images. This change was made as more data volume became available in spacecraft downlink activities. Rather than send

'fill bits' back to Earth, the science and operations team chose instead to reduce the compression and remove the downsampling on atmospheric images.

To fully analyse the ZMs, Mean-Frame Subtraction (MFS) is used on raw frames. The thin nature of aerosols at Gale crater often means that these features are sub-optical (optical depth of less than 0.04 (Kloos et al., 2016; 2018)) which makes them difficult for an operator to observe in raw frames. The MFS technique computes an average frame from all eight frames of each movie and then subtracts this mean-frame from each individual image to isolate any time-variable component (Kloos et al., 2016; 2018, Moores et al., 2015b). This time-varying component would typically be any moving dust or water-ice in the atmosphere. An example of the difference between raw and MFS frames are shown in Figure 2.8. All movies shown in this chapter will have MFS applied to allow the reader as much contrast as possible on the features described.

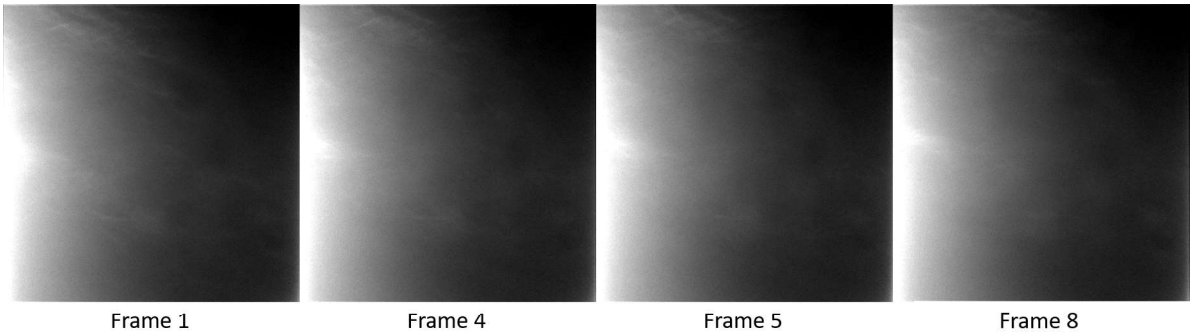

(a) top: raw frames of a ZM before MFS processing.

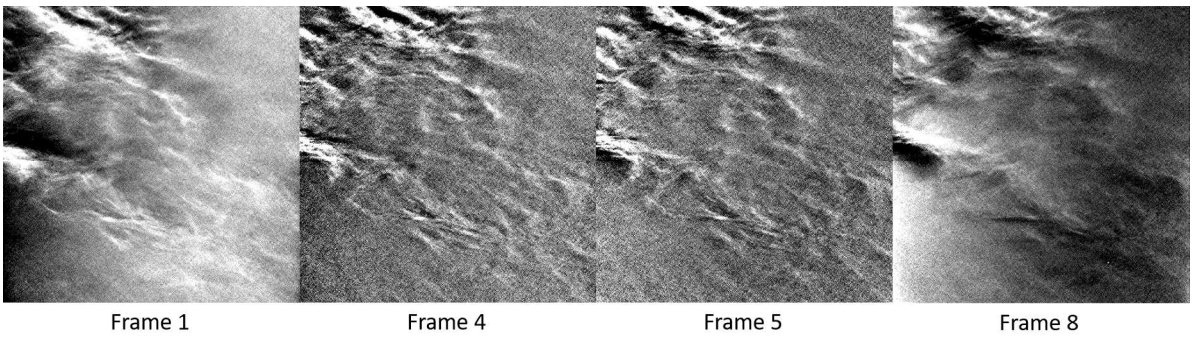

(b) bottom: processed frames of a ZM after MFS.

Figure 2.8: An example of a Zenith Movie (ZM) taken on sol 1748 at 06:46 LTST. This is an example of a movie with strong, consistent water-ice cloud features. MFS processing helps bring out more features to analyze within the movie.

In order to determine the wind direction in a movie, we took the orientation of the frame into consideration. To minimize saturation in images throughout a MY, the movies switch between north (0°) and south (180°) azimuthal pointing to maintain as much angular distance between the centre of the captured frame and the solar disc. This affects the cardinal direction location in the frame: images orientated North will have north as the bottom of the frame, south as the top with east to the right and west to the left. Similarly, images orientated towards the South will have South at the bottom of the image, North at the top of the image, West to the right and East to the left. This orientation is shown in Figure 2.9. Once each frame has been orientated, we analyzed movies that showcased aerosol movement for wind direction and angular wind

speed.

Figure 2.9: Orientation of the cardinal directions (N = North, E = East, W = West, S = South) depending on the azimuthal direction of MSL. The orientation of the rover was noted per movie to ensure that the correct cardinal direction was represented in calculated wind directions.

Angular wind speed was found by taking into account the NCAM's field of view (FOV) of 45° which determines the angular size of each pixel. By following how far aerosol features move across the frame in pixels, a translation to degree/pixel returns an angular distance. This, in turn, becomes angular speed once angular distance is divided by the duration of the movie. This angular wind speed will tell us if there is a particular part of a MY that has faster moving aerosols or lower altitude aerosols compared to others. Because this method returns an angular speed, it is not capable of distinguishing between slow low altitude motion and rapid high-altitude motion.

2.2.2 The InSight Lander

Unlike MSL, the InSight lander mission did not have a dedicated observation or cadence to observe Martian aerosols. InSight was equipped with two cameras, the Instrument Deployment Camera (IDC) and the Instrument Context Camera (ICC), which are both flight spare engineering cameras from MSL. The IDC is analogous to the Navigation Camera and the ICC is analogous to the Hazard Avoidance Camera (Maki et al., 2012; 2018). However, the main difference between the InSight cameras and the MSL cameras is

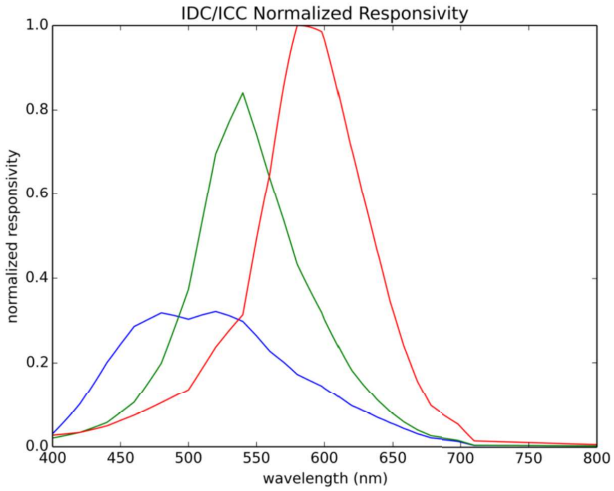

Figure 2.10: Figure 6 from Maki et al. (2018) describing the colour wavelength responsivity of the InSight cameras. The cameras work best with red light, which is best suited for Martian geological studies. Unfortunately, the best wavelength for this work would be blue, which is less responsive due to the decrease in quantum efficiency of the CCD in that colour (Maki et al., 2018).

that the InSight cameras were upgraded by adding bayer-pattern filters which allow a colour image to be reconstructed from IDC and ICC data. This change was made in order to distinguish between different types of Martian geological targets in InSight lander images (Maki et al., 2018). Figure 2.10 showcases the wavelength responsivity of the camera for each colour. The low response to blue is due to the decreased in quantum efficiency of the CCD at these wavelengths (Maki et al., 2018), which poses a problem for our work as both red and blue are needed to understand aerosols. Red is preferred for dust aerosols and blue is preferred for water-ice aerosols. In order to maintain as much signal-to-noise as possible and consistency between colour, we chose to convert the images entirely into black-and-white before analysis to make use of all colours in the bayer-pattern filter (Lemmon et al., personal communication).

For this work, we only used the ICC due to its fixed position facing the southern horizon. The IDC could be useful for observing aerosols at different pointings but the main objective of this camera was for instrument deployment, monitoring and geological targeting. Retasking this camera to atmospheric observation introduced additional complexity in mission plans and therefore fewer images of the atmosphere

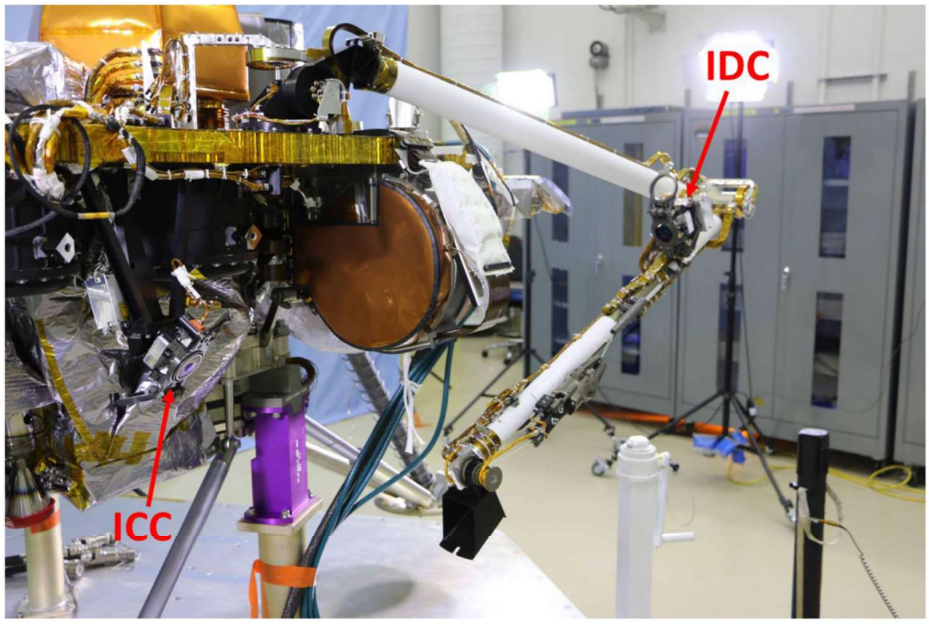

Figure 2.11: Figure 1 of Maki et al. (2018) shows the location of the ICC and IDC on InSight. The IDC is located on InSight's arm allowing it to move. The ICC is mounted on its underside and has a fixed position.

were acquired with this camera. By contrast, the fixed positioning of the ICC means that the sky is captured in every image. The location of the ICC (Figure 2.11) is mounted just under the lander and does include both ground and atmosphere in every frame. Since we are only investigating aerosol movement in the atmosphere, every ICC image was cropped to only include the sky.

All images taken by the ICC were processed and provided by Mark Lemmon from the Space Science Institute. These images were processed using a non-adaptive $\pm 10\%$ stretch. In some cases, ICC images were taken less than 900 seconds (15 minutes) apart in time and used to create a short movie. These horizon movie candidates were noted and investigated further for aerosol movement. An example of a movie is shown in Figure 2.12.

If a movie was found to have aerosol movement, we would find the meteorological wind direction to the nearest intercardinal direction (e.g. NE, N, NW). With a field-of-view of 124° x 124° and azimuthal pointing of 180°, it views ESE to WSW and thus can give us a general direction of where aerosols are moving from. Since no overhead images are included with the ICC, angular wind speed is not easily achievable and was

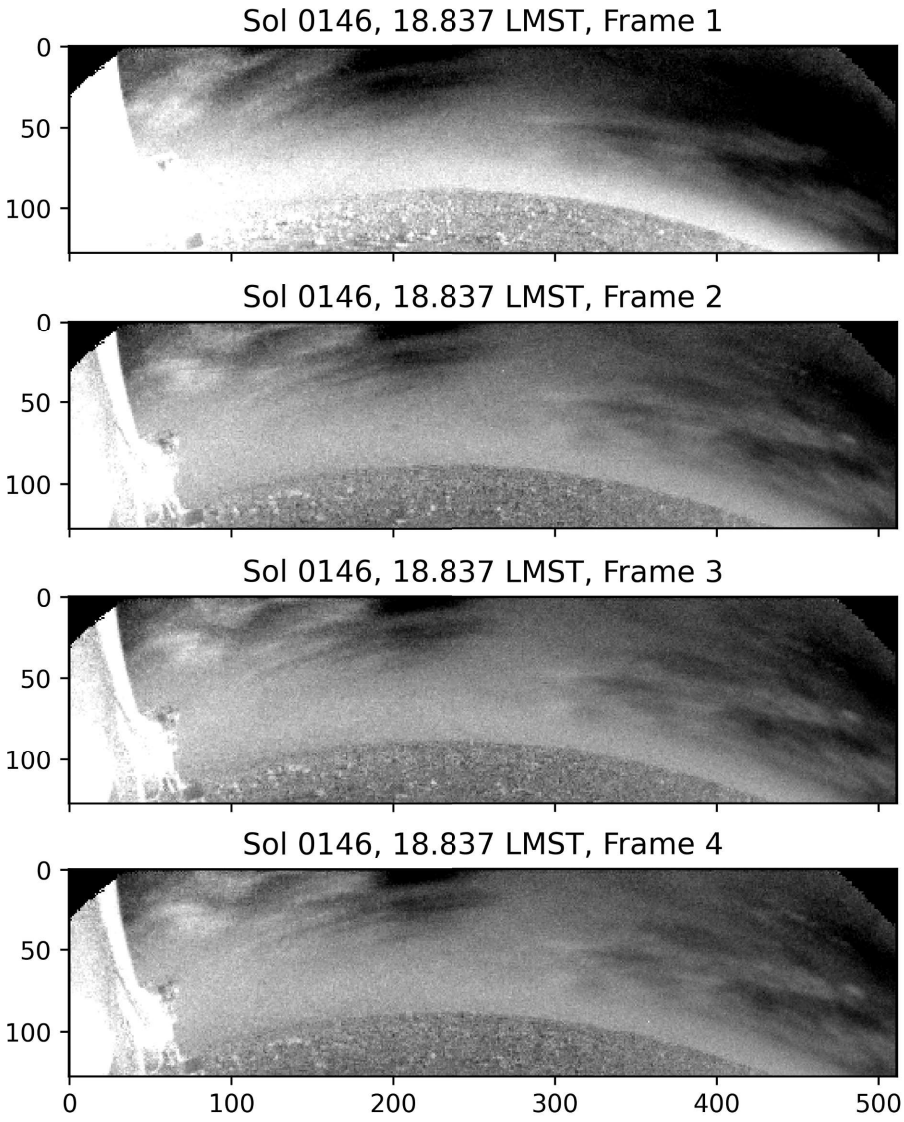

Figure 2.12: Frames 1-4 of a twilight movie taken on sol 146. These frames have been cropped to only include the sky and processed using a non-adaptive ±10% stretch (Lemmon et al., personal communication). Aerosols can be seen moving from the left side of the frame to the right. The ICC has an azimuthal pointing of 180°, thus the perpendicular movement of the aerosols indicates an Easterly direction.

not explored in this analysis.

The southern azimuthal pointing of the ICC means that InSight captures images of the sky that are oriented towards Gale Crater and MSL, which is just south of InSight's landing location. By observing the movement of aerosols in that area, we can compare to results from MSL that was also operational at the same time.

2.3 Results and Discussion

2.3.1 The MSL Mission

For clarity, wind rose plots were used to showcase the wind results from MSL. We split up results into Aphelion (cloudy season) and Perihelion (dusty season) in Figures 2.13 and 2.14 respectively. Diurnal changes have been reported in MSL data previously (Campbell et al., 2020, Kloos et al., 2018) and thus we investigated both time periods separately. These are denoted as AM, consisting of all data acquired before 12:00 LTST, and PM, consisting of all data acquired after 12:00 LTST, both expressed in Local True Solar Time (LTST).

In the plotted wind roses, the compass rose is divided into sixteen different angular source wind direction ranges, each of which is 22.5° wide. The length of each triangular pie slice-shaped radiant is scaled to the fraction of the total wind data which can be found within that source wind direction range. For instance, if the wind data were equally distributed between all source wind directions, each radiant would have a length of 6.25%. This radiant is further divided into wind speed bins which are shown with different colours. The fractional length (not fractional area) of each coloured segment of the radiant is equivalent to the fraction of all data from that source wind direction which falls into that wind speed bin. The wind speeds themselves are derived by assuming an altitude of 40 km for every cloud layer and represented by the colours shown in the bottom left of the figure. Finally, please note that these wind roses display the wind source direction and not the wind destination. As such, measured wind from the east travelling to the west would be plotted on the east or right side of the chart.

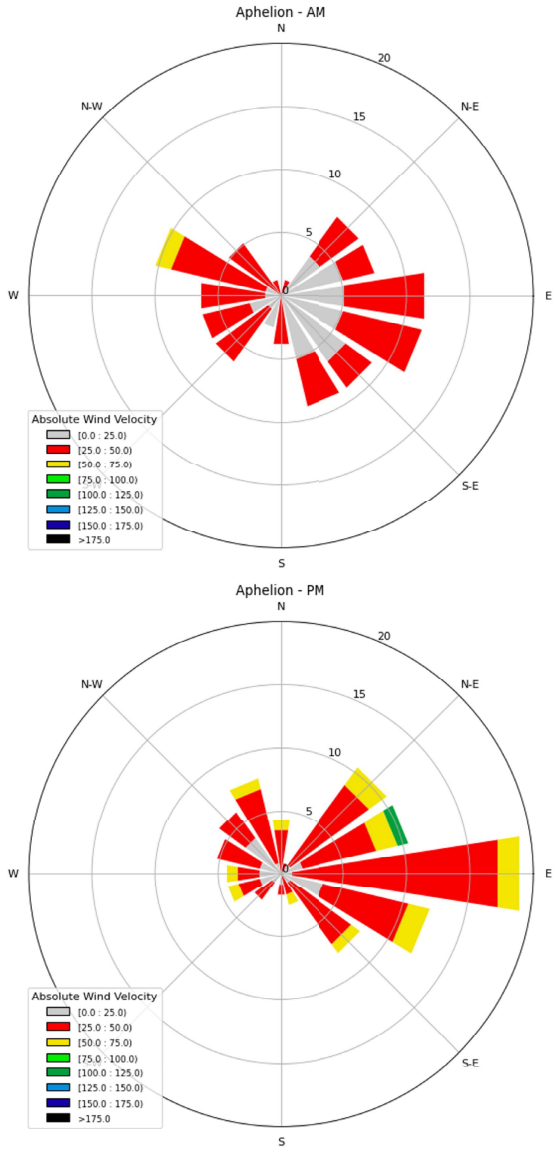

Figure 2.13: Results for the Aphelion season (L_s 0°-180°) split between AM (< 12:00 LTST) and PM (> 12:00 LTST). Easterly and Westerly winds were common in the morning (top) and predominate over north and south winds, but strong Easterly predominate over all other wind directions in our data in the afternoon (bottom). Wind velocities are shown by the colourbar which is based on 40 km altitude.

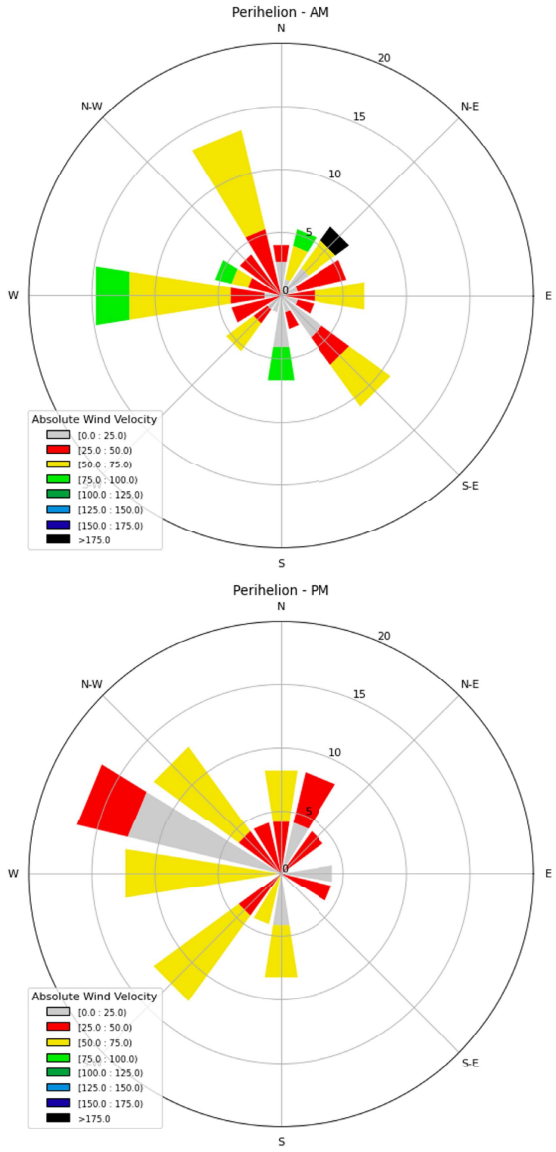

Figure 2.14: Results for the Perihelion season (L_s 180°-359°) split between AM (¡ 12:00 LTST) and PM (¿ 12:00 LTST). Winds were highly variable in both speed and direction in the morning (top), with somewhat more consistent wind speeds and direction, predominantly from the West in the afternoon (bottom). This change between Aphelion winds (from the East) could be due to changing Hadley cells between the seasons. Wind speeds are shown by the colourbar which is based on an assumed altitude of 40 km for every cloud deck.

Diurnal results show variable (though predominantly east-west versus north-south) results in the morning while a strong East (Aphelion) and West (Perihelion) wind direction in the afternoon. Wind directions were more variable during the dust season which could be attributed to the behaviour of dust in comparison to water-ice clouds. The change in direction between Aphelion and Perihelion could be due to the changing behaviour of the Hadley cell between Martian seasons. Due to a lack of oceans and the eccentric nature of Mars' orbit increasing the amplitude of insolation forcing, the Hadley circulation is much larger in latitudinal extent than on the Earth (Richardson and Wilson, 2002). Using the NASA Ames GCM, Haberle et al. (1993) demonstrated Hadley cell behaviour at equinoxes and solstices and discovered that Mars exhibits Earth-like Hadley cells at equinox ($L_s = 0°$, $180°$) but a non-Earth-like Hadley cell during solstice ($L_s = 90°$, $270°$). At solstice, a single cross-equatorial Hadley cell forms and ranges between 30°S and 30°N (Haberle et al., 1993). This single Hadley cell enables the transportation of aerosols between hemispheres which was confirmed from orbital data either measuring aerosol abundance over a MY (Smith, 2004) or through imagery of water-ice clouds (Tamppari et al., 2003). The Easterly winds associated with Hadley cell circulation at the tropics (Haberle, 2003) agrees with our results of strong Easterly directions observed in the afternoon during Aphelion (Figure 2.13). This points towards aerosols observed in ZMs most likely associated with large scale circulation at higher altitudes rather than being governed by near-surface sloped winds from Aeolis Mons. Even though Easterly winds are not as strong in Perihelion as expected with Hadley cells at solstice, this could be due to a variety of factors. Not as many data points are within the Perihelion season versus Aphelion and thus the Perihelion season may not be as well represented as Aphelion. Secondly, dust aerosols are more often captured by ZMs during Perihelion and exhibit different behaviour in comparison water-ice clouds such as higher speeds and more chaotic motion (Campbell et al., 2020). This is shown in Figure 2.14 where more yellow and green colours (faster speeds) are more common during Perihelion. Dust aerosol altitudes could in fact be closer to the surface than water-ice aerosols in Aphelion and thus more governed by Aeolis Mons, however, knowing the altitude information of aerosols within ZMs is impossible with just the NCAM. Thus it is hard to determine if dust aerosols are near-surface and fast or aloft and large scale. However, both Aphelion and Perihelion results can be compared to measured wind directions by the Rover

Environmental Monitoring Suite (REMS) onboard MSL to help further pinpoint where these aerosols behave at Gale crater.

The unfortunate damage to the REMS wind sensor (Gómez-Elvira et al., 2014) impeded constant wind measures, which lead to Newman et al. (2017) completing a set of high density REMS wind measurements during the Bagnold Dunes campaign to constrain patterns associated with aeolian processes. During MY 33 from L_s 64° - 104°, the Bagnold Dunes Campaign characterized the wind around three separate locations by optimizing two rover headings. The pointing of the rover is critical as REMS was unable to measure winds unless they came towards the rover (Gómez-Elvira et al., 2014). Thus, Newman et al. (2017) used the MarsWRF model to predict wind source directions and to try to make correlate which directions the rover should face to best capture expected winds. The sols from this paper were noted and compared to the ZM dataset to determine if any ZMs were acquired on the same sol as a REMS measurement. Table 2.1 showcases any ZMs that have a calculated wind direction on a same sol that Newman et al. (2017) had REMS measurements. Figures 8-10 from Newman et al. (2017) are quiver plots with arrows pointing where the winds are going towards, aka if an arrow points directly up winds are moving towards north. Wind directions from ZMs are changed to the same orientation as Newman et al. (2017) quiver plots to enable a quick comparison. Some sols in Table 2.1 do agree with measured wind directions (e.g. sol 1211), however, with only a minimal amount of data in both ZM and REMS data is only showing a small section of the true wind direction behaviour at Gale crater. With sol-to-sol variability noted in REMS wind results (Newman et al., 2017, Viúdez-Moreiras et al., 2019), it may be better to investigate how winds compare seasonally.

Table 2.1: Wind Direction comparison between ZM observations and REMS measured winds during the Bagnold Dune campaign from (Newman et al., 2017). Figure numbers in the REMS Wind Direction column are referencing figures from Newman et al. (2017).

Sol	ZM Time [LTST]	ZM Wind Direction [°, TO]	REMS Wind Direction [°, TO]
1163	14:48	236.6, SW	SSE (Figure 8)
1176	08:10	249.0, WSW	NNE (Figure 8)
1176	16:16	230.6, SW	SE (Figure 8)
1193	15:43	279.5, W	NaN (Figure 9)
1211	08:21	100.5, ESE	ESE (Figure 9)
1216	07:29	46.0, NE	NaN (Figure 10 in (Newman et al., 2017))
1234	15:11	312.4, NW	SSE (Figure 10 in (Newman et al., 2017))
1235	07:22	261.1, W	NaN (Figure 10 in (Newman et al., 2017))
1241	15:27	324.5, NW	SSE (Figure 10 in (Newman et al., 2017))

An expanded analysis from Viúdez-Moreiras et al. (2019) showed Northerly winds during both the day before switching to Southerly overnight before turning back to Northerly by morning, all highly dependent on nearby Aeolis Mons. However, sol-to-sol variability made it difficult to characterize them without having to average over multiple sols and thus it was better to classify them seasonally (Viúdez-Moreiras et al., 2019). Figure 2.15 highlights REMS results split into six timeslots. The best timeslots for a comparison to ZM results would be the first column (*DW (07:00-10:00), Figure 2.15*) and third column (*DL (15:00-18:00), Figure 2.15*) as those are the timeslots where ZMs occur. No midsol REMS results (*MD (10:00-15:00)*, Figure 2.15) are comparable to ZM results as the vertical pointing of the ZM observation is not sunsafe midsol (Campbell et al., 2020).

Figure 2.15: Table from Viúdez-Moreiras et al. (2019) showcasing REMS wind seasonal results in a variety of timeslots. The timeslot best comparable to ZM results is the first and third column.

Summary of the wind observations: wind directions and mean wind speeds for the different timeslots. Timeslots with a no-clear predominant wind direction are labeled as "variable". Empty boxes indicate periods with no high quality winds.

L_s period	Diurnal timeslot (LTST period) DW (07:00–10:00)	MD (10:00–15:00)	DL (15:00–18:00)	NF (18:00–21:00)	NL-1 (21:00–24:00)	NL-2 (00:00–03:00)
000°–060°	NNE, W[c] (5.7 m/s)	NNE[c] (8.1 m/s)	NNE, W[c] (5.9 m/s)	NE to SSW[c] (4.5 m/s)	variable, N to SW[c] (4.6 m/s)	–
060°–120°	W-WNW (5.3 m/s)	N-NW (6.2 m/s)	W to N (5.3 m/s)	NE to S (4.2 m/s)	–	–
120°–180°	variable, W-NW-N (5.5 m/s)	N-NNE (7.6 m/s)	variable (6.6 m/s)	N to SW (5.4 m/s)	SE to SW (5.1 m/s)	–
180°–240°	NNE-ENE, W (5.1 m/s)	N-NE (6.9 m/s)	N to E (6.7 m/s)	N to SW (5.4 m/s)	variable, W to E (5.7 m/s)	E-ESE (4.8 m/s)
240°–300°	NW to NE[b] (4.9 m/s)	NW to NE[b] (6.6 m/s)	ENE-ESE[a] (6.4 m/s)	NE[a] (5.6 m/s)	–	ENE-E[a] (5.3 m/s)
300°–000°	N[a,c] (5.2 m/s)	N, NE[a,c] (6.9 m/s)	N to NE[a,c] (6.5 m/s)	NE[b,c] (5.3 m/s)	–	–

[a] Representativeness of the measured dominant winds is not ensured.
[b] Assumption based on the rover headings for this timeslot. Wind speeds, if available, are computed using the retrieved dominant winds.
[c] Mean wind speed for another available MO (MO-1 or MO-3), instead of MO-2 (see Figs. 8–13 for details).

Aphelion (L_s0°-180°) morning results for ZM wind directions (Figure2.13) were variable between Easterly with some Westerly while REMS wind directions (Figure 2.15) for those same parameters noted Northerly and Westerly winds. Similar REMS wind directions were also in the afternoon, while ZM wind directions change predominantly Easterly during Aphelion afternoon (Figure 2.13), conflicting with REMS results in Figure 2.15. When investigating Perihelion morning wind directions, ZMs had highly variable direction, with no clear pattern (Figure 2.14) whilst REMS wind directions for that same time and L_s still exhibited strong Northerly directions (Figure 2.15). During Perihelion afternoon, ZMs observed strong Westerly winds (Figure 2.14) with REMS still observing Northerly and some Easterly winds (Figure 2.15). The similar Northerly wind direction measured by Viúdez-Moreiras et al. (2019) in both Aphelion and Perihelion was attributed to similar circulation types within the crater at all seasons (e.g. topographical circulation from Aeolis Mons) that has been modelled to overtake the large-scale circulation from the above Hadley cell (Rafkin et al., 2016, Tyler and Barnes, 2013). However, a similar direction within ZM results is not observed as a clear switch between Easterly (Aphelion) and Westerly (Perihelion) winds, further indicating that any aerosols observed in ZMs are most likely entrained in circulations above the level of the crater topography (e.g. Hadley cells circulation).

In order to better understand the measured ZM wind directions, it was necessary for us to compare to modelled results at Gale crater. To do this, wind speed and direction outputs were modelled at every

$30° L_s$ using the Mars Weather Research and Forecasting (MarsWRF) model, provided by Claire Newman. These models were ran with the same version as published in Newman et al. (2017) which matched well with REMS wind directions and speeds, making it ideal for a NCAM comparison. Since wind shear has been modelled to change wind directions and speed versus altitude (Rafkin et al., 2016), wind outputs from MarsWRF will be at 1.5 meters (REMS height) to resemble near-surface winds and then 20 km, 30 km, and 40 km which resembles the most likely altitudes of aloft aerosols (Campbell et al., 2020). The model ran by Claire Newman was done at 12 times of a MY during a nominal non-GDS (Global Dust Storm) year. To help compare to diurnal changes seen in ZMs, snapshots are provided by Claire at four different times of the sol (06:00, 09:00, 15:00, 18:00). Figure 2.16 showcases MarsWRF results over the course of the modelled MY with the x-axis representing L_s and y-axis as altitude. Arrows point in the direction the wind is travelling towards and the length of the arrow indicates speed. The longer the arrow, the faster the winds are travelling.

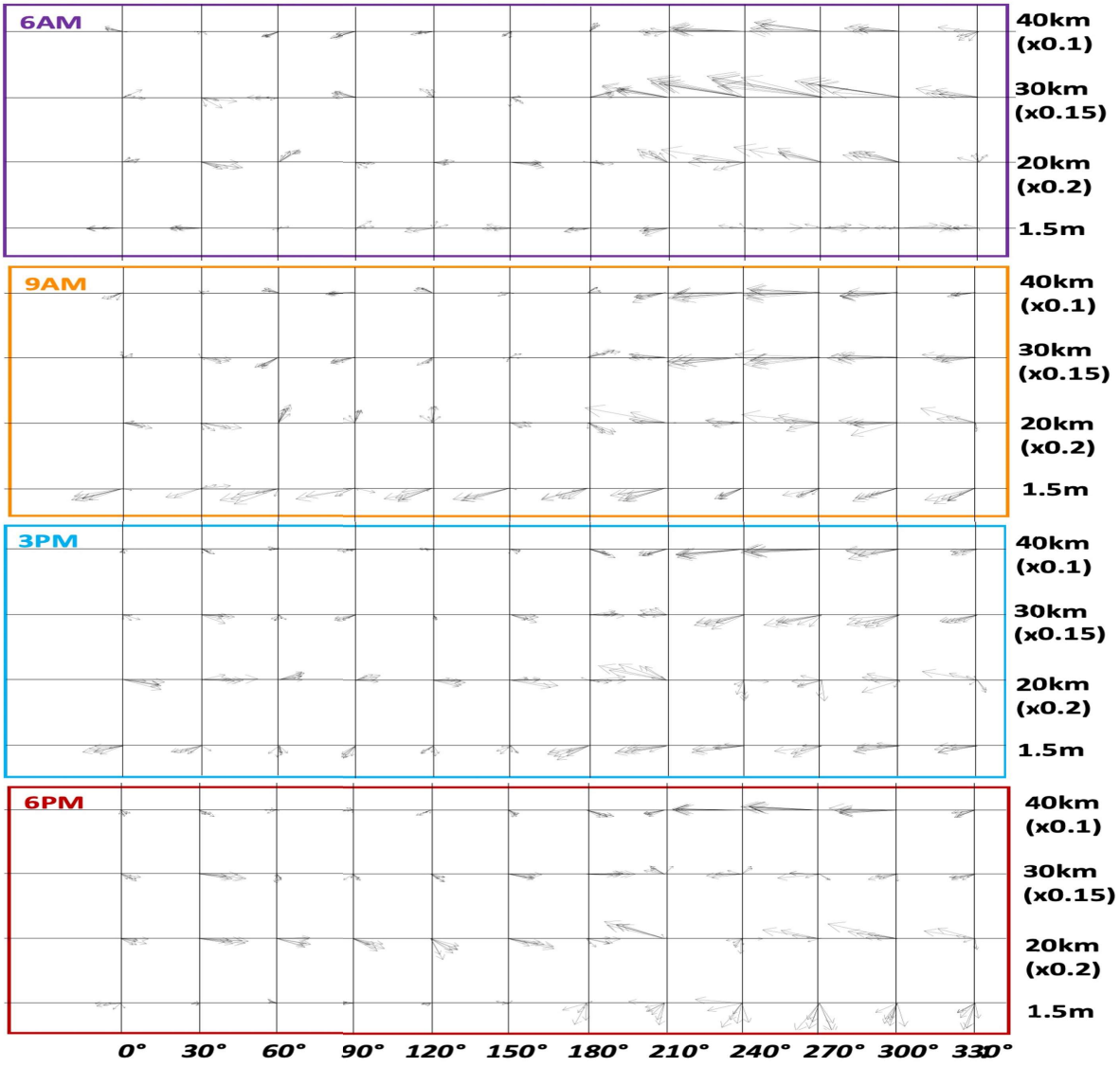

Figure 2.16: MarsWRF results for time bins 06:00, 09:00, 15:00, 18:00 LMST for varying altitudes as a function of solar longitude. The lowest altitude represents REMS (1.5 meters) and describe how winds would behave near the surface. The three upper altitude levels corresponds to altitudes where clouds are often observed in models and in previous work (Campbell et al., 2020).

To further compare to modelled wind directions and speeds we updated the ZM graphs to better represent the four time bins. This is shown in Figures 2.17-2.18 which have been split between AM (06:00 and 09:00 timebins) and PM (15:00 and 18:00 timebins). The MarsWRF results had arrows pointing where the winds

are going to (e.g. pointing up means winds going towards North) and we also updated the ZM wind directions to represent the same and are shown by arrows underneath each MarsWRF timeslots.

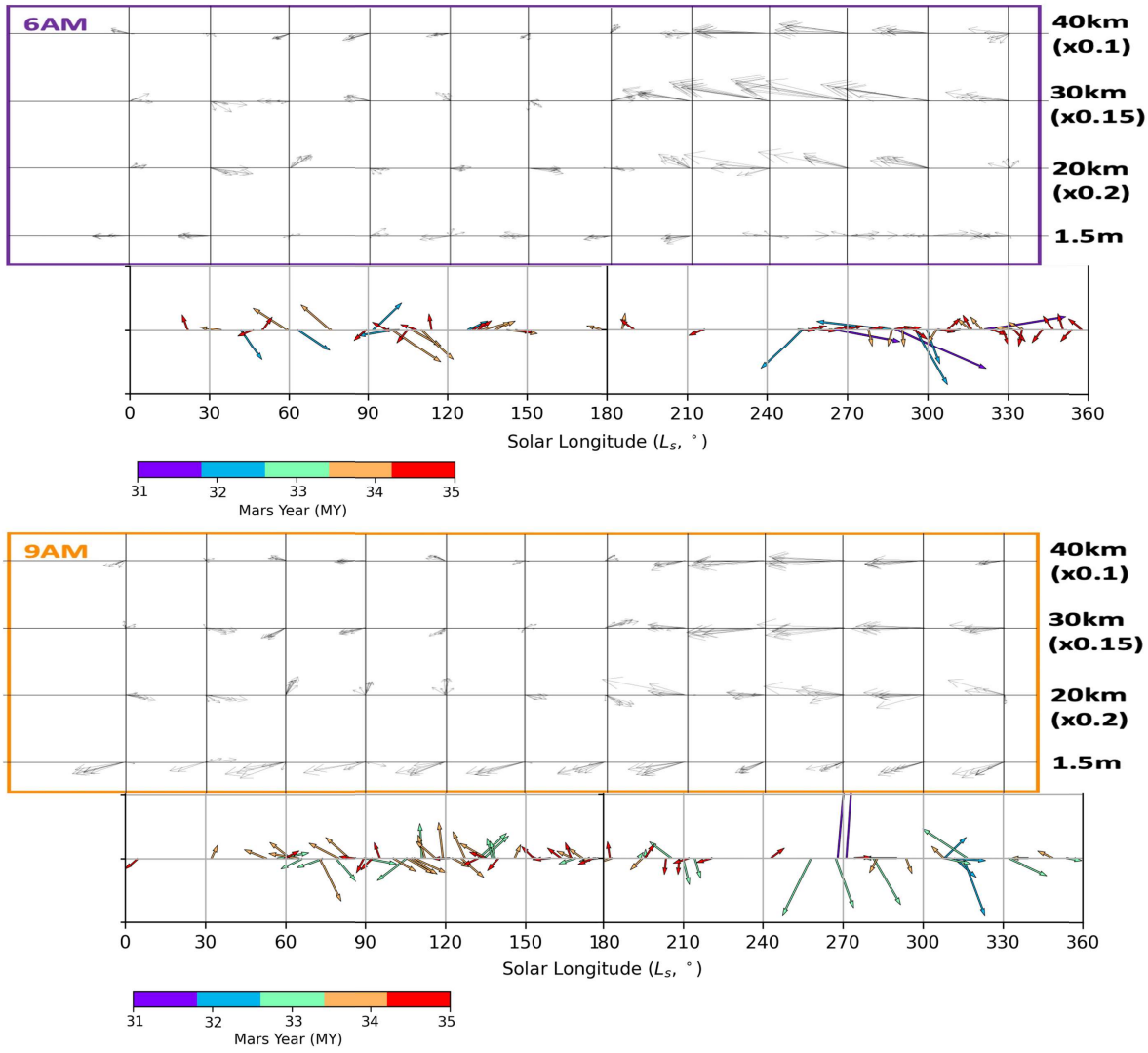

Figure 2.17: MarsWRF wind speed and direction results during AM timebins (each panel, above) as compared to ZM wind speed and direction results (each panel, below). The ZM winds were graphed in the same manner as the modelled results where the wind direction is represented by the direction of the arrow (up = North) and the length of the arrow is the speed of that wind observation. The ZM wind speed and direction arrows are combined from multiple MYs with the specific MY indicated by the colour of the arrow.

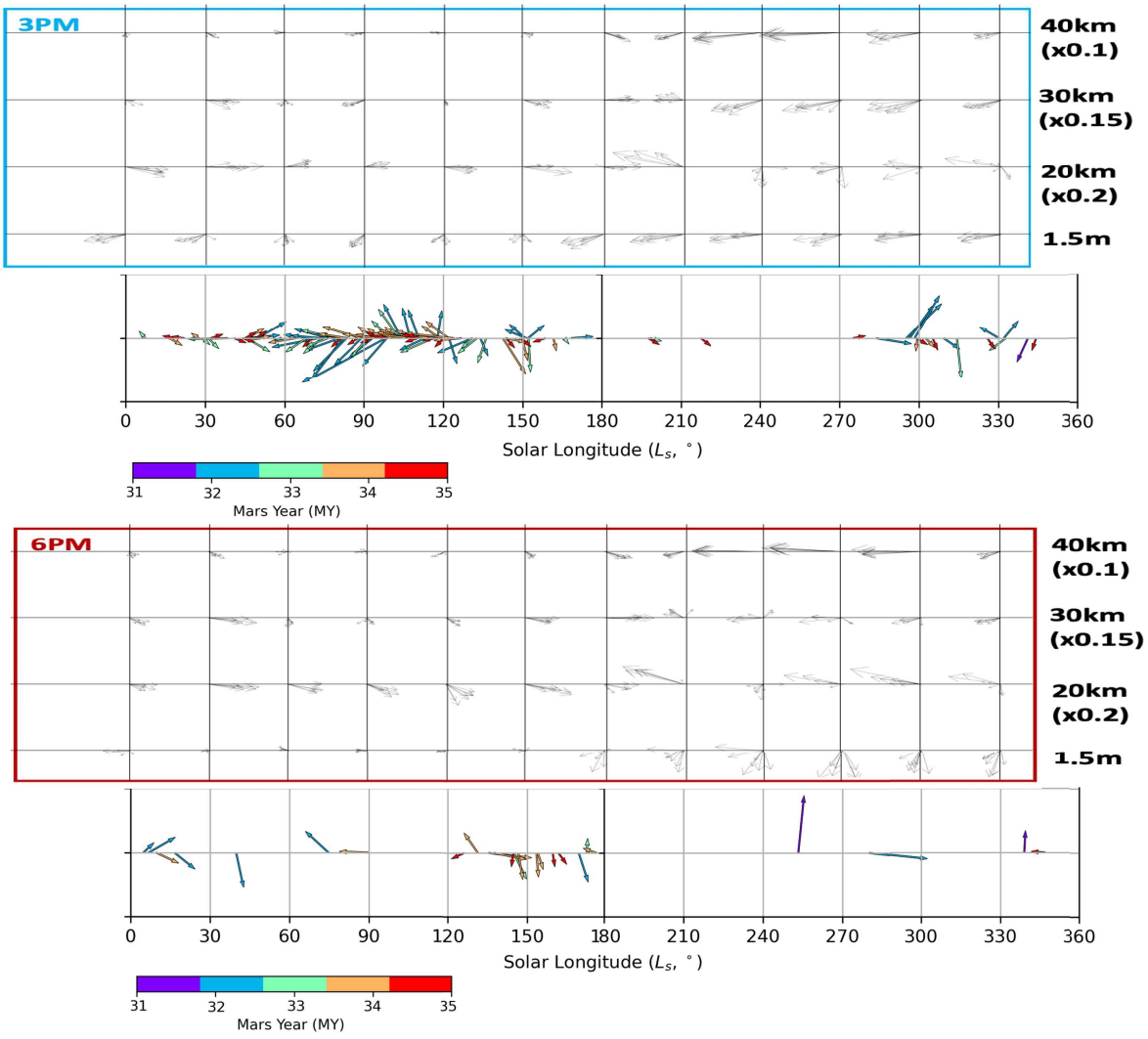

Figure 2.18: MarsWRF wind speed and direction results during PM timebins (each panel, above) as compared to ZM wind speed and direction results (each panel, below). These results are graphed in the same manner as Figure 2.17.

During the ACB season, the modelled MarsWRF wind directions and speed agreed well with the ZM results. The 15:00 timeslot had the most ZMs and the clearest Easterly heading which matched with altitudes at 30 km or 40 km. This agrees with results from Campbell et al. (2020) that calculated altitudes ranging 15-40 km for water-ice clouds at Gale. However, this correlation is less strong during the dusty perihelion season. Wind directions from dust aerosols in this season were variable and did not agree with modelled results at any altitude. This disagreement could be due to fewer movies being acquired during this season. The higher wind speeds seen in the ZMs during the dust season do seem to agree with modelled results at higher altitudes.

Wind directions of aloft aerosols observed in imagery at Gale crater gives an understanding into middle atmosphere aerosol movement and how it differs from both measured surface results (REMS) and modelled results (MarsWRF). With limited amount of wind data returned from Mars for aerosols in the middle atmosphere, the ZMs provide a long-term record of dust and water-ice transportation at their respective seasons. Therefore, these results can not only help understand how the Martian atmosphere behaves at the tropics, but can also be used to increase the accuracy of Mars GCMs wind behaviour.

2.3.2 The InSight Lander

Figure 2.19 (top) documents all of the sets of InSight images that were turned into an atmospheric movie. For each one of these datasets, there were at least 3 frames in close enough time (< 900 s) together to form a movie. Any movie that had observable aerosols and analyzed further for wind direction. These are notated in Figure 2.19 by the gray circles while the red circles were movies with no aerosols. Arrows on the gray circles represent the direction the winds are travelling towards. A total of 20 movies were analyzed and all were located in the Aphelion season (L_s 0°-180°). This is due to the significant increase of water-ice opacity from the ACB, which makes water-ice clouds more visible at this time of the year. Furthermore, because the ICC is not optimized for atmospheric observation and also includes significant rover and mars surface foreground in each image, it is not as sensitive to the presence of aerosols. Figure 2.19 (bottom) is included to provide a closer look at just the InSight movies with measured wind direction. A wind rose plot was also created

with the InSight wind data as shown in Figure 2.20. Overall results show a strong Easterly dependence with $> 65\%$ of the dataset being between from NE and SE (towards SW to NW), which agrees with Hadley cell circulation for that season (Haberle, 2003). With no wind directions measured in the Perihelion season, we are unable to determine any seasonal patterns.

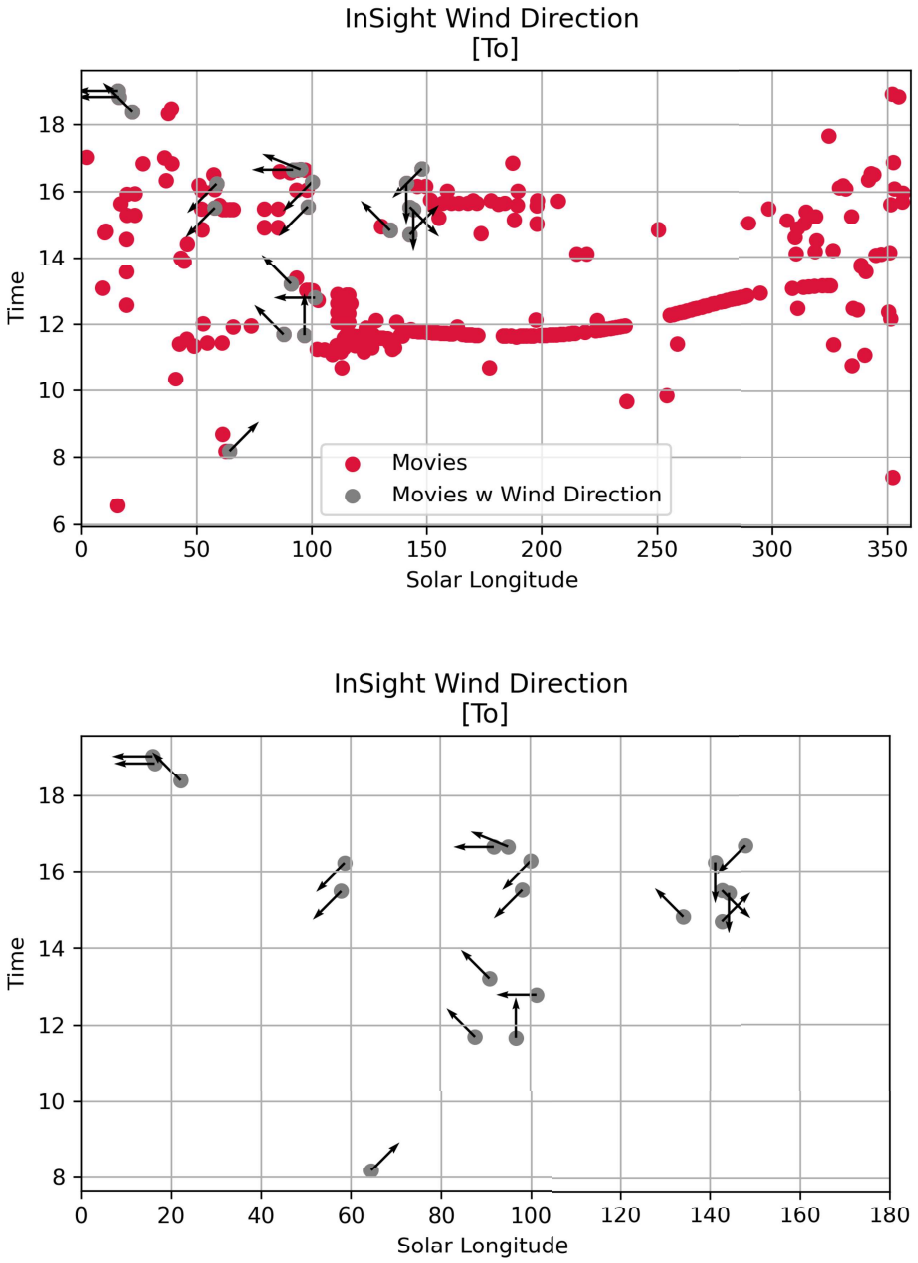

Figure 2.19: Results from InSight movies investigating aerosol movement. Top: The whole dataset with the wind direction results superimposed. Bottom: Only movies with wind directions are shown. The direction of the arrow represents the direction towards which the winds travelling, with an arrow pointing to the top meaning southerly winds is travelling towards the North. Wind directions were only recorded for InSight movies within the Aphelion season so the x-axis reflects that change.

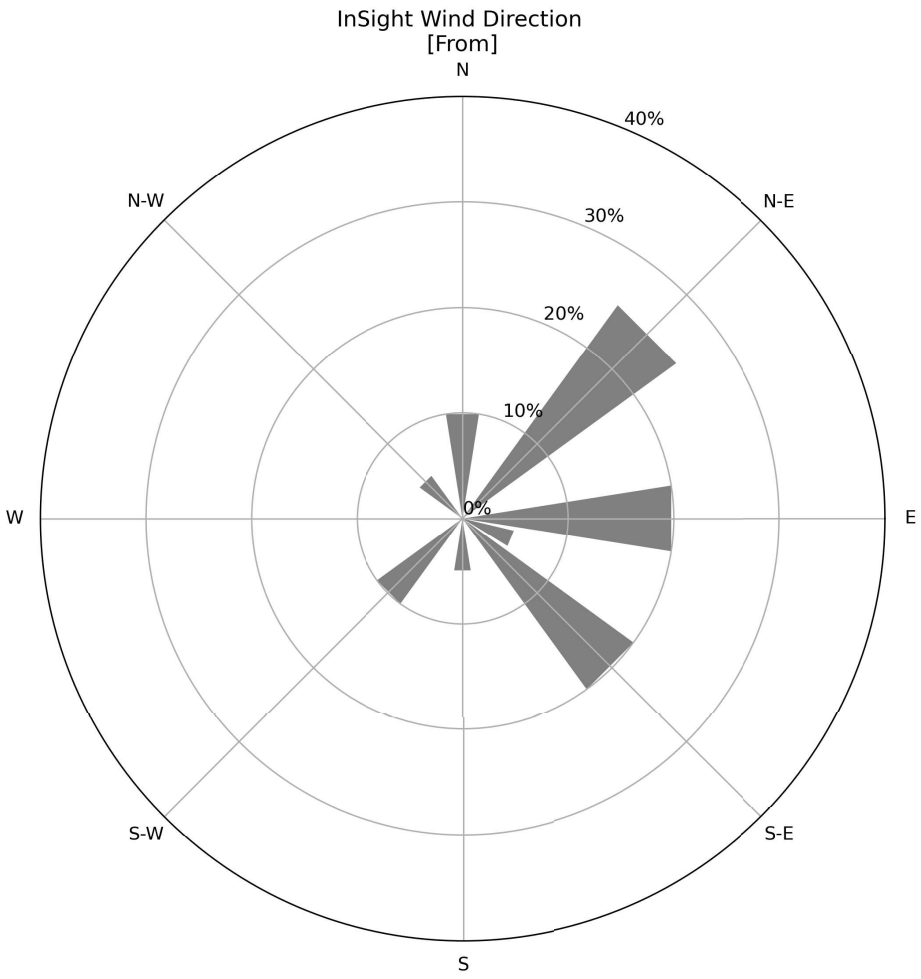

Figure 2.20: InSight wind direction results in the form of a wind rose. Each circle within the rose represents the % of data that have that direction within the dataset. For example, 20% of the movies in this dataset have aerosols moving from the East, comparable to results from MSL from the Aphelion season.

To verify results from the ICC, data from the TWINS instrument was used. With no published TWINS data available, we analyzed the raw wind direction values for this work. This will enable a comparison between near-surface winds from TWINS from aloft winds from the ICC. The flat, smooth landing site of InSight indicates that local winds could be primarily governed by large scale circulation (Spiga et al., 2018) rather than the topography driven winds measured by REMS on MSL (Newman et al., 2017, Viúdez-Moreiras et al., 2019). Thus, wind directions observed by TWINS may be more similar to winds observed by the ICC.

The raw TWINS data was provided by Emily Mason and included every TWINS measurement for the first 500 sols of operation, which encompassed the Aphelion season and the ICC data. To determine which data was the most accurate, the raw data also included operational flags that ascertains the state of the instrument when measurements were acquired. To ensure that any wind directions retrieved were reliable, data was only included when Flags 2, 3, 4 and 5 in Table 21 from Banfield, 2019 (Figure 2.21) were equal to 1. This meant that both booms were on and wind was in fact from the front of the lander. We narrowed down the TWINS dataset even further by looking at 30° L_s timesteps.

Table 21 Wind Sensor Model Data Operational Flags

Flag	Factor	Values	Description
0	ASIC temperature	0 = out of operational range 1 = in operational range	If ASIC temperature is out of its operational range, the ASIC won't work properly, and neither the Wind Sensor.
1	Frequency	0 = low rate (less than 1Hz) 1 = high rate (1 Hz)	When only low rate data are available, wind data cannot be determined reliably.
2	Boom -Y on	0 = boom -Y is off 1 = boom -Y is on	Wind accuracy is less reliable when only one boom is active, and wind is coming from the rear of that boom. Data are more accurate
3	Boom +Y on	0 = boom +Y is off 1 = boom +Y is on	
4	Front wind boom -Y	0 = wind not coming from the front of boom -Y or boom -Y off	
		1 = wind coming from the front of boom –Y	when both booms are used, since they will cover a wider range of optimal wind directions.
5	Front wind boom +Y	0 = wind not coming from the front of boom +Y or boom +Y off 1 = wind coming from the front of boom +Y	

Figure 2.21: Table 21 from Banfield, 2019 describing the operational flags used for the TWINS data. Wind data with Flags 2, 3, 4 and 5 were included in our TWINS analysis as it meant that both TWINS booms were operational and measuring winds at that time.

Figure 2.22 and 2.23 shows all the TWINS values for the Aphelion season (Ls 0-180) with the x-axis showing time of sol and wind direction on the y-axis. We plotted the mean TWINS value (black line) to

find the average wind direction over the course of a sol. Error bars for the mean values are the standard deviation. The ICC values (red) were also included with the TWINS data and include a 45° error bar. TWINS wind direction results show a consistent wind direction in the morning while the afternoon had more varying directions. When investigating how well ICC and TWINS results agreed, there was an overall agreement but the limited amount of both TWINS and ICC results limited the comparison. Unfortunately resources did not enable TWINS measurements as often later in the mission in comparison to the beginning of the mission and thus it was difficult to compare to ICC results.

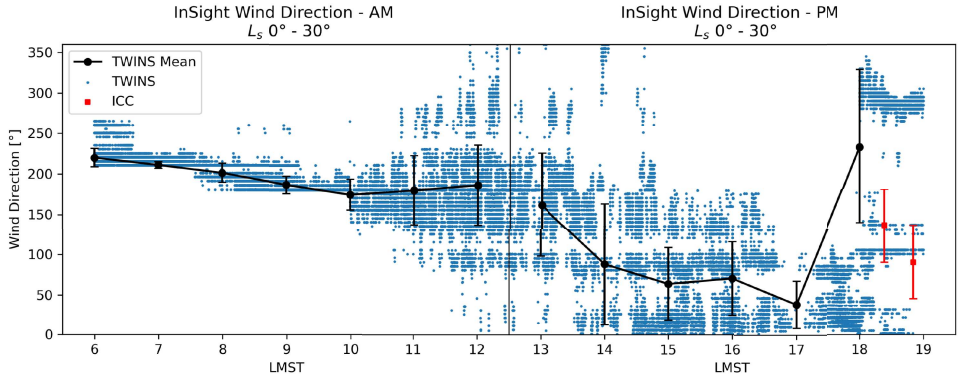

(a) L_s 0-°30°

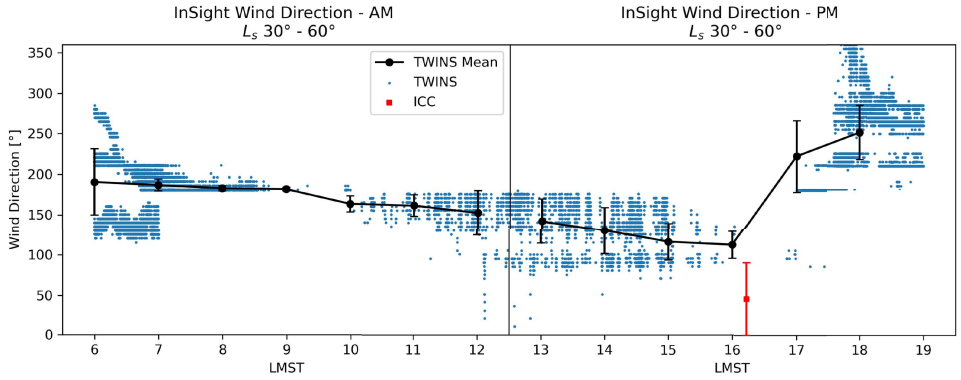

(b) L_s 30°-60°

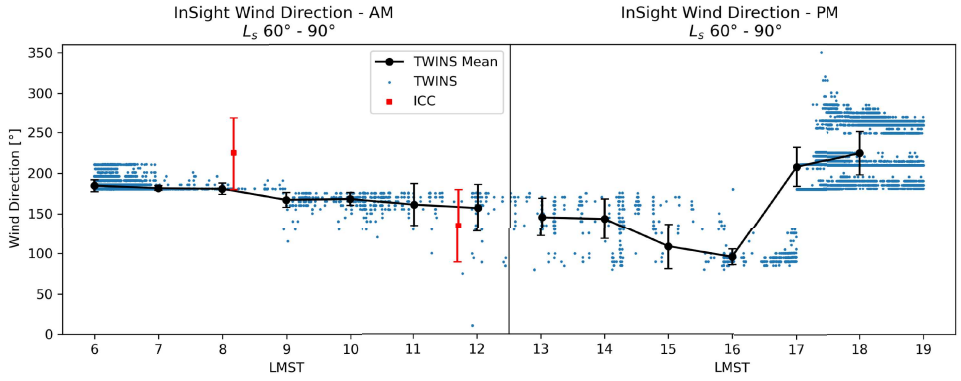

(c) L_s 60°-90°

Figure 2.22: TWINS results from L_s 0°-90° shown in black with ICC results shown in red.

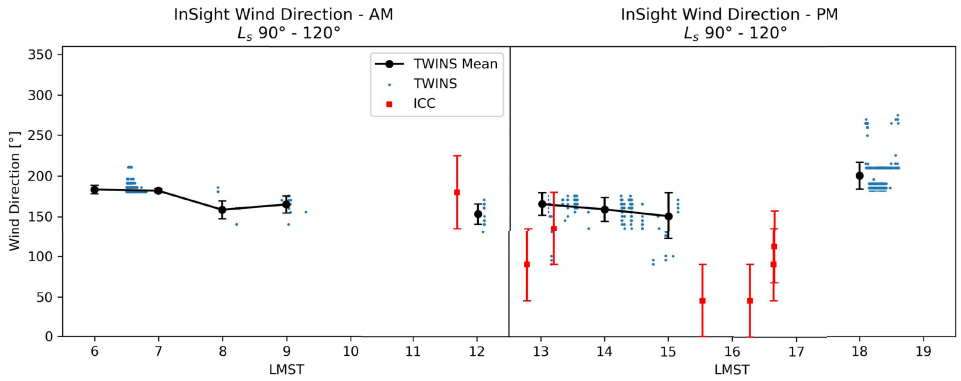

(a) L_s 90°-120°

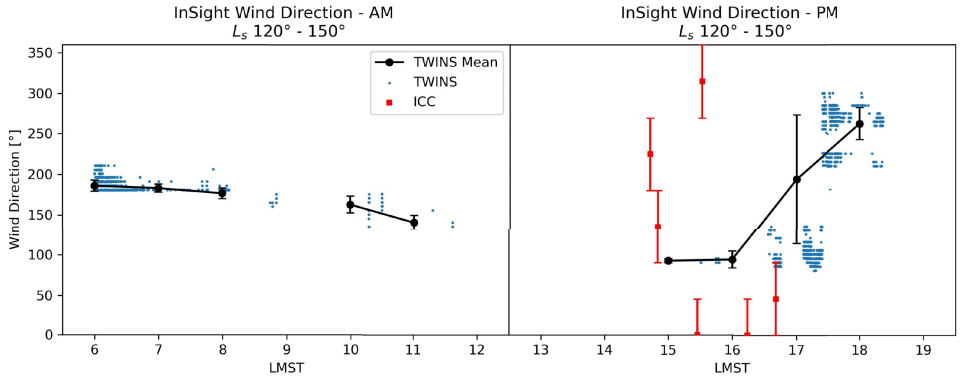

(b) L_s 120°-150°

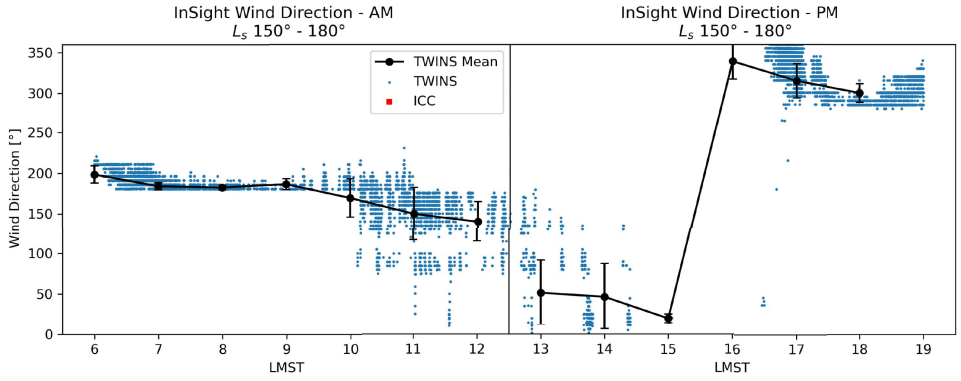

(c) L_s 150°-180°

Figure 2.23: TWINS results from L_s 90°-180° shown in black with ICC results shown in red.

The relative agreement between TWINS and ICC results indicates that near-surface winds and aloft winds could be governed by the same circulation method. This agrees with Spiga et al. (2018) where their modelled

results showed stable wind directions that were governed by general circulation due to the featureless nature of Elysium Planitia. With the majority of the wind directions observed by the ICC to be Easterly (Figure 2.20) this agrees with the large scale Hadley cell circulation that was modelled to have Easterly winds (Haberle, 2003). If the landing sites of InSight and MSL are close enough together to experience similar global dynamics, aerosols aloft may exhibit similar directions.

2.3.3 Comparison between MSL and InSight

The close proximity between the MSL and InSight landing sites provide a unique opportunity to compare results from Sections 2.3.1 and 2.3.2. Figure 2.24 and 2.25 show the nine InSight observations that had a corresponding MSL observation in close enough L_s. Table 2.2 shows the wind direction for each compared pair of observations. Results from both missions show aerosols moving in similar directions at similar times of sol and year. The observation matches are only during the Aphleion season, when water-ice clouds are strong (Clancy et al., 1996, Smith et al., 2004). InSight and MSL are within 600 km of each other and border the equator, within the 10°S–30°N range of the ACB measured by Clancy et al. (1996). With InSight and MSL observing similar movement of water-ice clouds in the ACB season, this indicates that InSight and MSL are likely observing similar global atmospheric dynamics that is governing the movement of aerosols (e.g. Hadley cell circulation).

Table 2.2: A table of the InSight and MSL movies that were taken on the same sol. Matches were made based on similar L_s values ($\pm 0.5^\circ$)

MY	**Ls**	**Time (InSight)**	**Time (MSL)**	**InSight WD [from]**	**MSL WD [from]**
34	309.19	18.935	12.82	0	90
35	15.83	19.021	14.63	90	315
35	22.12	18.385	18.37	135	90
35	58.64	16.225	14.67	45	90
35	64.33	8.182	8.58	225	225
35	87.76	11.692	15.28	135	67
35	90.96	13.21	11.88	135	135
35	95.12	16.657	15.25	112	112
35	142.66	14.712	13.73	225	225
35	142.68	15.524	13.73	315	225

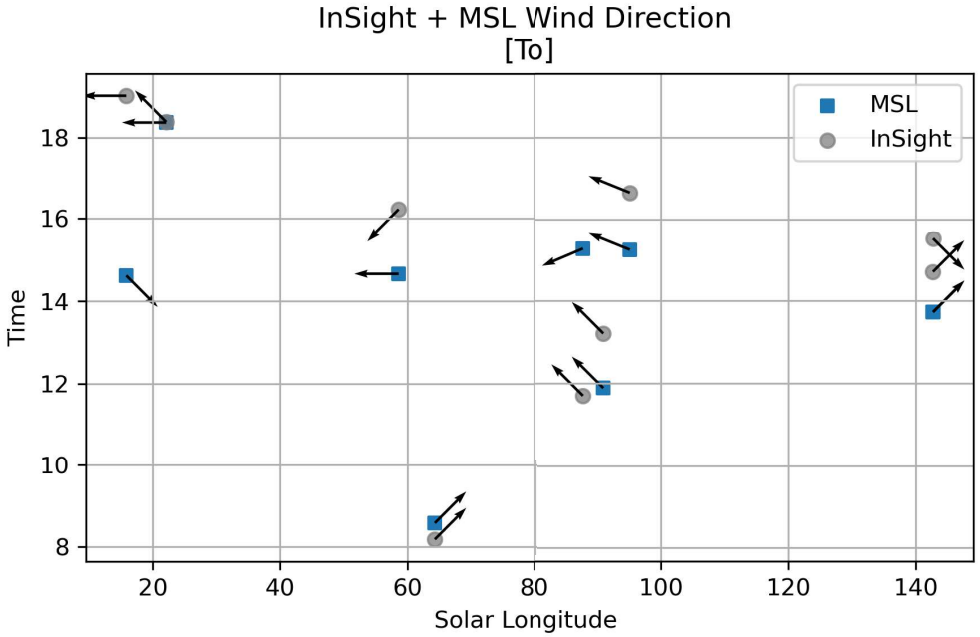

Figure 2.24: Results showcase MSL (blue) and InSight (grey). Results that are close in time on this diagram agree with each other, which indicate that MSL and InSight are observing aerosols driven by similar circulation dynamics. The arrows represent the direction towards which the winds are travelling, with up indicating aerosols travelling towards North.

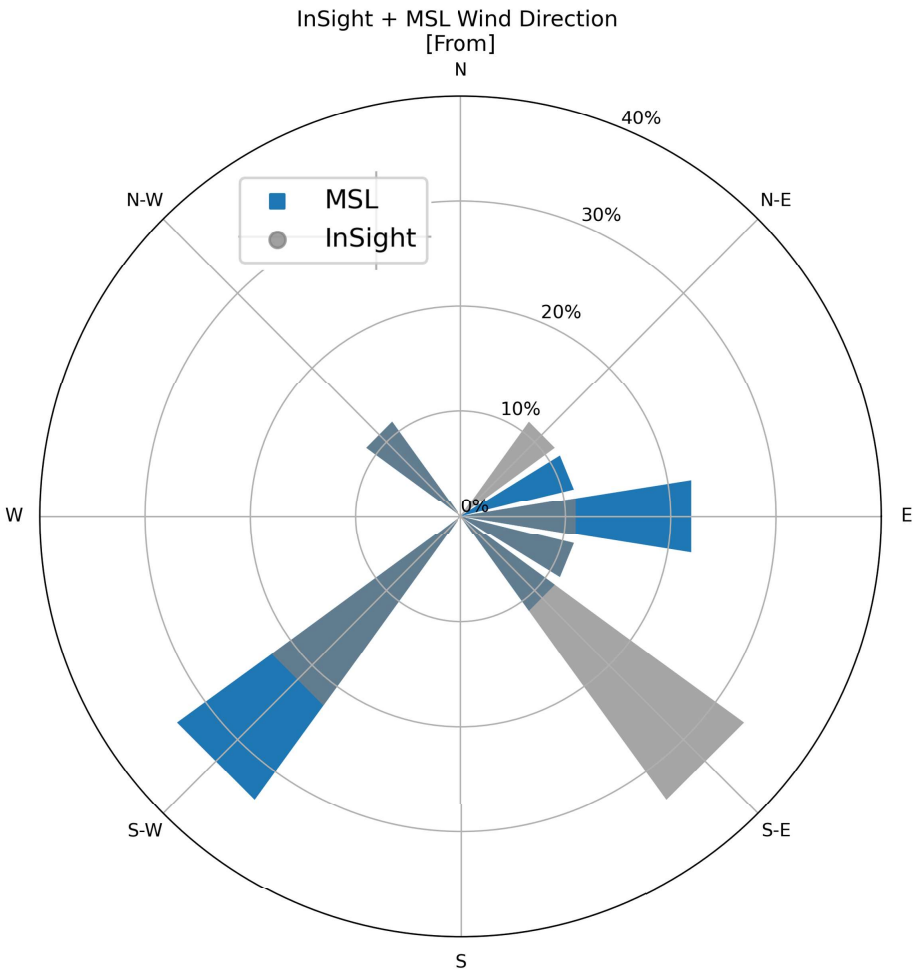

Figure 2.25: Wind rose plot of InSight and MSL results in the same manner as previous wind rose plots. However, since wind speed was not deducible in InSight results the colours represent the MSL (blue) and InSight (grey) missions. Results compare well with one another, with SW winds predominating.

2.4 Conclusions

Martian winds were observed through moving aerosols in imagery acquired by the MSL and InSight missions. Even though only nine observations were able to be matched directly between the two missions, they strongly suggest that both sites are viewing the same large scale circulation. This is extremely useful for helping to determine how aerosols observed by ZMs at Gale crater are affected by a topographical feature (Aeolis Mons)

as winds measured by REMS signify strong local dynamics that overtake large scale circulation (Newman et al., 2017, Viúdez-Moreiras et al., 2019). Yet, wind directions between ZMs and REMS were not in agreement indicating that ZM aerosols must be above Aeolis Mons. With InSight's landing location being on the flat plains, circulation is only driven by large scale circulation and thus there isn't much difference between near-surface winds measured by TWINS and those observed by ICC imagery. This agreed with modelled results (Spiga et al., 2018). Therefore, if MSL is also observing similar wind directions as InSight then this gives greater confidence that aerosols observed at Gale crater are aloft in the middle atmosphere as predicted by others (Kloos et al., 2016, Moores et al., 2015b) and later demonstrated through shadow analysis imagery (Campbell et al., 2020). As a result, the surface-level wind observations being made by REMS and the ZM dataset complement one another, giving data on different parts of the atmosphere simultaneously.

Overall, understanding winds aloft in the middle atmosphere of Mars is useful for understanding how circulation processes affect local conditions. By comparing these two missions, one in a crater and one outside, we can see how well topography affects aerosol activity. However, with only nine matched observations between InSight and MSL, it is difficult to be conclusive about our results. This is especially true for the Perihelion season where no matching pairs of observations could be considered in our analysis.

3 Investigating an Automated Analysis Approach for Aerosol Movement in Martian Surface Imagery

3.1 Overview

As discussed in Chapter 2, surface spacecraft imagery is useful for gathering information on meteorological parameters, such as wind direction. However, most of these observations are collected on a minimal cadence due a variety of factors such as data volume, priority, etc. This impedes the number of data points acquired, limiting Martian atmospheric scientist's understanding of the lower atmosphere. Currently, Global Circulation Models (GCMs) are used to fill in those blanks, but they must also be validated using actual data. This creates a feedback loop which ultimately requires finding new ways to better obtain surface data. In this case, better data means not only more frequently obtained data, but also data acquired at a wider range of geographic locations on Mars. For instance, Haberle and Catling (1996) suggest that at least 15 geographically well-dispersed stations are needed to verify a GCM.

The Mars Science Laboratory (MSL, Curiosity) mission continues to add to its atmospheric movie dataset collection that began in August 2012 after landing in Gale crater. Even with this large accumulation of observations, atmospheric movies are only acquired 1-2 times per week due to the large data volume required to send the images back to Earth to then be analysed by a human operator. This limits how much data can be returned and used to validate GCMs. Previous work by Francis et al. (2014) explored whether automated analysis on imagery from the Phoenix mission could be used to find wind parameters. Their automated results were comparable to wind vectors observed by human operators for the Phoenix atmospheric movies.

This suggested that automated analysis could also be successful with MSL movies (Francis et al., 2014), which was later confirmed by Campbell et al. (2021) who explored automated analysis as a plausible option for MSL atmospheric movies. This chapter describes the Campbell et al. (2021) study.

With collaboration with a team from Curtin University, Onboard Rover Cloud Algorithm (ORCA) was created and tested with the Zenith Movie (ZM) dataset from MSL to determine whether such an algorithm could viably be deployed on a Martian surface mission. This algorithm uses a hybrid approach that includes Computer Vision (CV) and Machine Learning (ML) techniques to determine wind direction and angular wind velocity based on how aerosols move over the course of a movie (Campbell et al., 2021). Using this algorithm as a pre-processing step would significantly reduce downlinked data volume by having the spacecraft process the movie itself and simply return a string of values. Therefore, the implementation of ORCA on future spacecraft could increase an observation's cadence and thus drastically increases our understanding of the Martian atmosphere from the surface.

3.1.1 Author Contribution

For this Chapter of the dissertation, the goal was to explore computation methods to that could be useful for studying imagery of Martian aerosols. In order for me to find wind parameters of aerosols taken with MSL, I would manually watch the frames and calculate the direction and pixel distance. This takes a good amount of time and in some cases, aerosols are too thin for me to distinguish by eye alone. This difficulty was higher in the dust seasons when chaotic motion also made it harder for me to distinguish aerosol movement. The dust season already has the minimal cadence for acquiring movies due to mission operation constraints such as data volume. However, these movies are also extremely useful for understanding aloft winds that heavily relies on GCMs. Thus it is important to determine how to expand this type of observation to allow a greater cadence while minimizing human operator effort to speed up analysis. My supervisor and I explored the option of using Machine Learning techniques to calculate aerosol movement, which was previously investigated for movies from the Phoenix mission (Francis et al., 2014) and could be tested with the MSL movies.

In order to investigate this type of project, we wanted to find collaborators that had an expertise in

Machine Learning computational methods. We brought our expertise in Martian aerosols and the imagery associated with capturing their movement but wanted to outsource the computational side. This lead us to collaborating with a team at Curtin university with the expertise applying automated analysis to planetary imagery. We agreed that they would be responsible for developing and training an algorithm to calculate the wind direction and distance of Martian aerosols while I provided the dataset that would be used to train the algorithm.

Once the algorithm was created and trained by the Curtin group using atmospheric movies, they gave me the Python code to run on a larger set of atmospheric movies. My previously published work (see Campbell et al. (2020)) had tallied the wind direction and angular distance that aerosols moved in a set of MSL movies. This was the perfect dataset to use with the Curtin alogrithm. I gathered all the movies, ran the algoirthm on each one and lead the analysis of the results. The Curtin group was helpful on determining what needed to be improved with the algorithm in order to increase the algorithm's accuracy with calculating the same values I found manually in Campbell et al. (2020). However, it showed promising results for movies with strong aerosol features and we decided to publish our results in Acta Astronautica (see Campbell et al. (2021). I lead the paper which included generating plots to showcase the accuracy with the algorithm while the Curtin group provided the writing for how the algorithm worked. The results from this Chapter will showcase the results from the Campbell et al. (2021) paper.

3.2 Methods

3.2.1 The Onboard Rover Cloud Algorithm (ORCA)

The algorithm, noted as ORCA, used in this dissertation was developed by a team at Curtin university and tested with movies from the MSL mission provided by myself. Laid out in (Campbell et al., 2021), a variety of CV techniques were used by the Curtin team to estimate the velocity field of moving objects in a successive images. To understand which CV techniques should be studied, examples using terrestrial and planetary cloud analysis were examined by the Curtin group and implemented into ORCA. This included

terrestial cloud motion estimation via optical flow (Cros et al., 2014, Zaher et al., 2017) and particle image velocimetry through Akatsuki orbiter imagery of Venus clouds (Horinouchi et al., 2017). Choi et al. (2007) showed promising results mapping out wind velocities for Jupiter's Great Red Spot from Galileo orbital imagery by using an automated algorithm. However, these CV examples rely on denser clouds, while Martian clouds are thinner and don't show as clear patterns as clouds on Jupiter or Venus. Therefore, the team at Curtin utilized a two-stage hybrid CV and Machine Learning (ML) approach to allow the algorithm to understand how to work with the thin Martian water-ice clouds observed by MSL.

To fully train ORCA, the Curtin team needed to create training data that was independent of the MSL data in order to synthesize a non-uniform velocity field with local motion and features. This training set comprised of 2000 images and were composed of chroma, brightness and hue, and random noise of varying intensity (Campbell et al., 2021). This is intended to analyze Mean-Frame Subtraction (MFS) imagery from MSL (see Section 2.1.1) that has a more 'granulated'-like view. After ORCA was fully trained by the Curtin team, it was quickly tested with a subset of MSL movies provided by myself that had typical conditions such as strong aerosols or no aerosols. Once proving viability with that set, it was used with a set of movies previously analyzed manually for wind parameters (direction and angular velocity). This set of 114 ZMs was previously published for wind parameters (Campbell et al., 2020) and became the stepping stone for testing ORCA with actual Martian movies. The ORCA pipeline for estimating cloud parameters in ZMs is shown in Figure 3.1.

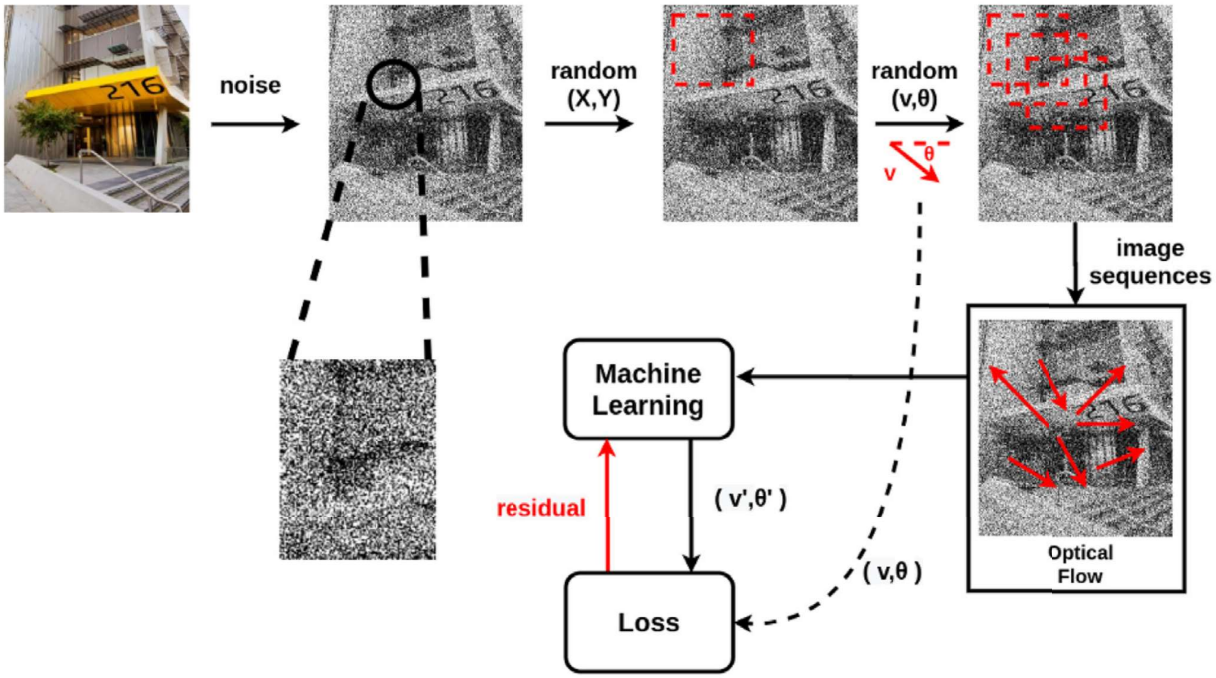

Figure 3.1: Figure 3.1 in (Campbell et al., 2021) showcases the pipeline that the Curtin team utilized to create and train ORCA for automated Martian aerosol movement analysis.

3.2.2 The Mars Science Laboratory (MSL) Mission Zenith Movie (ZM) Dataset

To test on a Martian dataset, wind results from Campbell et al. (2020) was used. This utilized the ZM (Figure 2.8) due to its vertical pointing and finds both meteorological wind direction and pixel distance from observed aerosol movement. Details on the ZM and determining these two parameters is described in Chapter 2.2.1. Note that movies in this Chapter have been processed using the MFS technique discussed in Chapter 2.2.1. There is a total of 114 ZMs from sol 193 (L_s 268°, MY 32) to sol 2010 (L_s 153°, MY 34) in this dataset (Campbell et al., 2020; 2021).

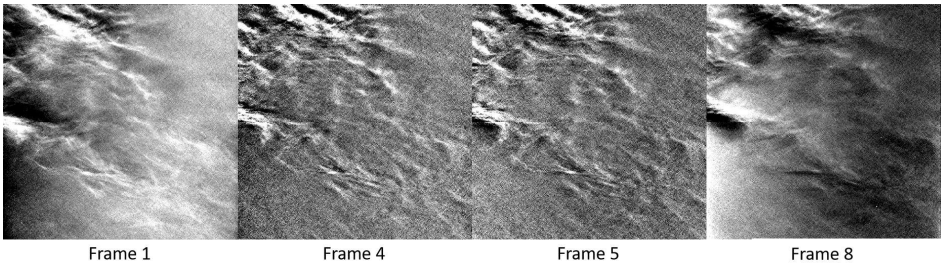

Figure 3.2: An example of a Zenith Movie (ZM) processed using the Mean-Frame Subtraction technique as discussed in Chapter 2.2.1. MFS processing helps bring out more features to analyze within the movie, which in this case is thin wispy clouds. A raw example can be seen in Figure 2.8.

3.2.3 Applying the Algorithm to ZMs Acquired by MSL

To apply ORCA to the ZM dataset, each ZM was inputted into ORCA which returned a wind direction, pixel distance and a copy of the same ZM with an overlaid arrow. The overlaid arrow shows the direction the aerosols are moving towards and the size of the arrow shows the pixel distance. The Curtin team developed two individual models that were used to train and compute each parameter (wind direction and pixel distance) to ensure more accurate results compared to a single model that does both. This also lets us investigate which parameter ORCA excels or struggles with and focus any improvements on that. The first model produces the arrow that points in the direction towards which aerosols are moving (wind direction). The second model also produces an arrow but the length of the arrow represents the distance the aerosols moved (pixel distance). The larger the arrow, the greater distance the aerosols moved. The algorithm calculates each parameter for each frame and returns a mean value as the overall value for the movie.

For a direct comparison to Campbell et al. (2020), the pixel distance values calculated by the algorithm were converted to an angular velocity by dividing by the average duration of a ZM ($\sim$235 seconds). Considering the FOV of the NCAM ($45^\circ \times 45^\circ$), and the pixel size of the frame (512 pixel $\times$ 512 pixel) allows a conversion of degree per pixel to angular distance.

For each parameter the root mean squared deviation [3.1] is calculated. This provides a measure of

confidence in the algorithm for each parameter calculated. For each movie, the standard deviation [3.2] is calculated to determine how the mean value varies with respect to the value calculated per frame.

Since wind direction has a periodic boundary around 0° and 359° this had to be taken into account when calculating the standard deviation. This means that wind direction values that fluctuated around north could result in incorrect standard deviations. Computing with equations 3.1,3.2 the difference between 5° and 355° wind directions would be larger than expected (350 °) even though both values represent Northerly directions and thus the difference is actually 10°. To combat this, wind directions that rotated around north (300°-60°) were separated and analyzed by making the fluctuating boundary 180°. An example of this would be if two wind directions were 355° and 5° then their values would be 175° and 185° respectively. Therefore the difference between these two directions is the correct 10°. Any wind direction outside of that range (300°-60°) was left as is for standard deviation calculations.

$$\text{Root-Mean Square Deviation} = \sqrt{\sum_{i=1}^{n} \frac{(y_{i,auto} - y_{i,manual})^2}{n}} \tag{3.1}$$

$$\text{Standard Deviation} = \sqrt{\sum_{i=1}^{n} \frac{(y_i - y_{mean})^2}{n}} \tag{3.2}$$

3.3 Results and Discussion

We investigated the results for each parameter (wind direction and angular wind velocity) to determine how the algorithm performed in each case. To determine if the algorithm performs well, the standard deviation was investigated on a sol-by-sol basis and the root mean square deviation for each parameter. The standard deviation should be able to tell us how the algorithm performs in a variety of cloud conditions such as varying lighting or multiple cloud decks. How the algorithm performs for the whole set will be determined by the root mean square deviation. Figure 3.3 showcases results for wind direction comparison while Figure 3.5 shows angular wind velocity results. Error bars for the automated results are the calculated standard deviation and errors for the manual results (±5°) and are taken from Campbell et al. (2020).

3.3.1 ORCA Wind Direction Results

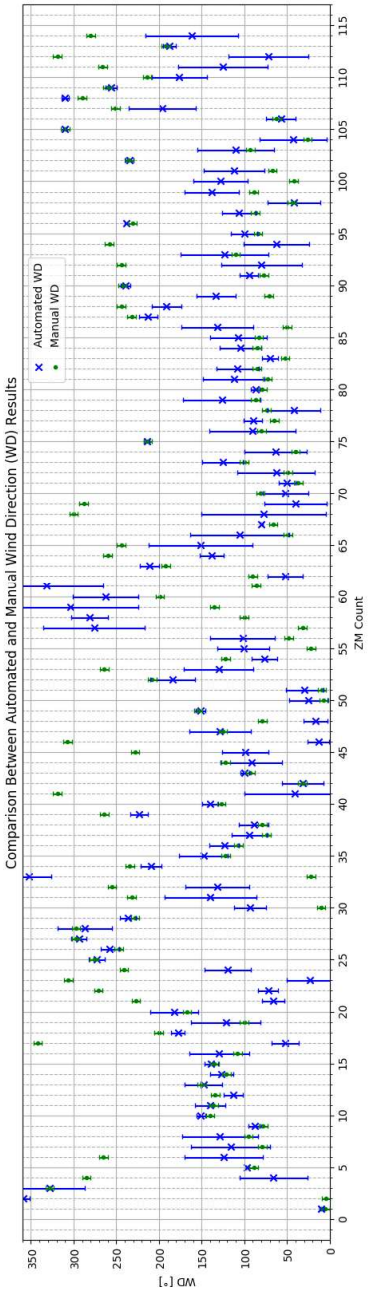

Figure 3.3: Results for automated wind direction (blue) vs manual wind direction (green). The automated error bars represent the standard deviation. The manual error bars are cited from Campbell et al. (2020) as $\pm 5°$.

The root-mean square deviation for wind direction was 67.14°. Even though this value is not close to 0° (indicating ORCA perfectly matches manually found results), it indicates that any error calculated by ORCA would at least fluctuate within roughly the same cardinal direction. For example, if manual results determined aerosols moved with a wind direction of 90° (E), then ORCA would be able to also find this wind direction within 67.14° of the manual result (90°). This range would be 22.86° (NNE) - 157.14° (SSE), still within the Easterly direction of the manual result. Yet, it would be best to explore how to lower the root-mean square deviation further to improve ORCA's wind direction results. Investigating how the algorithm performs on a sol-to-sol basis may help pick out which ZM conditions are better than others.

To determine if there are any seasonal or diurnal conditions that affect the standard deviation, we plotted versus time and solar longitude as shown in Figure 3.4. The y-axis represents the wind direction standard deviation value, thus the maximum value that the algorithm can fluctuate is by 80° During the early morning ($<$ 08:00 LTST), standard deviation values appear to be lower, indicating that ORCA performed well with clouds at this time of sol. Clouds observed in movies during these hours typically have higher opacities (Kloos et al., 2018) and strong features (Campbell et al., 2020). The consistency of movement of the aerosols from the start and end of a ZM would allow ORCA to better understand the aerosol movement with its Machine Learning and thus calculate the wind direction more accurately. When investigating standard deviation over the course of a MY, there does not appear to be any patterns on if there is a better time of a MY that ORCA can more accurately calculate wind directions. However, since the majority of the data points are within the ACB season it could be skewing how well the algorithm performs outside of that season due to the limited number of data points during the dust season. The histogram on the right side of Figure 3.4 indicates that the majority of the wind direction standard deviation values are between 5°-15° and 35°-40°. Thus, even though the root mean square deviation isn't as low as we would want, the algorithm appears to have a lot lower standard deviation values and must be investigated sol-by-sol to determine which specific aerosol conditions ORCA responds well or struggles with.

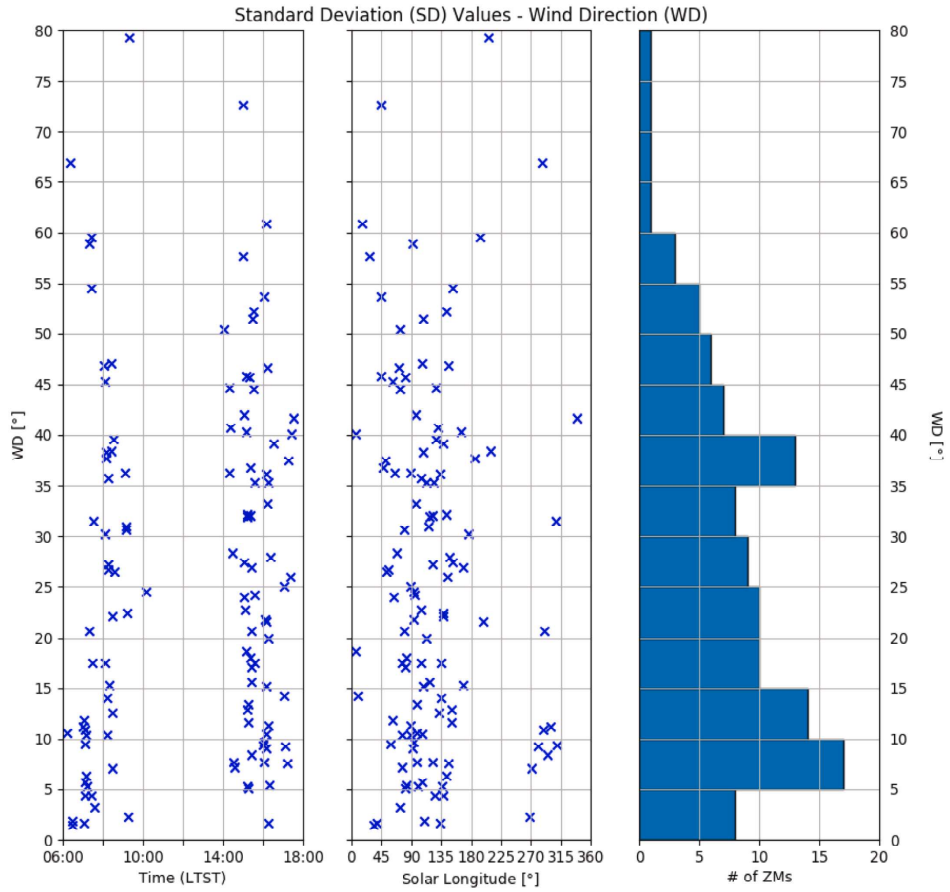

Figure 3.4: Standard deviation of wind direction for every movie in the dataset. Left investigates patterns with time (LTST), Centre investigates patterns with solar longitude, and Right is the histogram. The y-axis is the standard deviation value, thus the maximum value the algorithm fluctuated by was 80°. The majority of the standard deviation values lie between 35° and 40° or 5° and 15°.

3.3.2 ORCA Angular Wind Velocity Results

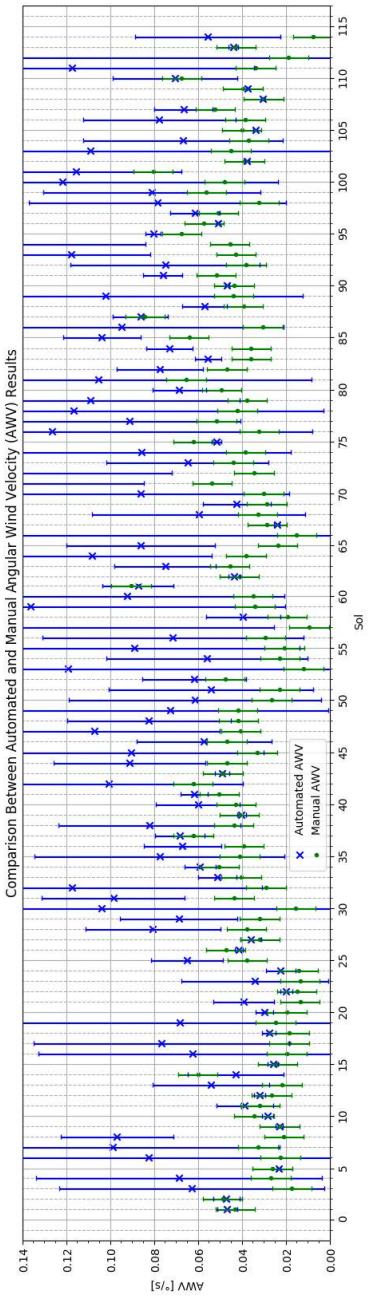

Figure 3.5: Similar to Figure 3.3, but for angular wind velocity. Error bars for manual results are cited from Campbell et al. (2020) while automated result error bars is the calculated standard deviation.

The root-mean square deviation for the angular wind velocity was 0.0518 °/s. With manual values ranging from 0.008°/s to 0.084°/s, the root-mean square deviation shows a fluctuate of at least 50% by ORCA. The angular wind velocity also needs to be trained more within ORCA to lower the root-mean square deviation. The standard deviation values for angular wind velocity are graphed in the same manner as wind direction (Figure 3.6). Morning movies appeared to have lower standard deviation which agreed with wind direction results. It appears that there are higher standard deviation values associated with the dust season, but similar to the wind direction results, that could be because we have less data points in comparison to the ACB season. Angular wind velocity standard deviation values will be investigated on a sol-by-sol basis with the wind direction standard deviation.

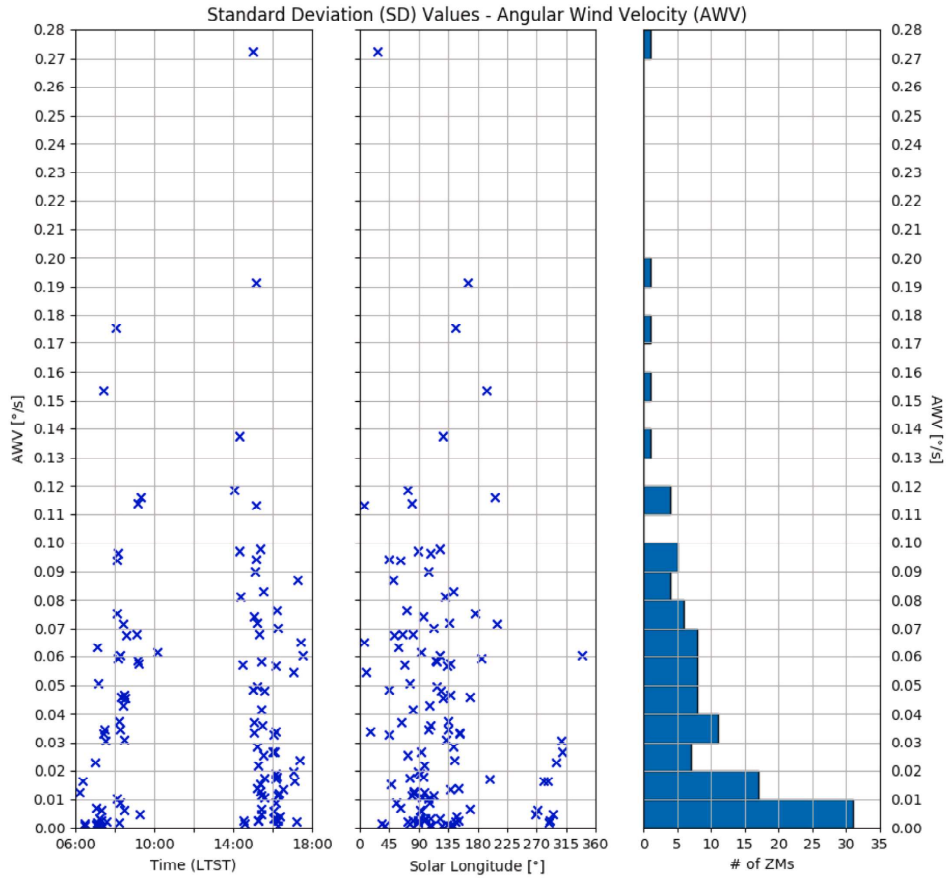

Figure 3.6: Similar to Figure 3.4, but for angular wind velocity. The maximum value the angular wind velocity could fluctuate is 0.28°/s, however, the majority of standard deviation for this parameter is lower than 0.02°/s.

3.3.3 Investigating ORCA on a Sol-by-Sol Basis

While investigating the wind direction standard deviation on a sol-by-sol basis, there was a lower value associated with clouds with strong features that stay consistent throughout the entire movie. Figure 3.7 showcases sol 1924 with strong cloud features and results that agree between manual and automated results. This was also true for the angular wind velocity results. However, ZMs that had lighting changes (Figure 3.8 or camera artifacts (Figure 3.9) had large standard deviation values.

When ZMs had lighting changes within a movie, the computed standard deviation is higher because of

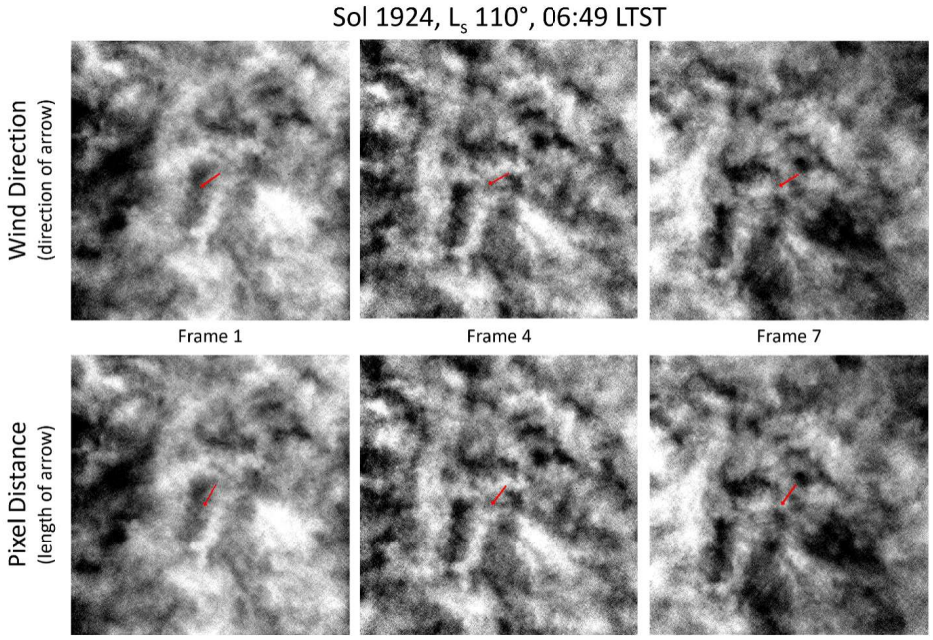

Figure 3.7: Example on Sol 1924 that has strong, consistent cloud features. The algorithm was able to measure wind direction that matched manual results. A low standard deviation is associated with this example, meaning that the automated value did not change much per frame. This is apparent in both the wind direction and pixel distance results as the arrow doesn't change much between each frame.

the differences between each individual frame calculation and the mean value. Investigating this further with Sol 310 (Figure 3.8, we noted that the automated and manual wind direction did match up well even though ORCA returned a large standard deviation. Therefore, it appears that the algorithm may be able to calculate wind direction but with a higher error. For angular wind velocity, the manual and automated wind directions do not match. Investigating this mismatch showed a significant change between the size of arrow between each frame. Even though the algorithm could possibly detect wind direction, it still needs extra training for angular wind velocity.

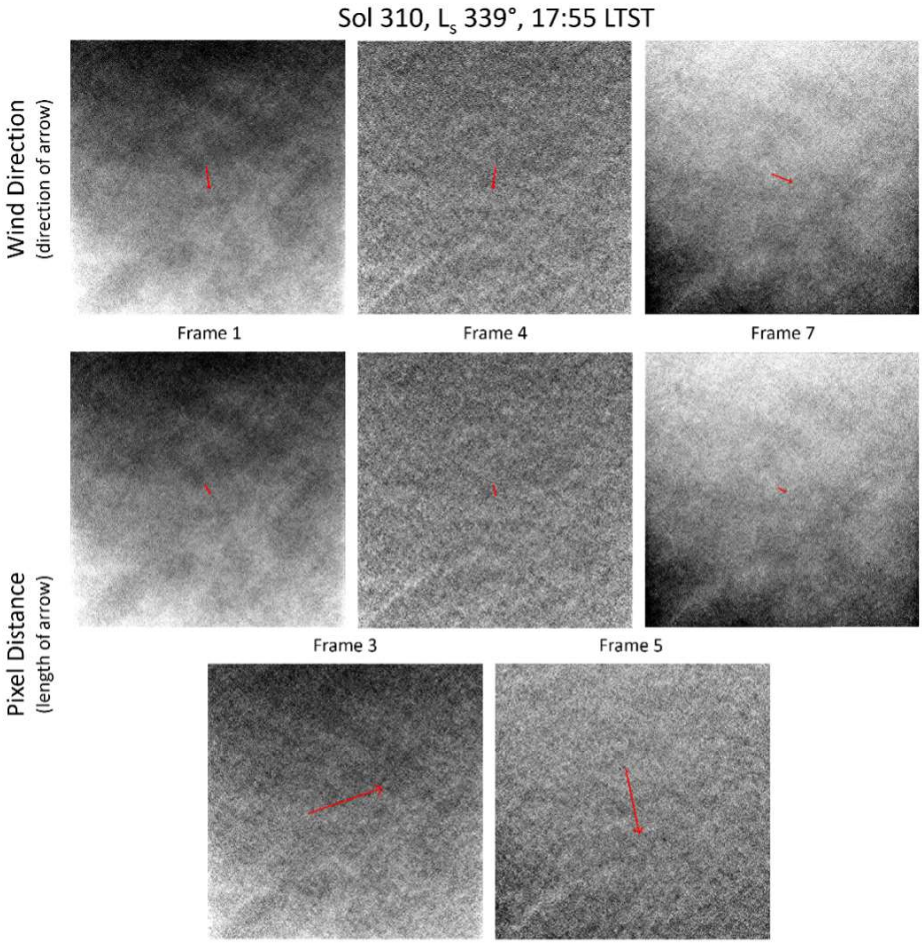

Figure 3.8: Sol 310 showing how lighting changes affect the algorithm calculations. For the wind direction, the automated (mean) value matched with manual value but had a large standard deviation. For pixel distance, the algorithm did not match manual values and had a large standard deviation, especially in frames 3 and 5. Overall this indicates that the algorithm needs more training with these types of movies.

Exploring examples with camera artifacts show that the algorithm struggles with both wind direction and angular wind velocity. The arc shown in Figure 3.9 is a common camera artifact within ZMs that display lighting changes throughout a movie. With two examples where the algorithm struggled with lighting changes (Figure 3.8 and 3.9), this error was examined further. Several factors could be contributing to the fluctuation with these lighting change examples based on how ORCA implements velocity vectors:

- Multiple flows returned for a movie could mean that ORCA averages the flow and the directional vector is the result of various local flows that ORCA measured
- Optical flow generates vectors based on intensity changes and therefore could fluctuate those vectors more if intensity changes significantly within a movie
- This type of intensity change isn't well represented in the synthetic data used to train the model and thus could be more difficult for ORCA to distinguish at first

Since it is apparent that the algorithm has a lower success rate for determining both parameters in movies with artifacts, the algorithm requires additional improvements to overcome this obstacle since it is a common feature within ZMs.

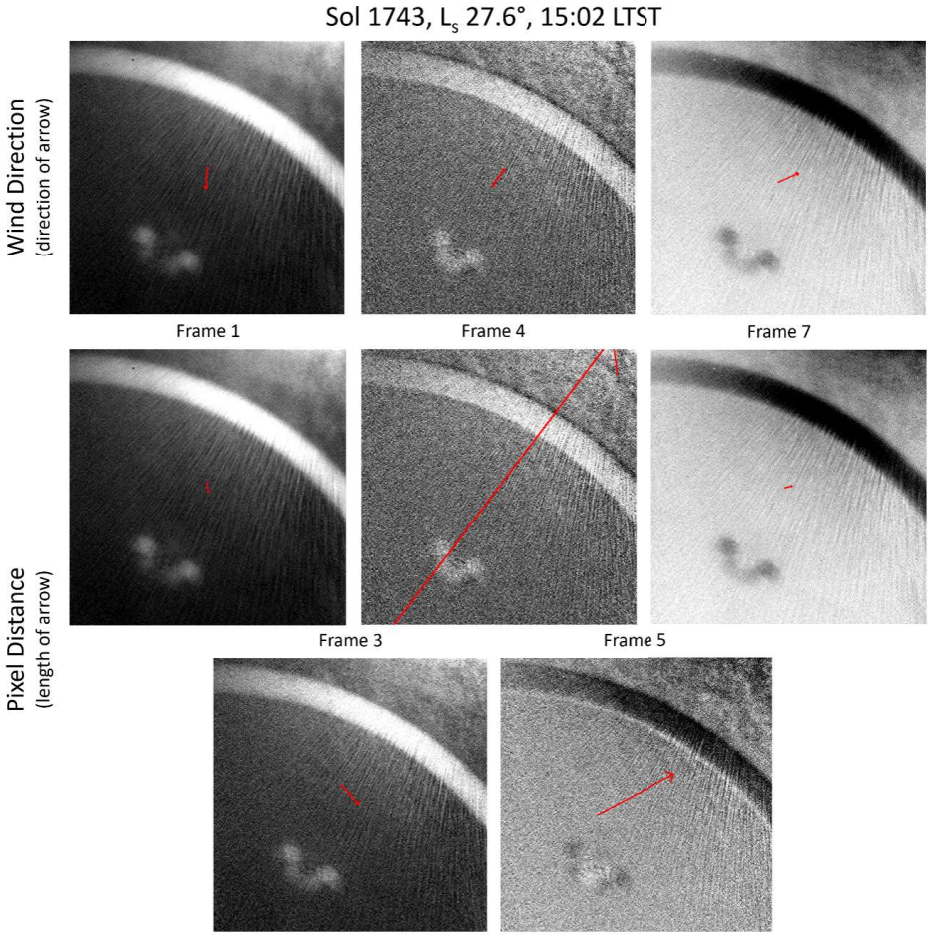

Figure 3.9: Sol 1743 is an example with a camera artifact that is common in ZMs. Both models fluctuated significantly, as shown by the varying direction or size between frames. Neither the wind direction nor the pixel distance matched with manual results, and both had high standard deviations. This high error indicates the algorithm must be trained more to ignore these artifacts

Another common feature observed in ZMs are cloud decks with different wind directions. Figure 3.10 shows an example where two cloud decks are seen moving in opposite directions. The automated wind direction seems to fluctuate between both observed directions, creating the false impression of a large variation. On the other hand, the angular wind velocity seemed to agree with manual results. Both cloud decks are moving at roughly the same velocity, which could be the reason why there is little change between

automated and manual results. However, cloud decks with different velocities could have a larger standard deviation. The algorithm would need to be trained to determine how to detect multiple cloud decks, and how to calculate parameters for one or both decks.

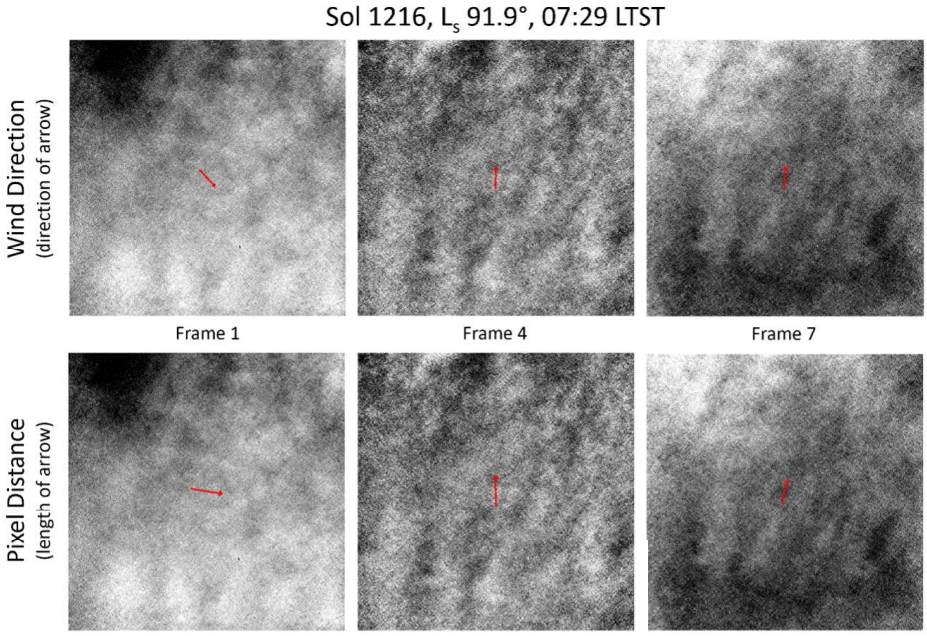

Figure 3.10: Sol 1216 is an example of multiple cloud decks viewed in the movie. They are moving opposite of each other, but the most prominent deck moves from the bottom right to the upper left. The algorithm appears to measure the pixel distance very well with low standard deviation, which could be due to both decks moving at the same rate. For the wind direction, the algorithm gets confused on which deck to follow and flips between each direction. More training is needed for the wind direction output.

3.4 Conclusions

Overall, it appears that the algorithm needs some more testing but offers a great stepping-stone into understanding how computing techniques such as Computer Vision and Machine Learning can be used for Martian aerosol studies. The large dataset from MSL grants us the ability to test how well the algorithm can calculate wind parameters with movies under varying conditions. Movies with strong cloud features were

able to match manual results, but movies with lighting effects, camera artifacts or cloud decks had large errors or did not match manual results. Knowing this enables us to train the algorithm to recognize these features. By testing on a dataset from Mars, we can see if an automated algorithm could be implemented on future spacecraft as a pre-processing step.

4 Learning from Martian Surface Missions to Develop a Low-Cost Optical Meteorological Station

4.1 Overview

Even though more spacecraft have visited Mars than any other planet in our solar system, there are still many gaps in our understanding of the Martian environment due to the high cost associated with space missions and the consequence of fewer undertaken investigations. In particular, 40 have been at least partially successful in their exploration of the planet with less than 20 having visited the surface as landers, rovers or helicopters. These surface missions are especially valuable as they are the only missions capable of categorizing the lower atmosphere associated with the Planetary Boundary Layer (PBL). The PBL is where the surface and atmosphere mix and where any future human exploration would take place. Furthermore, any analysis of the Martian atmosphere will be incomplete without a thorough understanding of the PBL.

While many orbiters have studied the Martian surface from above, there are several limitations which prevent these spacecraft from observing the lower atmosphere. At altitudes below 10 km, occlusion from the terrain becomes an issue. Above this, at altitudes of up to 60 km, certain configurations of instruments and orbiters – such as limb sounders – may struggle to obtain data due to increased opacity (Kleinböhl et al., 2009) especially when dust loading in the atmosphere is high. With orbiters unable to reliably and regularly resolve the near-surface part of the atmosphere, surface spacecraft must be used to investigate surface-atmosphere interactions.

Two Martian surface missions that have proven extremely useful for understanding the lower atmosphere

are the Mars Science Laboratory (MSL, popularly known as the Curiosity rover) and the Phoenix lander. Both spacecraft made use of onboard cameras to capture aerosol activity around the spacecraft and to classify the properties of those aerosols. In addition to atmospheric movies captured with its camera known as the Surface Stereo Imager or SSI, Phoenix jointly used its lidar with the SSI at night to capture light backscattered towards the surface from the lidar laser beam to measure ice-water content in the near-surface atmosphere (Moores et al., 2011). Even though MSL does not have a lidar, engineering cameras were still used to create an umbrella of atmospheric aerosol observations to calculate opacity (Kloos et al., 2016; 2018), winds, (Campbell et al., 2020), ice-crystal shape (Cooper et al., 2019) and altitudes via shadow movement on Aeolis Mons (Campbell et al., 2020).

Even with surface missions, there remain many limitations on our past study of the near-surface atmosphere. For instance, these spacecraft are only able to retrieve local conditions at their widely spaced landing sites. The spacecraft are also limited to how many times an experiment/observation can be successfully repeated due to limited onboard resources. For instance, for the Phoenix combined SSI-lidar experiments, a total of ten attempts over 151 sols yielded four successful detections of water-ice fogs (Moores et al., 2011). Meanwhile on MSL, power, data and complexity limits result in 6-minute atmospheric observations being completed at best 1 or 2 times per week (Campbell et al., 2021). The remaining geographic and temporal informations must be filled in using numerical models. However, models also use Martian data with Haberle and Catling (1996) suggesting that a minimum of 15-20 globally distributed surface meteorological stations are needed to accurately map and model the Martian atmosphere. It is important to not only utilize current mission resources in the best way to maximize observations, but to investigate low-cost options that could achieve higher frequency measurements than the Phoenix and MSL missions were able to accomplish.

The Mars Atmospheric Panoramic and Laser Experiment (MAPLE) could be one such option. This instrument will utilize a panoramic camera and multiple low-powered lasers to study aerosols based on observations successfully conducted from the Phoenix and MSL missions. A housing was created to incorporate the camera and laser system to enable field experiments. Battery packs and a Raspberry Pi will be included in the structure to power both the camera and lasers out in a remote field. To test MAPLE, experiments

were completed in Argentia, NL to determine how well the instrument performs with near-surface aerosols in an accessible field site.

4.1.1 Author Contribution

The goal for this part of the dissertation was to investigate various low-cost methods methods of analyzing local atmospheric conditions based on previous successful Mars missions. Based on my expertise working with surface Mars missions, I was able to expand on new ideas on how to improve current and past observations to develop a low-cost optical meteorological station that was tested in real-life conditions in Newfoundland.

My contribution to this Chapter included picking out various components such as the lasers from ThorLabs and constructing the necessary housing for the camera and lasers. This involved creating windows, putting together ThorLabs parts to hold equipment, and making important changes so the box could include batteries and a Raspberry Pi. These steps were showcased in Figures 4.8 and 4.12.

Once appropriate housing was created for MAPLE, I looked into a good field site location that could be used to test MAPLE with aerosol conditions. Newfoundland was chosen due to the high chance of near-surface aerosols with fog, however, the type of lasers used in our experiment limited the ability to take MAPLE directly onto the field. We decided to reach out to WOOD PLC, a company that handles field site projects in Newfoundland. They were able to give us the proper permits to operate MAPLE in the field in a safe manner. This included access to a secluded field site in Argentia, NL where someone from the company would escort us to the site every day.

To prepare for the field site experiments, I organized everything from travel and hotel arrangements for myself and another grad student. Grace Bischof generously agreed to accompany me on my trip to ensure a proper buddy system. A health and safety guide was created by myself and signed by Grace and the team from WOOD to ensure a proper field safety standard would be adhered to during our experiments. All results from this field site was processed and analyzed by myself. Some legacy code from the Phoenix Mars mission was used to help calculate intensity before being expanded by myself to be applicable for the NL field site and different camera/laser parameters. Any graphs showcasing results were generated by myself.

4.2 Methods

4.2.1 MAPLE Camera and Lasers

To improve upon previous Mars surface missions by incorporating the best ideas from what has come before, MAPLE will be equipped with a panoramic camera and multiple lasers. The panoramic camera provides a view of the entire sky, maximizing our visibility on the atmosphere in each observation while eliminating the need for the instrument to be actively pointed. This reduces operational complexity and power resources. A similar camera called MEDA was employed on the Perseverance Rover which builds on previous measurements of optical depth (solar disc imaging) and cloud optical depth (Maki et al., 2020, Rodriguez-Manfredi et al., 2021). Adding simple Continuous Wave (CW) lasers allows MAPLE to gather additional information on scattering by aerosols in the lower atmosphere, particularly at night. In this way, the lasers build upon the work of the Phoenix Mission (Moores et al., 2011) but at a much-reduced cost to the spacecraft in terms of power.

The camera used in our study is a Basler ace camera (model: acA4024-29uc (BaslerAG, 2023)), equipped with a fisheye lens (FOV = 180°) to maximize the field of view. An example of an image taken with this camera during daytime with observable aerosols is shown in Figure 4.1. Parameters for this camera are shown in Table 4.1. The camera is coloured with a Bayer-filter that has a RGGB layout. The camera includes an IR cut-off, which limits the laser wavelengths that could be included in our analysis to the visible spectrum. The spectral response of the camera is shown in Figure 4.2 and the transmittance showing the IR cutoff is shown in Table 4.2.

Figure 4.1: An example of a frame taken with the Basler camera by previous post-doc Christina Smith. This was taken outside at York University when aerosols (clouds) were in the sky.

Resolution (W x H)	4024 x 3036 pixels
Mono/Colour	Colour
Power requirements	3 W (typical) @ VDC
Size (L x W x H)	29.3 x 29 x 29 mm (without lens mount or connectors)
Weight	$<$ 80 g

Table 4.1: Specifications of the Basler camera acA4024-29uc, taken from BaslerAG (2023)

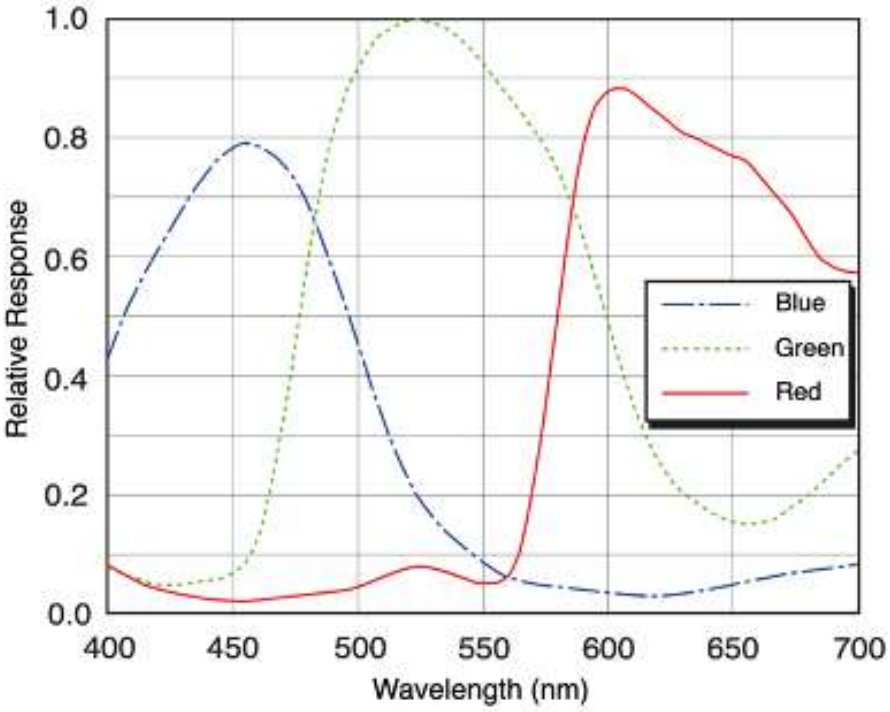

Figure 4.2: Spectral response to Basler camera acA4024-29uc (BaslerAG, 2023). The camera performs best with green colours, which is expected with a Bayer-filter camera that has two green filters versus one for blue and one for red.

Wavelength [nm]	**Transmittance**
450-610	$T_{\text{min}} > 90\%$
450-620	$T_{\text{avg}} > 93\%$
645 $\pm$ 10	$T = 50\%$
700-1070	$T_{\text{max}} < 4\%$
690-1070	$T_{\text{avg}} < 1\%$

Table 4.2: Spectral characteristics of the IR cut off filter for the Basler acA4024-29uc camera (BaslerAG, 2023). The IR cutoff is at 690 nm which means that lasers used by MAPLE cannot be higher than this wavelength.

The fisheye lens used on the Basler camera was tested with a set of known measured grids to determine how equiangular the camera is. We can also determine how many degrees per pixel the camera has for future translation. Figure 4.3 shows multiple grids inside an aquarium that was taken with the MAPLE camera. These grids have a 10 cm separation, which allows us to determine a polar angle conversion value per pixel. Provided by my supervisor, the following figure shows the same image as Figure 4.4 but with an overlaid circle. This circle lines up well with lines from the grid indicating that the camera is equiangular and there is not much distortion. A conversion value of 14 pixels per degree of polar angle was calculated and this value will be used when processing future imagery from field site testing.

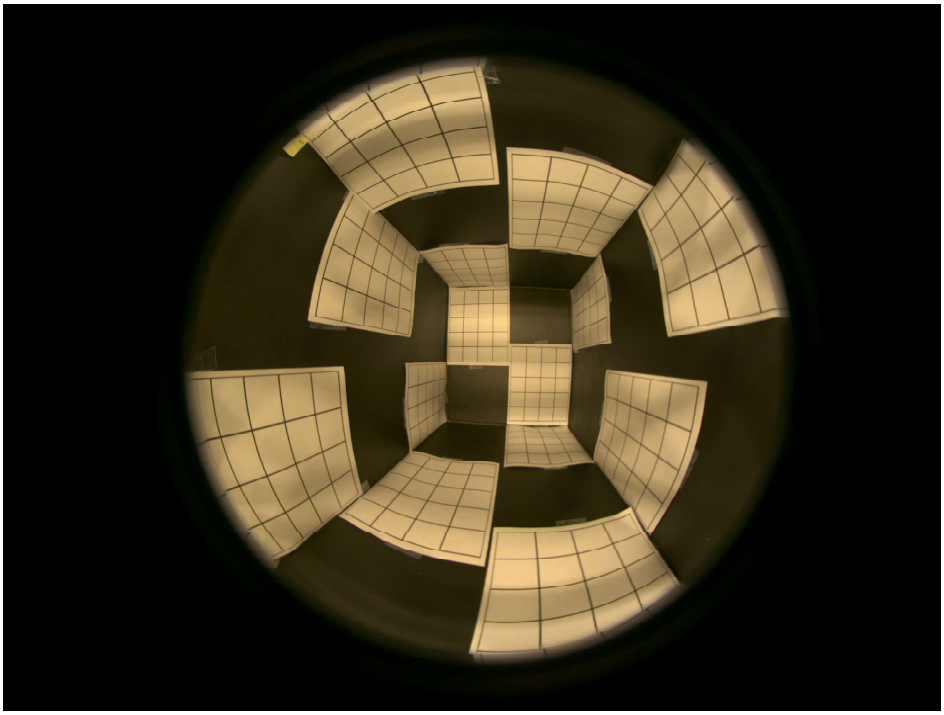

Figure 4.3: An image of an aquarium as taken by the MAPLE camera. Gridded sheets with 10cm x 10cm squares were used to translate to a polar angle conversion of 14 pixels per polar angle.

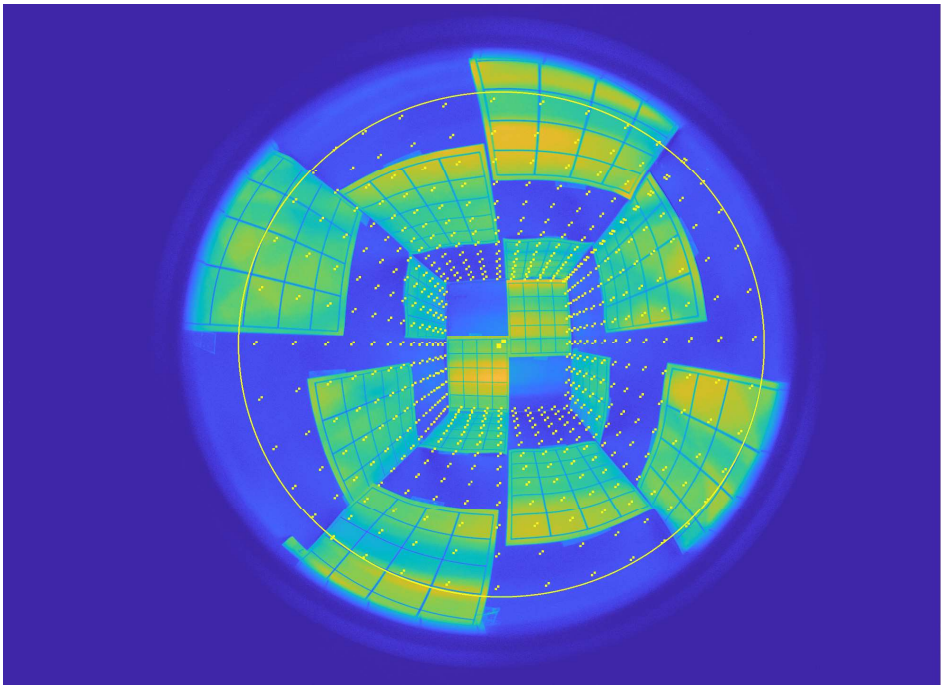

Figure 4.4: The same image as Figure 4.3 but with a perfect circle overlaid to determine any distortion from the camera. Since the circle appears to follow similar lines within the grids, it was determined to be equiangular.

The lasers used in MAPLE are from Thorlabs and are CW (Continuous Wave) and class 3R or class 2. CW lasers were chosen over pulsed lasers due to their constant power output and easier operational handling when on the field. As indicated by their name, CW lasers produce a continuous laser at one power output while pulsed lasers have changing power outputs as it pulses the laser on and off (ThorLabs, 2024). This increases the complexity with pulsed lasers as they rely on calculating the pulse width, peak power and period of pulsing to characterize the laser. However, for CW lasers all that is needed to characterize them is their power output. Another aspect to consider is we want to increase the chance that the laser interacts with nearby aerosols, which is easier with a continuously outputted laser rather than pulsed where we'd have to focus our time to ensure it pulses when it is needed.

Building off the success of the Phoenix Mars mission, we wanted to explore the idea of using a non-lidar laser to determine if it could return similar scattering properties to classify aerosol height and Liquid Water Content (LWC). The Phoenix lidar had a power output of 40 mW and only in the Green wavelength (520 nm) (Whiteway et al., 2008). To keep MAPLE low-cost but maximize science, we went with lower powered lasers but expanded the wavelength range to include more visible wavelengths (red, green and blue). Using multiple coloured lasers allows the study of scattering properties such as shape and size distribution of observed aerosols. Class 2 or 3R lasers were chosen due to their lower power. Class 2 have power ranging from 0-1 mW while class 3R ranges from 1-5 mW. The idea of using a minimum of three lasers in red, green and blue showed that the maximum power output of all three would be $3 \times 5\text{mW} = 15\text{mW}$. This is still significantly lower than the Phoenix lidar set up (40 mW). If these class 2 or 3R lasers are shown useful to calculate aerosol height and LWC, it could be a good option for future low-cost missions.

Laser safety was taken into consideration for MAPLE as higher class lasers can cause damage to the human eye. Based on the American National Standard for Safe Use of Lasers (ANSI Z136.1-2022), lasers are classified into difference classifications based on its potential for biological harm (Kelechava, 2023). This ranges from class 1 (no hazard) to class 4 (severe hazard) thus the lowest hazard classes was ideal for safety. The graphic shown in Figure 4.5 shows that class 2 (0-1 mW) and 3R (1-5 mW) are in the low eye hazard category and thus best for field testing. Even though class 2 and 3R are low hazard, safety guidelines

still indicate to avoid eye exposure to the beam. The Nominal Ocular Hazard Distance (NOHD) can be calculated to determine the distance at which it would be safe for accidental direct eye exposure to the laser beam. Class 2 lasers (0.99 mW) have a NOHD of 7 meters and class 3R (4.99 mW) have a NOHD of 16 meters (Facts, 2023), therefore the lasers could still be hazardous out in the field Since there is still safety considerations for these lasers, appropriate laser eye safety wear from Thorlabs was included for the field testing site.

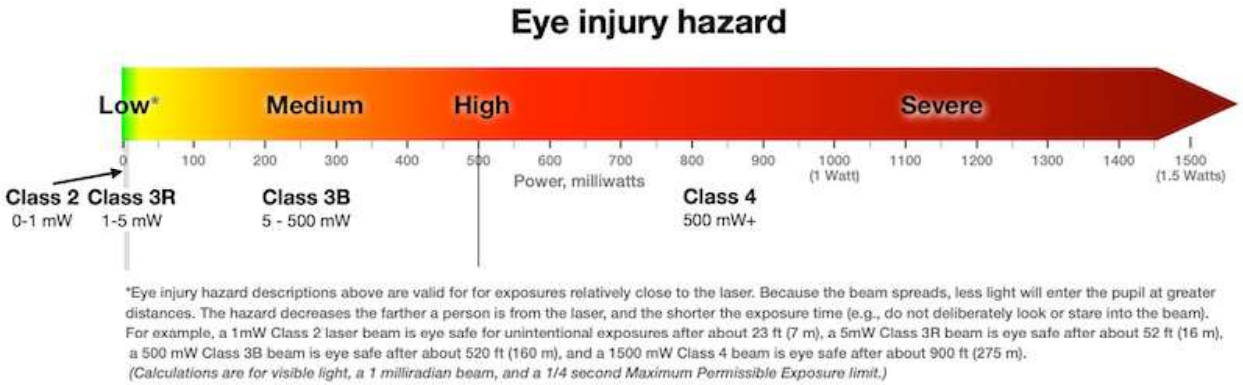

Figure 4.5: Figure from (Facts, 2023) describing the eye injury hazard for the different class lasers. We want MAPLE to be as safe as possible so class 2 and 3R will only be used because of their low hazard for eye injury.

The Thorlabs lasers that were included on MAPLE is shown in Table 4.3. This includes four class 2 lasers and four class 3R lasers all within the visible spectrum. The total power output if all eight lasers were used would be $(4 \times 1\text{mW}) + (4 \times 5\text{mW}) = 24\text{mW}$. Even though we do not plan to use all eight lasers at the same time when on the field, the maximum power output is still signifcantly lower than the Phoenix lidar (40 mW).

Thorlabs Model Number	**Laser Class**	**Power (mW)**	**Centre Wavelength (nm)**
PL205	2	0.89	404.1
PL201	2	0.90	518.8
CPS532-C2	2	0.91	532.1
PL202	2	0.93	637.1
CPS405	3R	4.4	402.9
CPS450	3R	4.3	451.9
CPS520	3R	4.7	514.3
CPS635	3R	4.7	638.0

Table 4.3: Specifications of the Thorlabs visible lasers used with MAPLE for field site testing.

With both the camera and lasers chosen for MAPLE, we wanted to characterize the camera in order to find calibration values at specific wavelengths to convert image Digital Numbers (DN) to spectral radiance. This involved using an integrating sphere and a light source with varying filters that ranged from 400nm to 650nm wavelengths. The integrating sphere is good at making sure light is properly diffused across the whole frame of the camera. The experiments with the integrating sphere and camera were performed by a fellow grad student, Elisa Dong, while the conversion calculation was performed by myself. An example of the green coloured laser (550 nm) is shown in Figure 4.6.

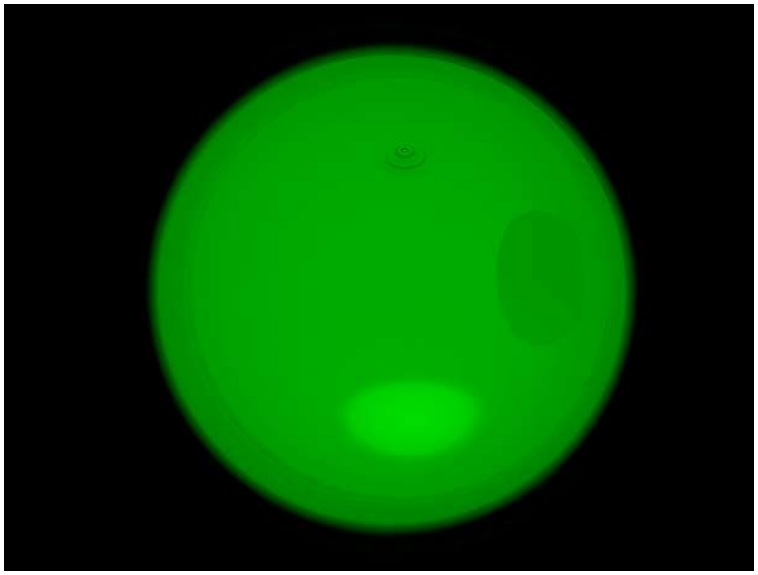

Figure 4.6: An image of the inside of an integrating sphere as seen by the MAPLE camera. The green laser was used to output a consistent spectral radiance to determine how well the camera responds to this wavelength (550 nm).

To find the DN conversion factor, we translated the measured output power from the integrating sphere into $W/m^2/Sr/nm$ using equation 4.1. This value per wavelength is used to then convert DN in MAPLE imagery into spectral radiance (L_λ). The calculated DN conversion factors per wavelength is shown in Figure 4.7 and Table 4.4.

$$\begin{aligned} \text{Conversion Factor}(\lambda) &= \frac{\text{Power Output}()}{\text{size of light meter sensor} \times \pi \times \text{filter width}} \\ &= \frac{\text{Power Output}(\lambda)}{0.0001\text{m}^2 \times \pi \times 10\text{nm}} \end{aligned} \tag{4.1}$$

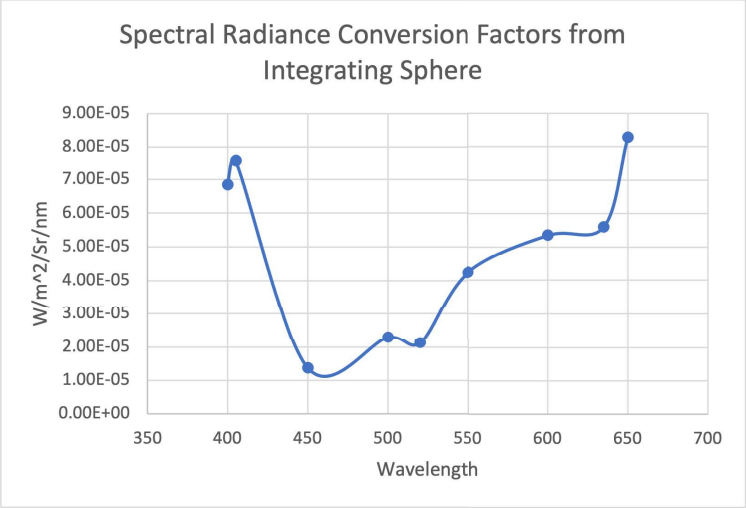

Figure 4.7: The calculated conversion values when converting DN to spectral radiance. A range of wavelengths were included to determine how well the MAPLE camera characterizes visible wavelengths.

Wavelength (nm)	Power (W)	Conversion Factor ($W/m^2/Sr/nm$)
400	2.15E-13	2.15E-04
405	2.37E-13	2.37E-04
450	4.30E-14	4.30E-05
500	7.20E-14	7.20E-05
520	6.70E-14	6.70E-05
550	1.33E-13	1.33E-04
600	1.68E-13	1.68E-04
635	1.76E-13	1.76E-04
650	2.60E-13	2.60E-04

Table 4.4: Table of calculated conversion values based on the power output and equation 4.1.

4.2.2 Constructing Housing for MAPLE

Once the cameras and lasers were chosen, MAPLE needed to be assembled for outdoor field testing. A weatherproof housing for the camera and lasers was designed, built and prepared. A yellow Pelican 1450 case (Figure 4.8), bought from Mountain Equipment Coop, was chosen because of its durability and resistance to water ingress. It was able to securely close and keep any humidity out of the case, which is extremely useful for electronics during foggy conditions. It weighs only 2.9 kg and is able to fully float on water when carrying loads up to 13.6 kg (Pelican, 2023). The interior dimensions are 37.2 x 26 x 15.5 cm (L x W x D) while the exterior dimensions are 41.8 x 33 x 17.3 cm. Noting the interior dimensions, components from Thorlabs were used to merge the camera and multiple lasers into one system for eventual integration into the Pelican 1450 case. A rough schematic for the outside and inside of MAPLE is shown in Figure 4.9.

Figure 4.8: The yellow pelican case chosen for Newfoundland field site testing. Source: Pelican (2023)

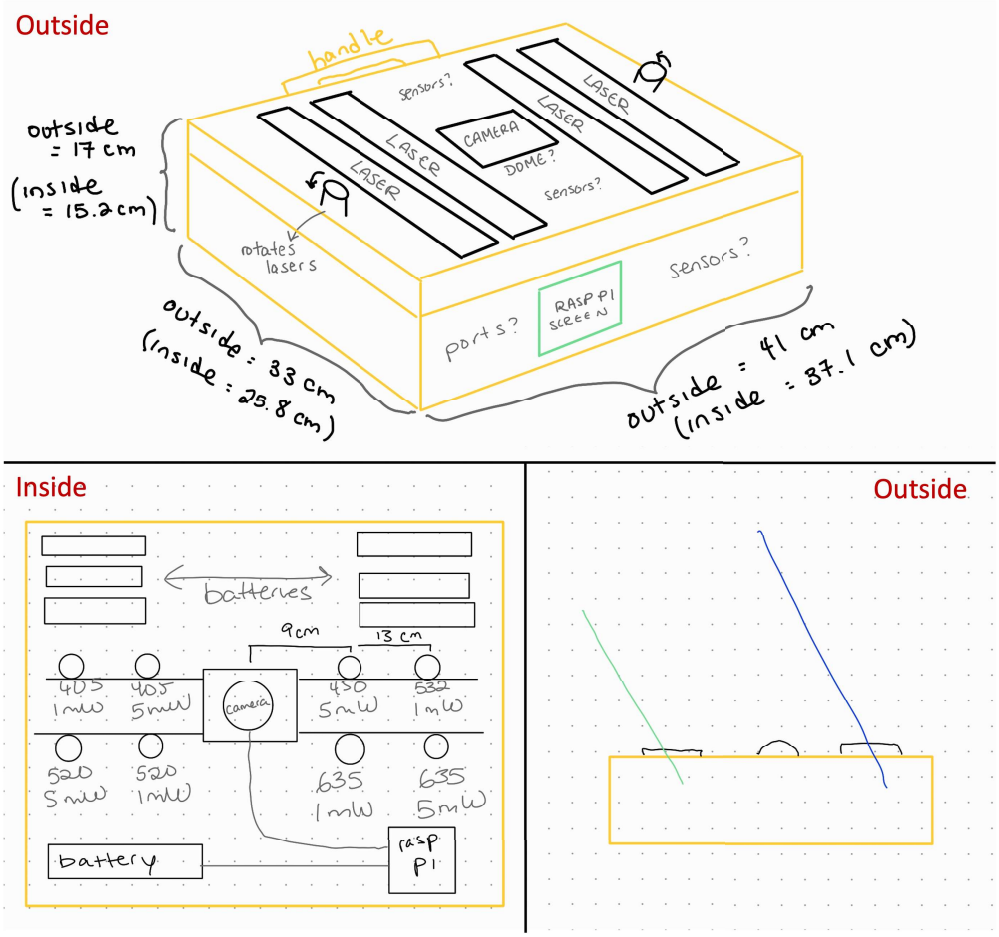

Figure 4.9: Rough schematics created for MAPLE based on the pelican case, camera, lasers, batteries and the raspberry pi used to control the camera. Several aspects were considered, such as putting a screen for the raspberry pi on the outside of the case. However, not everything was included for the Newfoundland field site.

To hold the camera, a self-centering lens mount (part SCL60C/M) was used with a 60 mm cage system. To mount the lasers, a kinematic mount designed by Thorlabs (part MK11F/M) was recommended since the lasers were also from Thorlabs. A 60 mm cage system was constructed and implemented the camera and laser parts as shown in Figure 4.10. To secure the system to the Pelican 1450 case, Thorlabs part CPVM was screwed into the bottom of the case and weather proofed with caulk.

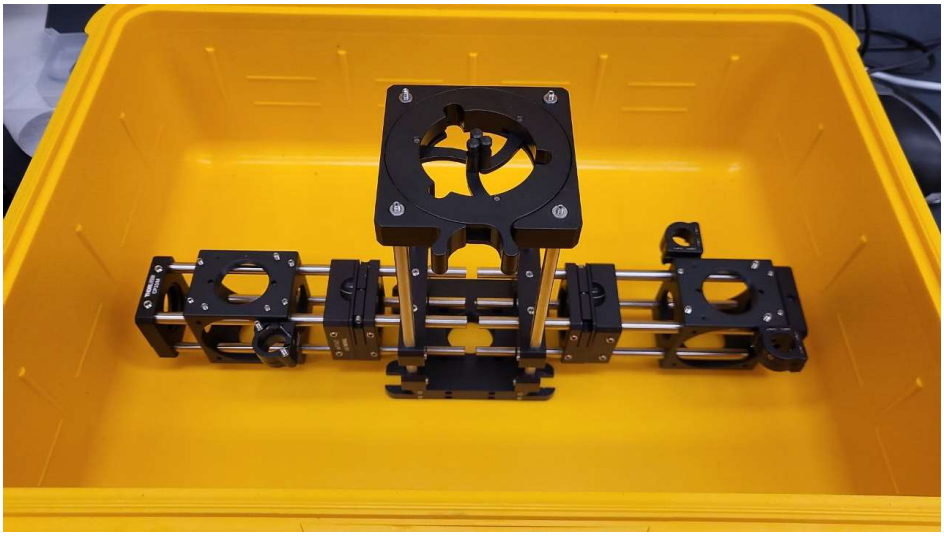

Figure 4.10: The setup for the camera and laser integration with the Pelican case. The camera would be mounted in the middle, with the lasers attached to the perpendicular parts.

Windows were installed for both the cameras and the lasers and were weather-proofed with caulk to ensure that humidity would be low within the case. The panoramic camera needed a special window that could allow the fisheye lens to be above the Pelican case. This would let the camera view as much as the sky without being obstructed by the case. Therefore, three sets of windows were installed in the pelican case; one in the middle for the camera and two on the edge to accommodate the lasers. The laser windows were made of polycarbonate plastic and were sized to fit the pelican case while allowing a wide range of motion within the case. Figures 4.11 and 4.12 exhibit the measurement, construction and installation of these windows.

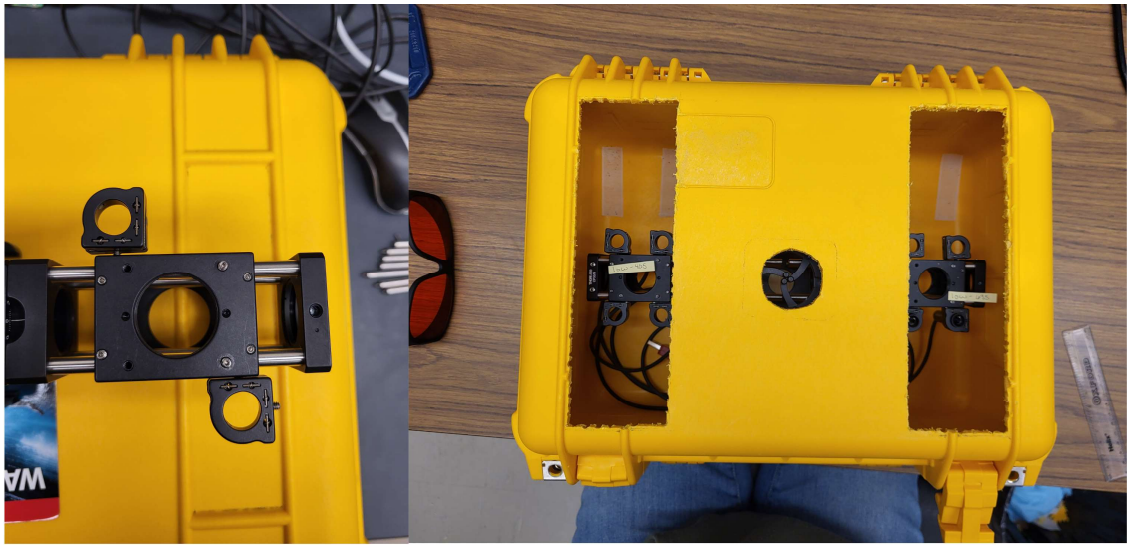

Figure 4.11: *Left:* the size of the Thorlabs part that holds the laser mount was measured against the top of the case.

Right: The three locations for the window were verified with the Thorlabs equipment inside the case to ensure they were the correct size.

Figure 4.12: *Left:* Polycarbonate windows were sized to the correct size of the two rectangular laser window location. The window for the camera was a panoramic camera case. The hole for this window was filed down to ensure a snug fit with the window.

Middle: Caulking was used to glue and seal all three windows from the inside of the case.

Right: Caulking was also applied to the outside of the case to better seal the system since MAPLE will be visiting a high humidity location.

A Raspberry Pi will be used to interface to the camera as a unique feature of the Basler cameras is they offer their software for linux-based computers. Therefore a small screen for the raspberry pi was included, which was created from a waterproof cellphone. A wireless usb keyboard was added to the raspberry pi so that the camera could be controlled remotely. The ultimate goal was to have a screen mounted on the outside of the case to reduce opening MAPLE, but was unable to incorporated for the NL field site. An example of the Basler software being used by the raspberry pi via a waterproof cellphone is shown in Figure 4.13.

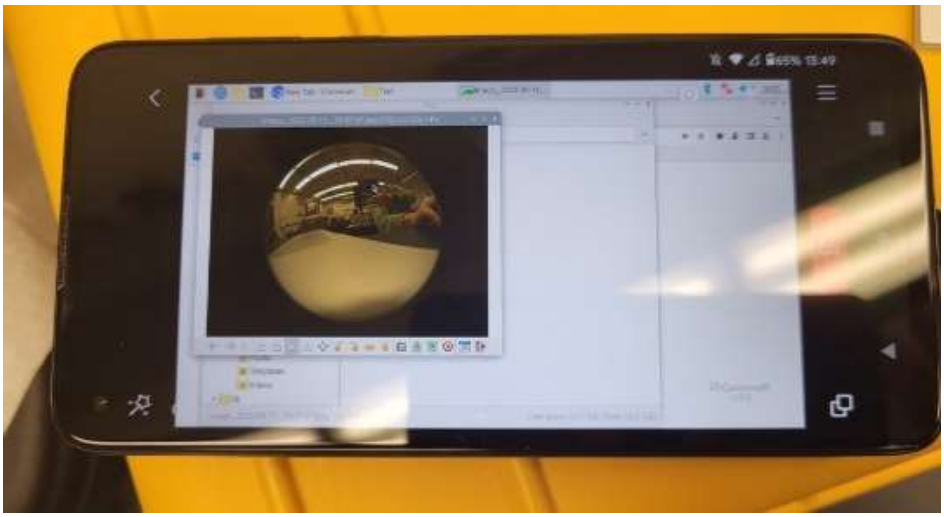

Figure 4.13: A waterproof phone has been set up with a raspberry pi to act as a screen to control the camera. The Basler software has a linux-based option, allowing for camera parameters to be modified if need be. The blackbox with a circular image is an image taken with the Raspberry Pi and Basler camera.

To manage power for all eight lasers as well as continuously run power to a Raspberry Pi to interface with the camera, seven portable battery packs were included in the Pelican case. Thorlabs has batteries packs (10,000 mAh) compatible with their lasers (part: CPS1) so six of those were ordered: one for each class 3R laser (four total) and two for the remaining class 2 lasers. Since the power output for the class 2 lasers is lower (1.0 mW) versus the class 3R lasers (4.5 mW). The last battery pack had a larger capacity (20,000 mAh) as it was used solely to power the raspberry pi which needs a strong continuous output in order to

keep itself and the Basler camera operating. Finally, to ensure that internal humidity was minimized for operation during foggy conditions, dessicant packs were kept inside the case to protect the batteries and electronics.

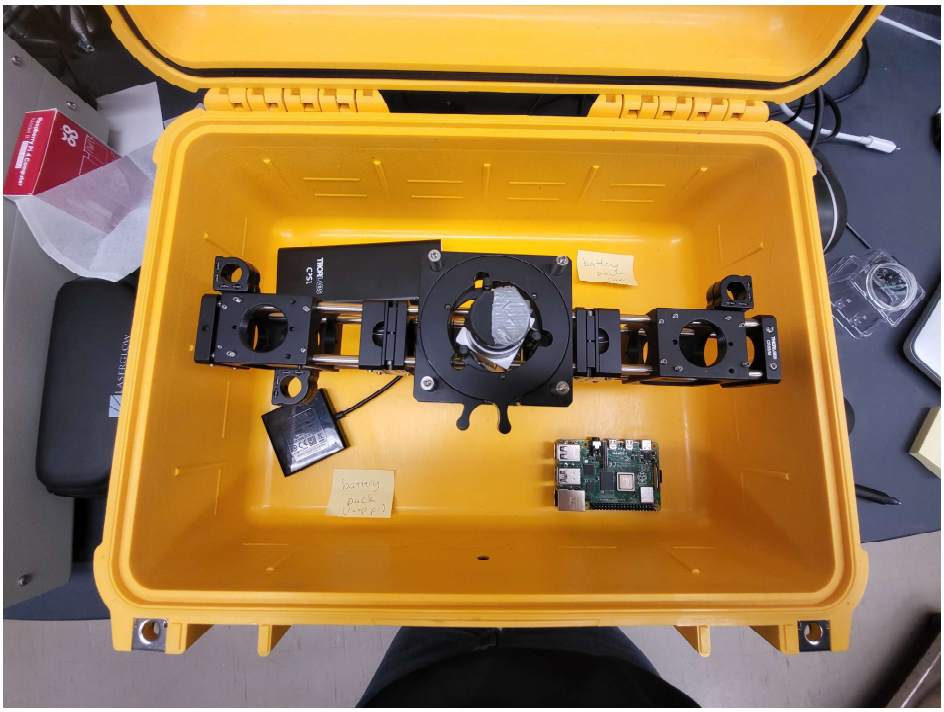

Figure 4.14: A rough top-down view of the MAPLE components, the location of the Raspberry Pi and battery packs. The raspberry pi is in the lower right part of the case, with it's corresponding battery on the lower left part of the case. The batteries for all the lasers will be stacked in both the left and right upper parts of the case.

4.2.3 Argentia, Newfoundland Field Site

To test MAPLE in a real-life setting with reliable near-surface atmospheric aerosols, various locations were explored. We sought a location that was convenient and comfortable to allow us to optimize the instrument before taking it to any challenging field sites. This means finding a site that has a high chance of exhibiting scattering aerosols in a non-remote location. Knowing these conditions, we landed on a location with a high chance of fog: Newfoundland (NL).

Newfoundland is a Canadian province on the East coast close to where two major ocean currents, the Gulf Stream and Labrador Current meet over the broad and shallow grand banks. The Labrador current is a cold current travelling down from the arctic, whereas the Gulf Stream is a warm current travelling up from the Gulf of Mexico. Both are surface currents within the broader circulation of the world's oceans. The meeting of a cold and warm current in shallow waters has the effect of creating frequent fog, in fact the Avalon Peninsula has 206 days of fog each year (Pitt and Pitt., 2015). The best times of the year to view fog is either late spring or late summer. WOOD PLC is a company that has previously worked with environmental monitoring teams in NL and we reached out to them to determine if there were any good field sites in NL to explore. Under their direction, we determined that Argentia, NL would be a suitable spot for MAPLE.

Argentia, NL is a port that is used for both commercial and public use. One unique aspect of the port is that it has an old World-War-II runway that is unused today. The inclusion of this runway made it ideal to perform experiments with the class 3R lasers as there would be no danger to the public and by working directly with the port authority, we were exempted from NavCanada regulations on laser usage. However, because the Argentia port is heavily used outside of the runway, we decided to keep the class 2 lasers in MAPLE just in case there were any issues with the port authority due to variances in daily traffic. The orientation of the runway at Argentia is shown in Figure 4.15, where the black rectangle is the WOOD PLC truck and the blue arrow represents the direction of the lasers down the runway.

Figure 4.15: A map of the Argentia runway courtesy of WOOD PLC. This was used to convey to port authority where the lasers would be located with respect to port traffic. The black rectangle represents our starting point with the WOOD PLC truck and pylons would be used to mark down the runway. To avoid construction on the NE side of the port, the lasers could not point that way, but in the direction of the blue line.

After being approved to use the old Argentia runways for MAPLE, a team of two people travelled to the Argentia, NL area from June 22nd to July 8th, 2022 to attempt to capture data on foggy conditions. Since it is hard to predict when the fog would roll in, we were added to the West White Rose Project for Argentia, courtesy of our WOOD PLC counterpart. This daily forecast for the Argentia, NL area would send daily emails about weather conditions that day with a forecast for the next 2-5 days. Conditions such as precipitation type (e.g. fog, mist), visibility and cloud cover were monitored every 3 hours. The foggiest conditions would typically occur overnight and in the morning, so mornings were designed to be our field site times. When it was predicted that fog would be present the following morning, arrangements were made the previous evening to meet with our WOOD PLC representative to gain access to the field site the following

morning. The WOOD PLC representative was stationed in St John's NL, which was a 1.5-2 hour drive, so plans had to be made ahead of time rather than on the spot. Once we arrived on the field site, we planned to run experiments according to the experimental matrix in Table 4.5. With four lasers (two class 3R and two class 2) on either side of the camera, two lasers will be used at a time. In some cases all the lasers in the same class will be turned on and captured with the camera. This would let only a single image characterize up to four laser's intensity with height, rather than four single images for each laser, which could lower data costs out in the field.

			Laser in use, Wavelength [nm]				
Run Number	Laser Class	Number of Frames	405	450 (3R only)	520	532 (2 only)	635
1	2	10	x		x		
2						x	x
3			x		x	x	x
4	3R	10	x		x		
5				x			x
6			x	x	x		x

Table 4.5: The original experimental matrix for the MAPLE NL field site. The orientation of the lasers in the Pelican case (see Figure 4.9) split the eight lasers into four on either side of the camera. Two class 3R and two class 2 were included on each side so to limit operations, two lasers (one from each side) were used at the same time. All four lasers from each class will be used for a run. An **x** in a laser column indicates that it should be on during that specific run number. A total of 10 frames will be taken for each run number.

Field experiments at the site in Argentia, NL occurred on June 28, June 30 and July 4. These were all completed in the morning when fog was predicted by the West White Rose weather forecast. The goal was to complete a set of ten images of each coloured laser while it is in use in the fog in two orientations, up and sideways. Sideways (Figure 4.16, top) had MAPLE on its side with the lasers pointing down the runway.

Up (Figure 4.16, bottom) has MAPLE on its back with the lasers pointing up into the sky. Therefore, the experimental matrix showed in Table 4.5 will be completed twice, one for each orientation.

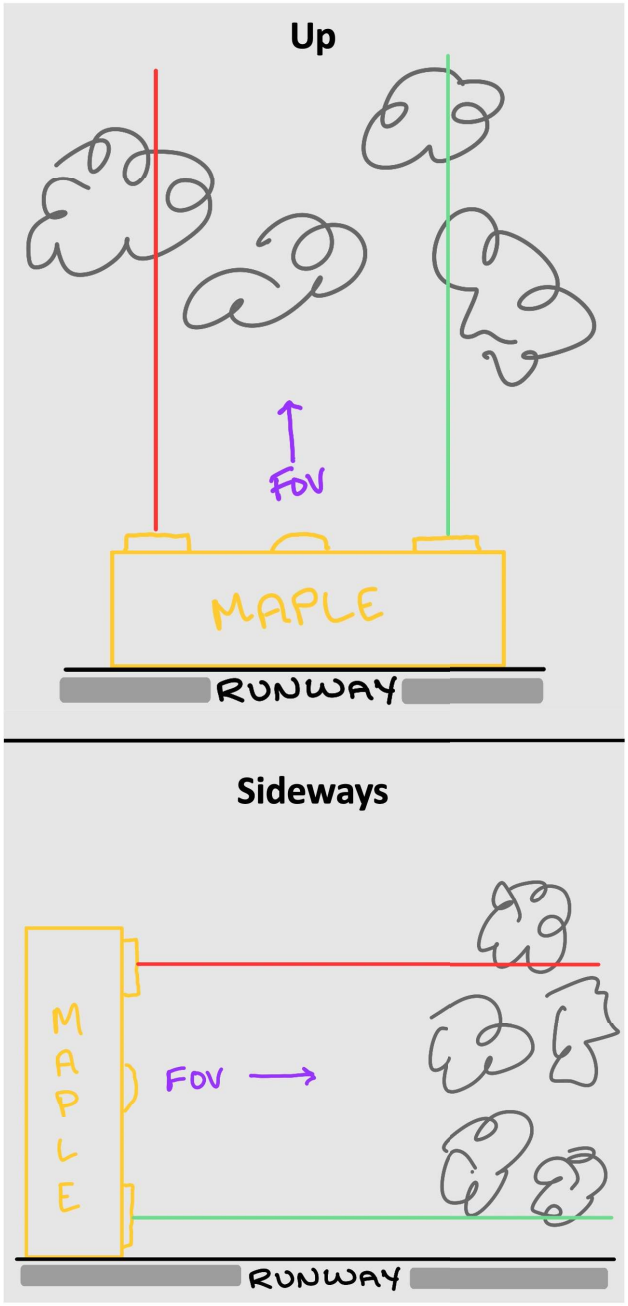

Figure 4.16: The two orientations of MAPLE during field testing in Argentia, NL. *Top:* the up orientation has MAPLE pointing the camera and lasers up into the atmosphere. The goal would be the capture fog decks at heights above the camera, which should be measurable by the change in intensity of the lasers per distance. *Bottom:* the sideways orientation has MAPLE pointing the camera and lasers down the runway, through any fog on the surface. This orientation could capture visibility and how it changes with distance.

4.3 Argentia, NL Field Testing Results and Discussion

4.3.1 Field Testing - June 28, 2022

The first active field day happened on June 28, 2022 in Argentia, NL due to morning fog conditions predicted by the West White Rose Project to occur between 06:30 and 09:30. After meeting with the WOOD PLC representative and discussing health and safety measures, MAPLE was set up in the Up orientation. In order to detect the laser, the exposure time needed to be modified. Values ranged from 50, 200, 500, 1000 and 5000, however, it appeared that even at the lowest time, the camera was unable to see any scattering from the class 3R green laser beam interacting with the fog. An example of the Basler camera with varying exposures in the Argentia field site is shown in Figure 4.17.

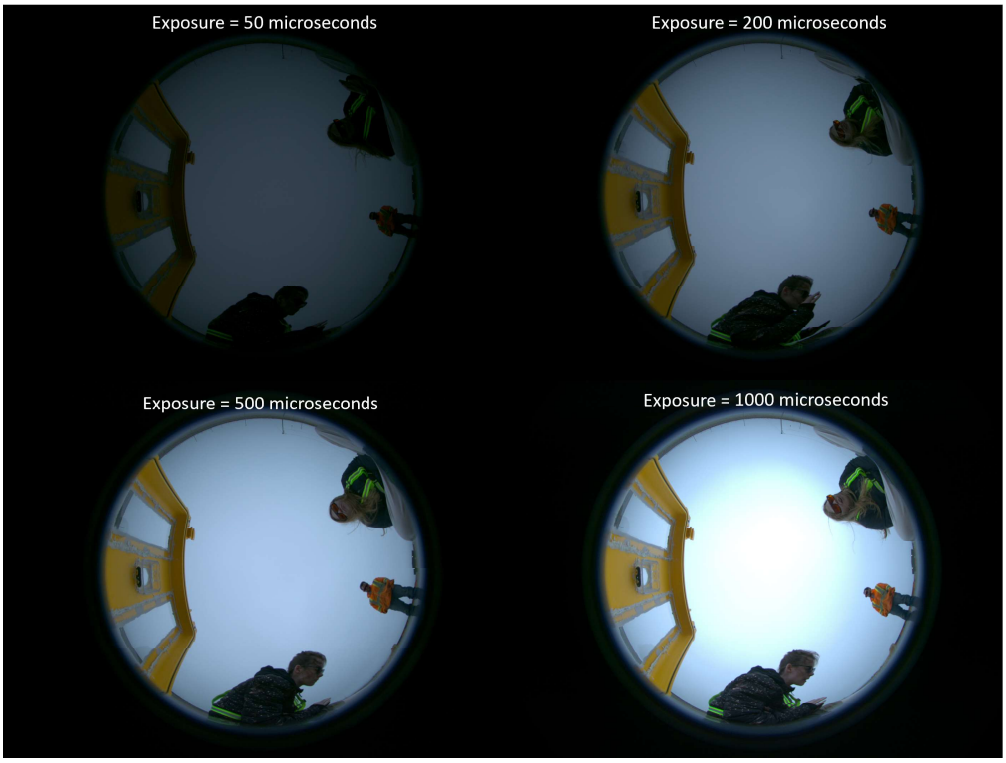

Figure 4.17: Exposure times of 50, 200, 500 and 1000 microseconds with the Basler camera on the first day at Argentia, NL. The class 3R laser is powered on for all four images but is not visible in the raw imagery. This daytime issue was noted for future experiments and the 200 microsecond and 500 microsecond exposure times were used for testing.

With neither the class 2 nor 3R powered lasers viewable in the daytime, a line-of-sight test was created using the Argentia runway and pylons. For this experiment, MAPLE was turned on its side during clear conditions (no aerosols). It was originally placed on the ground but this combination of orientation and location resulted in too much of the ground in the recorded frame. Instead, MAPLE was placed on the back of the WOOD-PLC truck. This lifted MAPLE 1 meter above the ground. This enabled half of the images to view the atmosphere and the other half the runway. One laser was turned on at a time and a white piece of paper was used to follow how far it travelled down the runway before becoming too diffuse. Once it became too diffuse, a pylon was placed on the ground. Once all the pylons had been placed for the lasers,

the distance from MAPLE was measured using equipment provided by WOOD. An image of the pylons were also taken, with a colleague standing at each pylon to identify its location. The distances measured by the line-of-sight experiment is shown in Table 4.6.

Class	Wavelength (nm)	Distance (m)
2 (1 mW)	405	7.92
2	520	32.6
2	532	66.0
2	635	53.3
3R (4.5 mW)	405	76.5
3R	450	75.7
3R	520	96.9
3R	635	80.0

Table 4.6: Line-of-Sight results from the first field test day at the Argentia site. The class 3R lasers travelled further than the class 2. This is because the class 3R lasers have higher power. Therefore it would be better to use the higher powered lasers to ensure the furthest distance from MAPLE can be measured.

The line-of-sight results determined that the class 2 lasers did not travel as far as the class 3R lasers. This is to be expected as the distance a laser travels is dependent on its power. Distance is a key consideration for any laser used to detect back-scattering from atmospheric aerosols therefore, the class 3R lasers would be preferred over the class 2 lasers. However, it is difficult to choose which coloured lasers would be best based on this line-of-sight experiment as the MAPLE camera may see them different in comparison to our eyes. The spectral response shown in Section 4.2.1, Figure 4.2 shows green and red colours are better viewed with the camera, which do travel the furthest. Yet, class 3R blue still performed better in distance than class 2 lasers. Note that because the target in these cases was a white sheet of paper, the absorption characteristics of the aerosols are not considered. For instance, at Mars where aerosols are known to be most optically

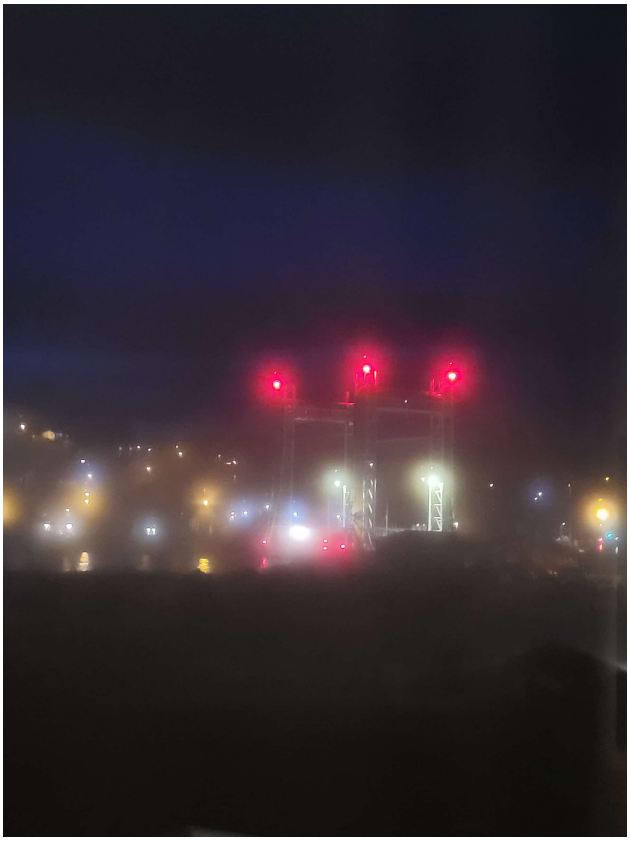

Figure 4.18: Fog on the night of June 29, 2022 as observed from the hotel room. Pictured is the Placentia lift bridge. The fog caused scattering from the lights, showing haziness.

active in the red, the blue laser may not be the best choice unless there is a desire to differentiate between dust and the more spectrally flat water-ice aerosols.

4.3.2 Field Testing - June 29, 2022

Taking into account that neither the class 2 nor class 3R lasers were visible in the day, we explored whether nighttime was a more suitable time of day for our experiments. On June 29, 2022, a thick fog suddenly rolled into the town of Placentia, where we were staying. Figure 4.18 shows an image of the Placentia Lift Bridge on June 29, 2022 at 20:55. The fog was so thick that the lights from the bridge and nearby town Jerseyside were hazy (Figure 4.18).

Images were taken in only the Up configuration to minimize horizontal laser exposure. Unfortunately, in an act of haste, the pelican case was left open while imagery was being taken. This was noted to avoid in the next night-time MAPLE experiments. The lasers used in this experiment are shown in Table 4.7 as an experimental matrix.

			Laser in use, Wavelength [nm]				
Run Number	Laser Class	# of Frames	405	450 (3R only)	520	532 (2 only)	635
1	3R	10			x		
2				x			
3							x

Table 4.7: Experimental matrix for the impromptu nighttime experiments on June 29, 2022. Similar to Table 4.5, lasers with **x** indicate they were on for that particular run. The class 3R lasers were only used.

Figures 4.20 to 4.22 showcase the images taken with MAPLE with the class 3R red, class 3R green and class 3R blue laser. These images were analyzed further with a Matlab code that determines the spectral radiance profile of the laser and graphs it with respect to distance from the camera. The fisheye lens of the camera means that spherical coordinates must be translated to an x,y,z coordinate in order to pull out the laser's coordinates in the frame. To ensure that the code was correctly pulling out the laser within the image, a simulated laser was placed over the image. If the simulated laser did not overlay over the laser then the starting polar and azimuthal points were adjusted until the simulated laser perfectly mimicked the MAPLE lasers. The geometry of the simulated laser in spherical coordinates, after converted to radians, is shown in Equations 4.2-4.4. These spherical coordinate equations (4.2-4.4) are then used in Equation to in order to convert from spherical to azimuthal coordinates. Lastly, these azimuthal coordinates are placed back onto the image with Equations 4.8-4.9 to determine if it properly overlays with the observed laser based on also knowing that there is 14 pixels per polar angle (as mentioned in Section 4.2.1) for the Basler camera. An example of the simulated laser overlaid onto a MAPLE image from June 29, 2022 is shown in Figure 4.19.

$$Beam_x = Beam_{Initial} \times \cos(Beam_{Azimuthal}) \times \sin(Beam_{Polar}) \tag{4.2}$$

$$Beam_y = Beam_{Initial} \times \sin(Beam_{Azimuthal}) \times \sin(Beam_{Polar}) \tag{4.3}$$

$$Beam_z = Beam_{Initial} \times \cos(Beam_{Polar}) \tag{4.4}$$

$$cameraDist = \sqrt{(Beam_x)^2 + (Beam_y)^2 + (Beam_z)^2} \tag{4.5}$$

$$cameraTheta = \arctan(Beam_y, Beam_x) \tag{4.6}$$

$$cameraPhi = \arccos \frac{Beam_z}{cameraDist}) \tag{4.7}$$

$$Simulated_x = 14 \times cameraPhi \times \cos\left(cameraTheta\right) \tag{4.8}$$

$$Simulated_y = 14 \times cameraPhi \times \sin\left(cameraTheta\right) \tag{4.9}$$

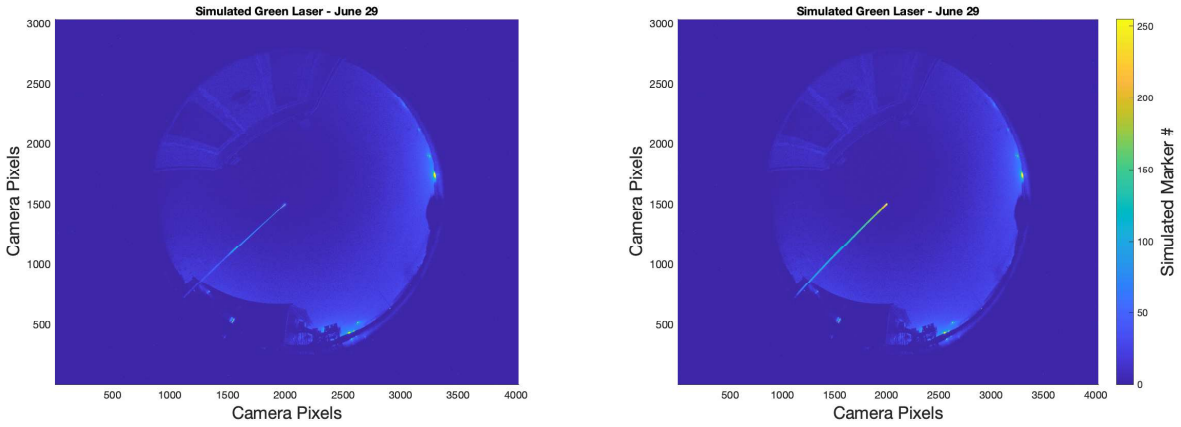

Figure 4.19: Image showing the green laser taken by the MAPLE camera on June 29, 2022. Left shows the actual laser pointing up into the atmosphere while Right has the simulated laser overlaid onto the actual laser.

Once the laser has been simulated and overlaid to the real-life laser (Figure 4.19), our code converts the change in brightness along the laser to spectral radiance. Using the calibration method in lab (Section

4.2.1), conversion values for the corresponding laser wavelength (R, G, B) were multiplied by all intensity (brightness) values. These spectral radiances are then plotted to determine peaks of high spectral radiance at heights above the camera. These peaks would correspond to fog decks above the camera as the water aerosols would cause scattering within the laser, increasing the intensity and spectral radiance. Figures for June 29th fog imagery are shown in Figures 4.20-4.22.

Both the green (Figure 4.21) and blue laser (Figure 4.22) found fog decks at 1 meter and 40 meters above the camera. This appeared consistent with the low visibility around the field site. The red laser (Figure 4.20) appeared to struggle with distances further away from the camera as it was only able to distinguish a fog deck very close to the camera ($<$ 1 meters). However, upon further inspection, the edges of the images have higher intensity because of other light sources within the town of Placentia, affecting the normalized intensity. This did not affect the green and blue lasers, but the red laser unfortunately was affected and does not show accurate results.

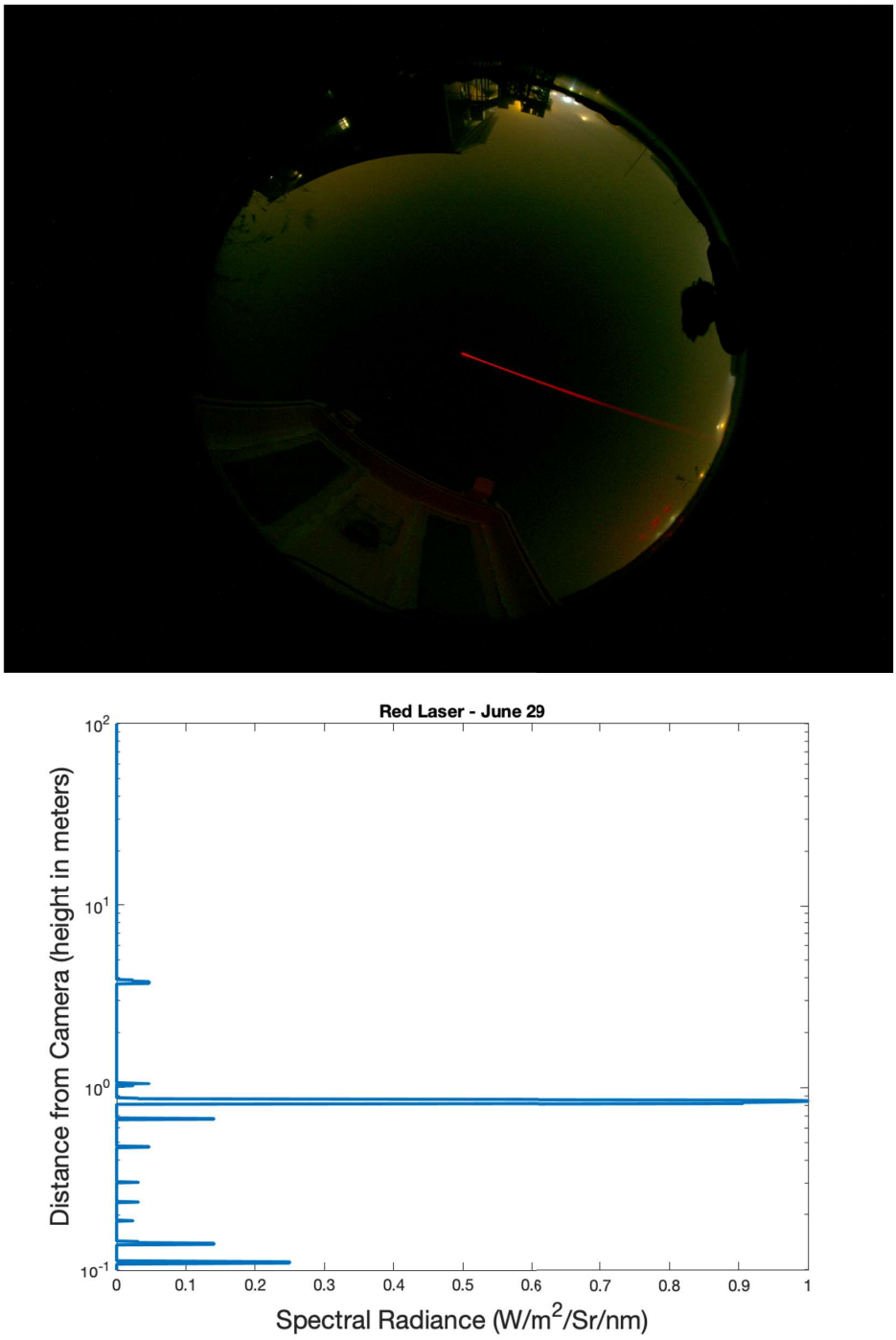

Figure 4.20: The class 3R red laser in use on June 29, 2022. The normalized intensity (bottom) is modelled as a function of distance from the camera based on the laser path in the top image. Light pollution from nearby light sources appears to affect distances near the camera and may need to be investigated further.

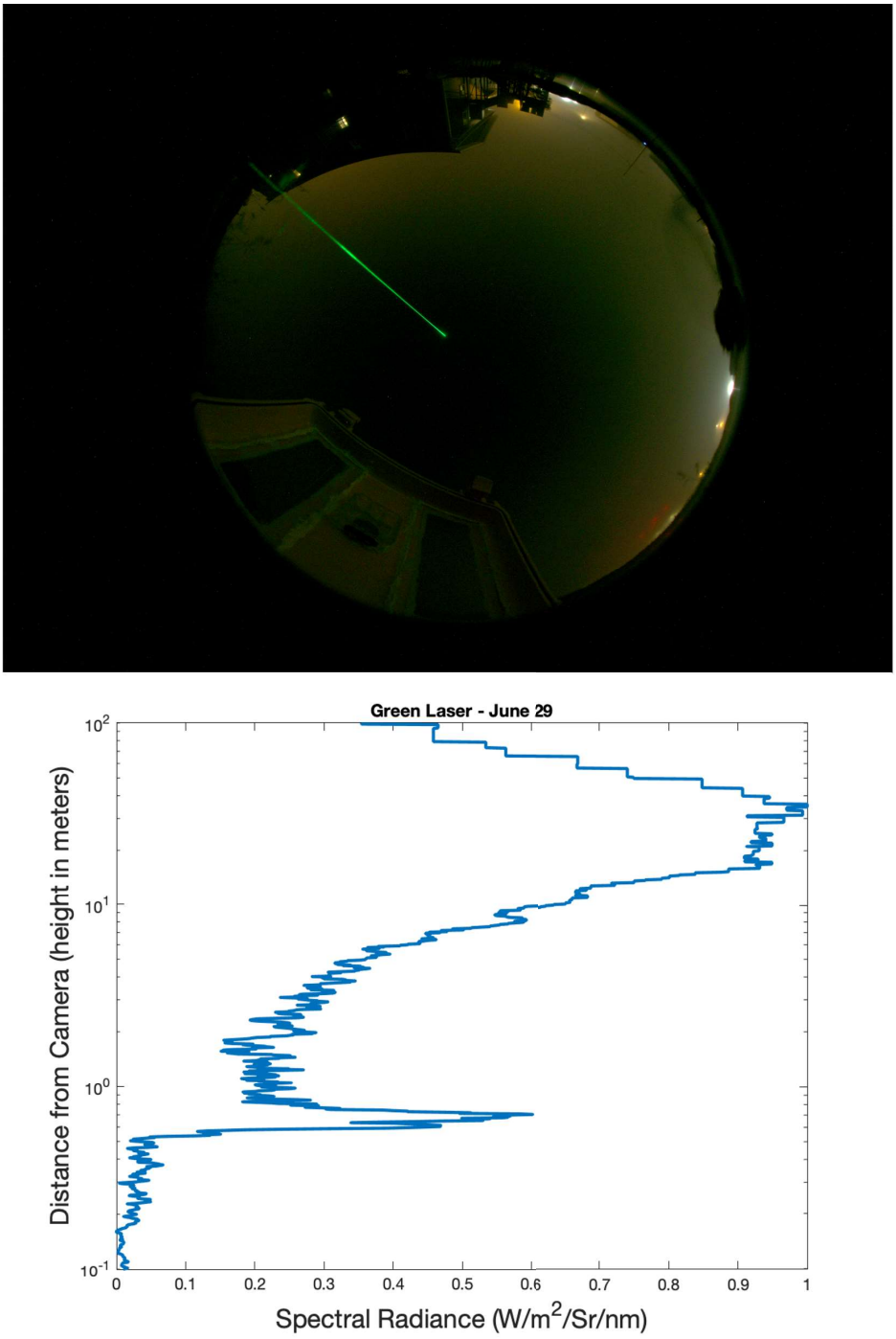

Figure 4.21: Similar to 4.20 but for the class 3R green laser. Light pollution does not affect the green laser as much. This could be due to minimal light pollution around the horizon near the start of the green laser. Fog decks were measured at 1 meter and 40 meter above the surface. The thick fog layer confirms the near-surface aerosol measured by the class 3R green laser.

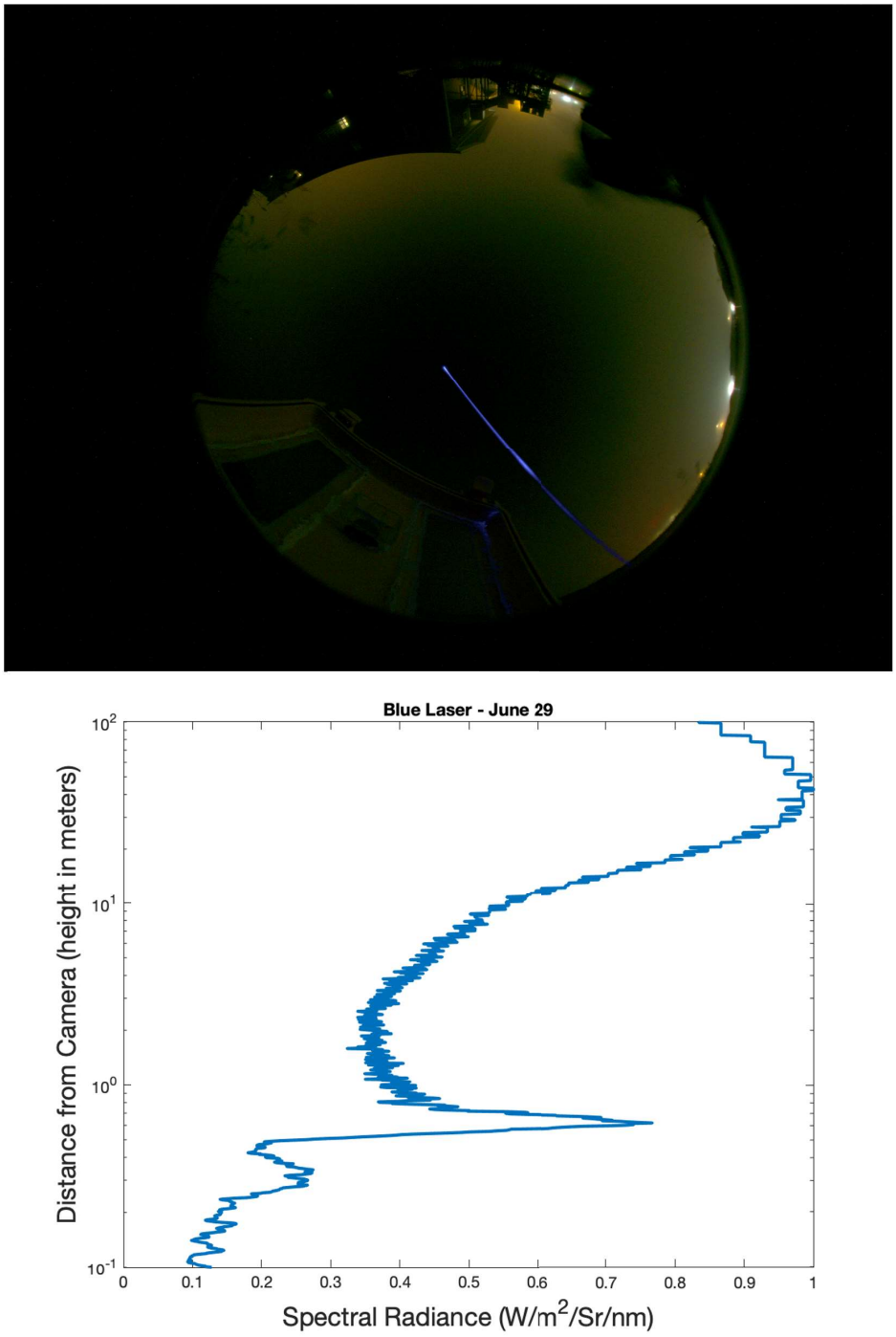

Figure 4.22: Similar to 4.20, but for the class 3R blue laser. Light pollution slight affects results but not to the extent as the red laser in Figure 4.22. The blue laser measured similar cloud decks as the green laser (Figure 4.21).

The spectral radiance graphs produced for this field site can be used to estimate the Liquid Water Content (LWC) at each vertical point above the camera. The LWC equation is taken from Equation 1 in Moores et al. (2011) and is shown here in Equation 4.10. All of the parameters in this equation are shown in Table 4.8 with known values noted if applicable. We must consider that certain parameters have changed values from the Moores et al. (2011) results as we are observing water fog here on Earth rather than water-ice clouds on Mars. For example, the density (ρ) would be 1000 $\frac{kg}{m^3}$. The size of particles (a) has been found to range between 1 and 30 micron (Meyer et al., 1980) so the middle point (15 micron) was used. To calculate the transmittance, Beer's-Lambert law was used which uses optical depth (OD). This is shown in Equation 4.11 where the OD is shown in Equation 4.12. Putting all these parameters together into Equation 4.10 lets us understand the LWC at various heights above MAPLE. We also graphed the transmittance and OD in a similar manner. These are shown in Figures 4.23-4.25 for each laser.

$$LWC = \sum_{z} L_{\lambda}(z) \frac{4\pi}{\phi} \frac{z^2 \Omega_{pixel} \Delta\lambda}{P_{laser} cos^2(\theta)} \frac{1}{T(z)^2} \frac{2a\rho}{3\Delta z} \tag{4.10}$$

$$T(z) = e^{-OD(z)} \tag{4.11}$$

$$OD(z) = (\Delta z) * ((L_{\lambda}(z))); \tag{4.12}$$

LWC Parameter	**Meaning**	**Value**
$L_\lambda(z)$	Spectral Radiance	Found in imagery from laser and converted to via DN conversion values from Table 4.4
ϕ	Phase Function	Assuming isotropy = 1/15
z	Height level above camera	Ranges from 10^{-1} to 10^2
Ω_{pixel}	Solid Angle	Calculated by finding the number of horizontal pixels and dividing by the camera FOV (180°) = 10^{-6}
$\Delta\lambda$	Bandwidth from spectral radiance conversion	10 nm
P_{laser}	Power of the laser in use	red laser = 0.00453W green laser = 0.001794W blue laser = 0.00398W
θ	Angle of the laser from the zenith point per distance from the camera	Calculated for each point above the camera based on horizontal distance between laser and camera
$T(z)$	Transmittance	Calculated using Optical Depth (OD) for each point above the camera. $T(z) = e^{-OD(z)}$
a	Radius of aerosol in question	15 micron
ρ	Density of aerosol (water)	1000 kg/m^3
Δz	Step size in distance above camera	Calculated within code for each distant point above the camera

Table 4.8: Table showing the parameters for the LWC equation (Eqn 4.10)

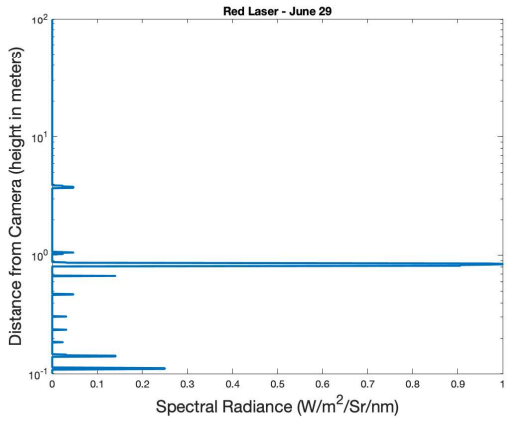

(a) Spectral Radiance

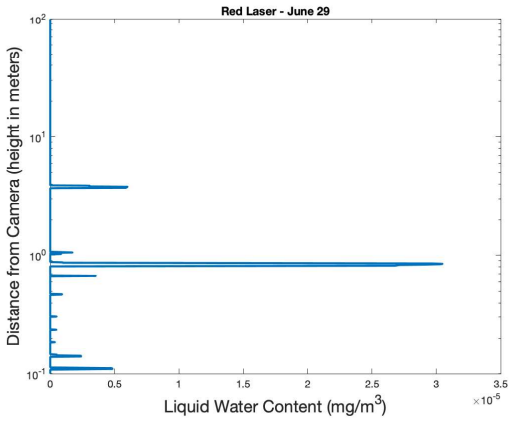

(b) Liquid Water Content

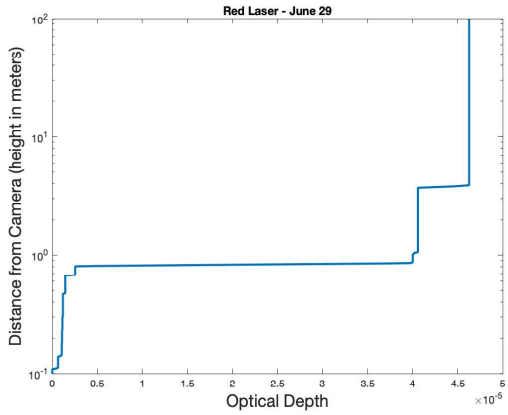

(c) Optical Depth

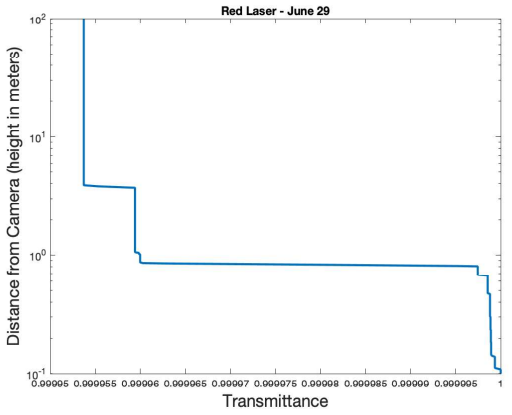

(d) Transmittance

Figure 4.23: Red laser LWC analysis with Spectral Radiance (a), Optical Depth (c), and Transmittance (d).

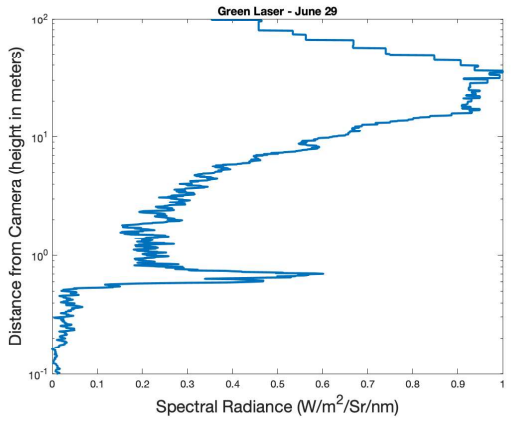

(a) Spectral Radiance

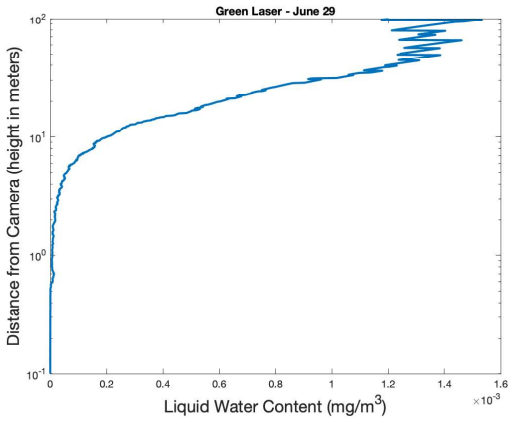

(b) Liquid Water Content

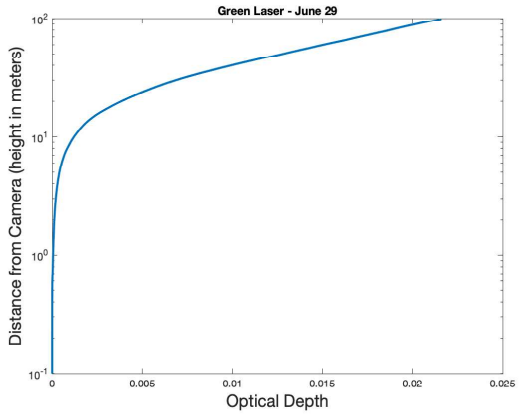

(c) Optical Depth

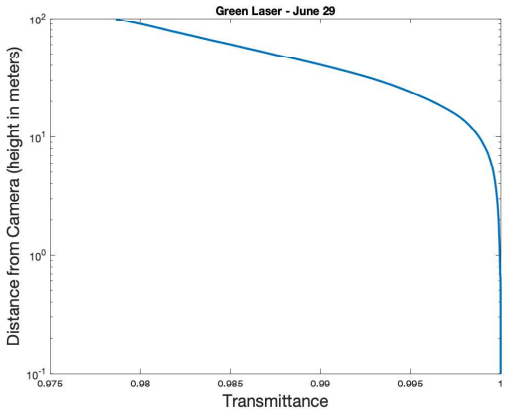

(d) Transmittance

Figure 4.24: Green laser LWC analysis with Spectral Radiance (a), Optical Depth (c), and Transmittance (d).

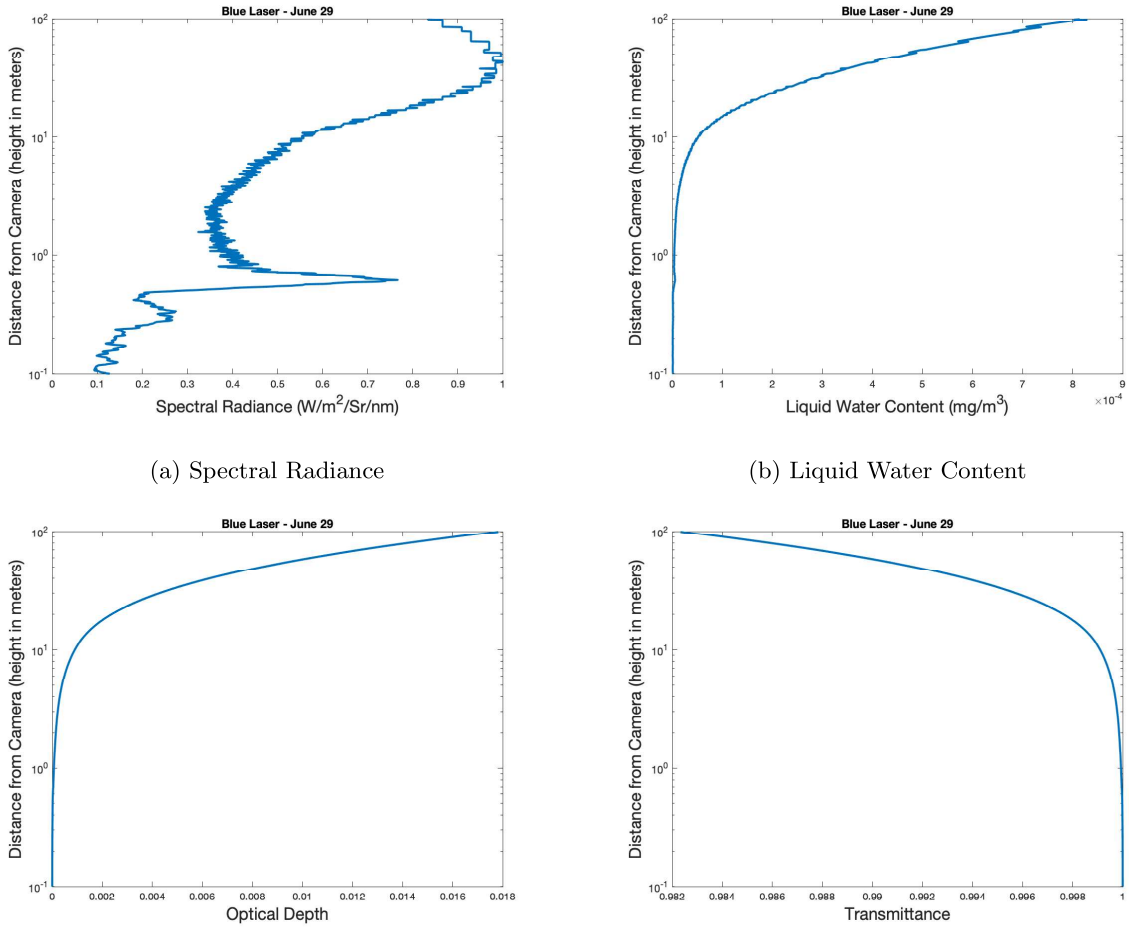

(a) Spectral Radiance

(b) Liquid Water Content

(c) Optical Depth

(d) Transmittance

Figure 4.25: Blue laser LWC analysis with Spectral Radiance (a), Optical Depth (c), and Transmittance (d).

When applying the LWC equation (4.10) we can see that the red laser produced incoherent results while both the green and blue lasers showed higher LWC at the top of the laser, furthest from the camera. Unfortunately the cloud deck at ∼1 m does not seem to be represented well in either laser LWC analysis. The transmittance and optical depth graphs were also included to determine their behaviour. The green laser finds a higher optical depth at higher altitudes because MAPLE observes a larger opacity the more fog it observes through. The peak for the green laser was at 0.022. The blue laser shows similar behaviour to green but peaks at 0.018, a lower optical depth than green. Both measurements indicate that the fog is suboptical. Unfortunately result from the red laser were not used due to showing unreliable results (Figure 4.23).

The difference between the day and night imagery shows a stark contrast on conditions to observe the lasers. The class 3R lasers could not be resolved during the day due to the significant higher background brightness caused by sunlight scattering within the fog. However, at night-time, backscatter from the same lasers could be observed right away with the camera and then analyzed to deduce vertical information about fog decks. Therefore, lasers at classes higher than 3R with increased power should be used during the day to acquire measurements.

4.3.3 Field Testing - June 30, 2022

The thick fog observed on the night of June 29, 2022 continued into the morning of June 30, 2022 so arrangements were made to visit the Argentia field site. Learning from the first field experiment on June 28, 2022, the exposure time was lowered to minimize overexposure from the sun. 200 microseconds and 500 microseconds were the exposure times used moving forward. Since the high-power Green laser was the best laser seen by the camera, only this laser was used during the June 30, 2022 experiments. The experimental matrix for this series of images is shown in Table 4.9.

Table 4.9: Experimental matrix used on June 30, 2022 for daytime experiments at the Argentia, NL fieldsite. To maximize the chance of seeing the lasers in the day, only the class 3R green and red laser were used as they had a higher spectral response for the Basler camera (Figure 4.2). Background images were also taken for image subtraction to attempt to pull out any visible laser in the imagery. Both 200 and 500 microsecond exposure times were used.

					Laser in use, Wavelength [nm]	
Run Number	Laser Class	# of Frames	Orientation	Exposure time	520	635
1	3R	10	Up	200	x	
2				200	None - Background	
3			Side	200	x	
4				500	x	
5				200		x
6				500		x
7				200	None - Background	
8				500	None - Background	

Unfortunately, the background illumination in images acquired on this day in sunlit conditions was still too bright to observe any laser backscatter in the images. Even though fog was in the vicinity, the laser beam was unable to be resolved in the imagery. Background images that were acquired on this day were used to help look for laser backscatter within the images. By subtracting the background with any image that should have a visible laser beam backscattering off fog particles, we had hoped this beam could be distinguished. Background images in 200 and 500 microsecond exposure times are shown in Figure 4.26. For each run that was not a background set, a raw and background-subtracted image are shown in Figures 4.27-4.31. Even after performing this image reduction technique, no lasers were discernable in the imagery during the day. The lasers not being powerful enough could be a big factor, however, there also may not be

enough aerosols in the vicinity to scatter off the class 3R laser.

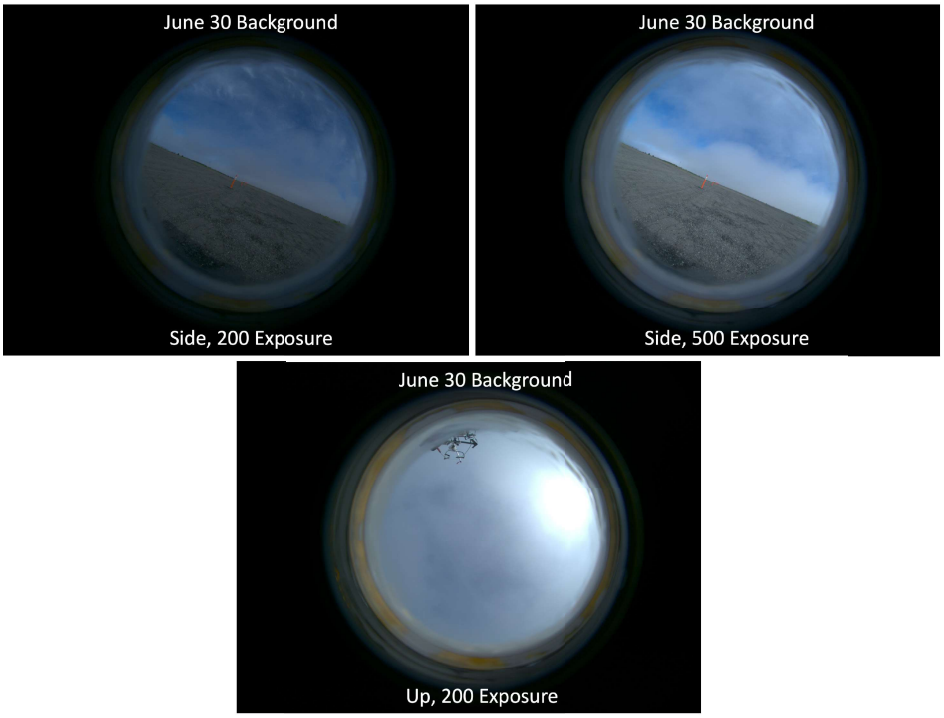

Figure 4.26: Background images taken on June 30, 2022 at the Argentia, NL site. These would be Run 2 (bottom), 7 (top,left), and 8 (top,bottom) in Experimental matrix 4.9.

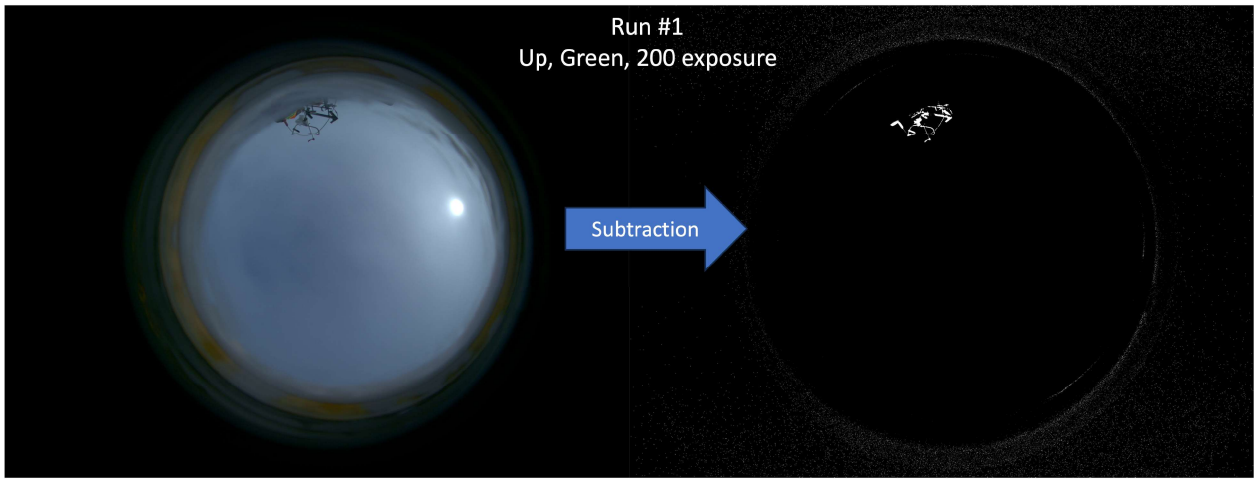

Figure 4.27: Raw (Left) and background-subtracted (Right) images for the runs laid out in Matrix 4.9. No laser beam was detected in this image which could be due to limited near-fog at this time.

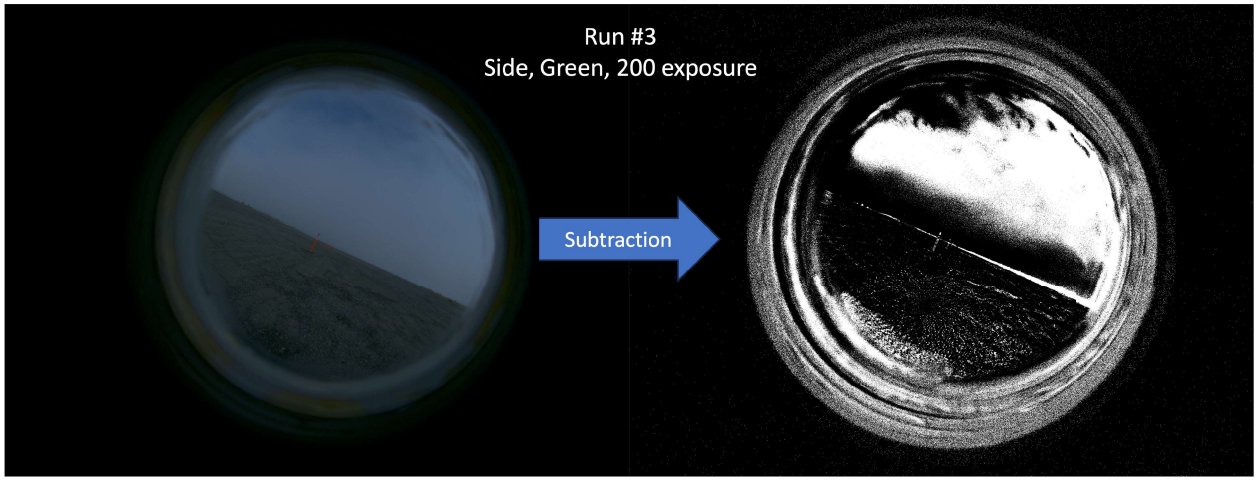

Figure 4.28: Same as 4.27, but for side orientation. No laser beam was detected.

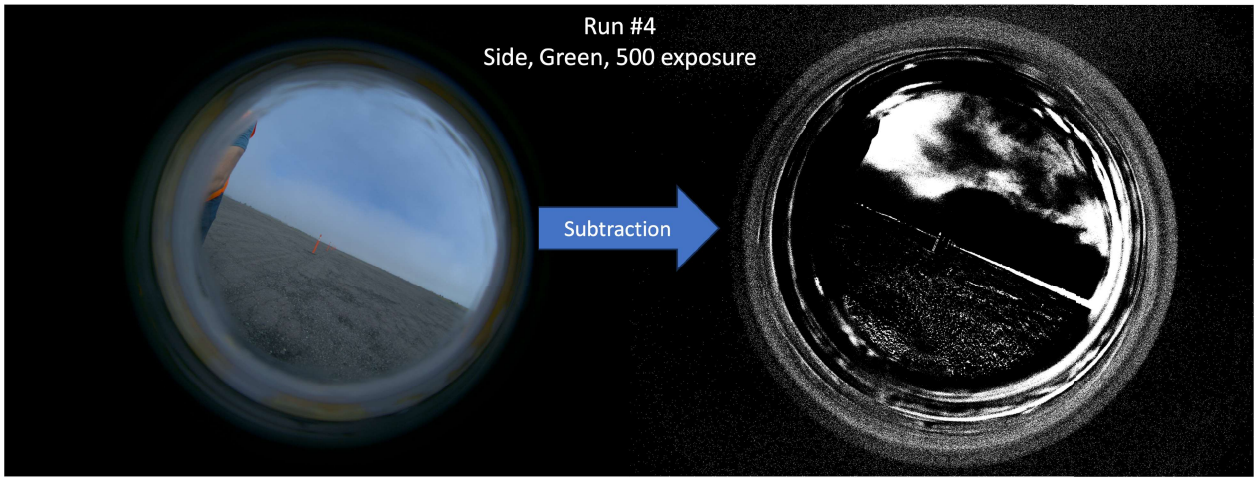

Figure 4.29: Same as 4.28, but with higher exposure (500 microseconds). Results continued to show null results on observing the laser within the subctracted image.

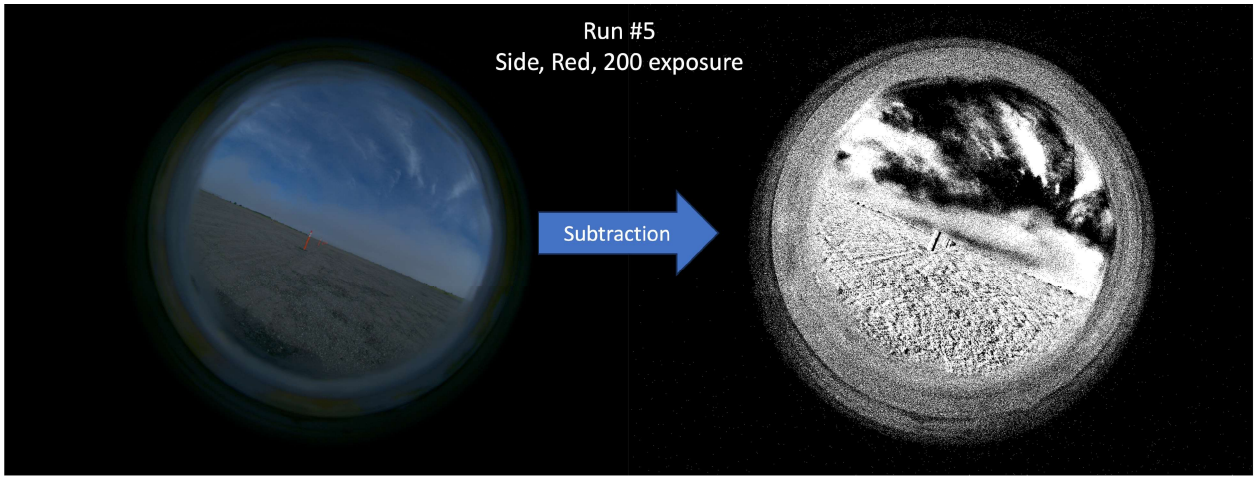

Figure 4.30: Same as 4.28, but with the class 3R red laser. Similar to the green laser, the red laser was unable to be detected with background subtraction.

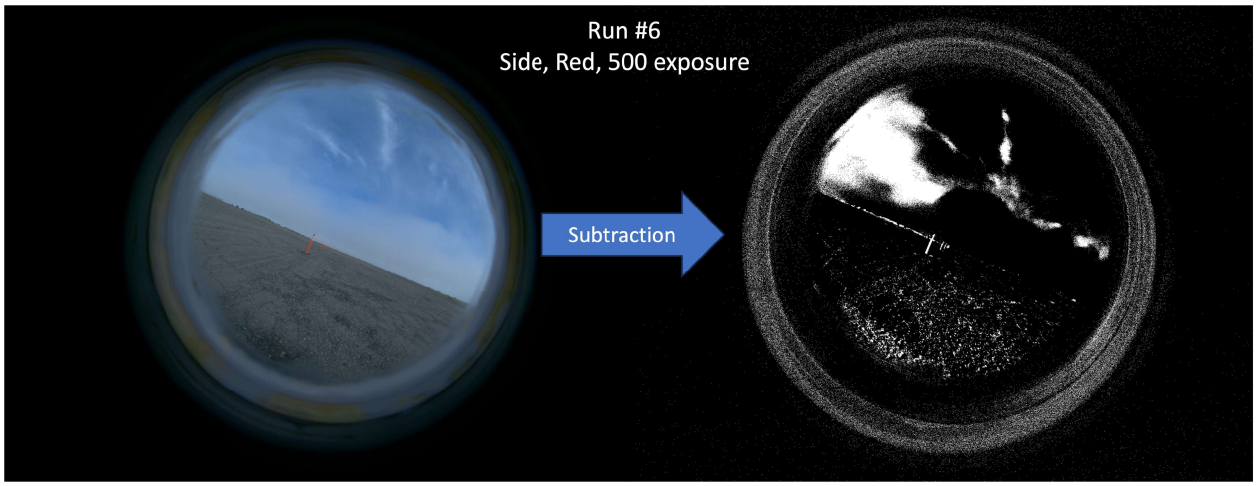

Figure 4.31: Same as 4.30, with a higher exposure, which still does not show any laser in imagery.

By 10:00, the majority of the fog had dissipated from the runway. However, fog was still quite heavy over water as shown in Figure 4.32. These conditions were comparable to the first field day (June 28, 2022). The bay had cooler temperatures in comparison to the tarmac and supported the formation of fog longer into the morning. This is demonstrated in Figure 4.33 that shows the field of view (FOV) of Figure 4.32 with the peaks actually across the bay of Placentia. Unfortunately, after sunrise the fog would dissipate within

2-3 hours and thus experiments at the Argentia site would wrap up around 10:00. Yet, fog would still be viewable over the water. Fog would occasionally be present over the course of the day but these conditions were observed so infrequently or unexpectedly that it was difficult to gain access to the site sufficiently rapidly to respond when we needed it. In some cases, the fog would come and go within ten minutes, which would not be enough time to get MAPLE set up for experiments. Therefore, exploring better locations that could support long-term fog experiments would be beneficial for future expeditions with MAPLE.

Figure 4.32: An image captured at the end of the field test where fog can be seen further in the distance with peaks observed above. In comparison with Figure 4.33, the fog observed is over the Placentia bay. Thus, it could be of interest to investigate fog measurements over bodies of water as they hold onto fog longer throughout the day.

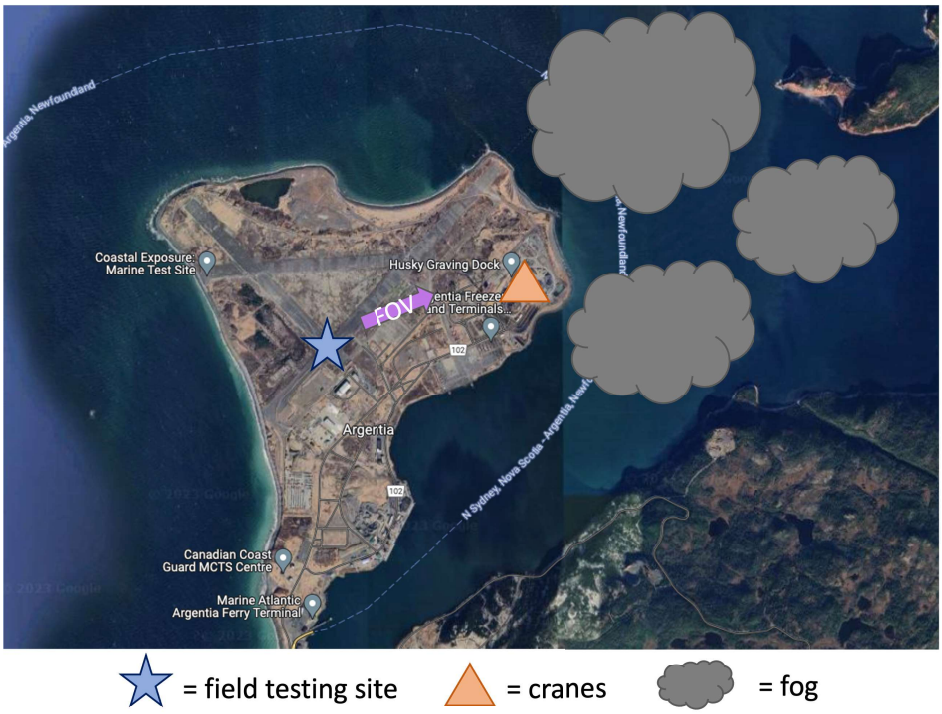

Figure 4.33: A google map overlay of the Argentia, NL field site to roughly determine where fog in Figure 4.32 is located. The blue star represents the field site, the orange triangle is the cranes, with fog most likely over the bay.

4.3.4 Field Testing - July 3, 2022

The successful run of night-time imagery from June 29, 2022 proved an excellent foundation for more night-time experiments. On July 3rd, 2022, fog rolled into the town of Placentia during the night, allowing more images to be captured. Since night-time imaging proved more successful than daytime imaging, both the class 3R and class 2 lasers were used. The case was also kept closed for these experiments. The experimental matrix for this night is shown in Table 4.10.

Table 4.10: Experimental matrix for July 3, 2022 night experiments. Based on the success of June 29, 2022 measurements, more lasers were included in this matrix.

			Laser in use, Wavelength [nm]				
Run Number	Laser Class	# of Frames	405	450 (3R only)	520	532 (2 only)	635
1	3R	10	x	x	x		x
2				x			
3							x
4					x		
5	2	10	x		x	x	x
6					x	x	
7	N/A	10	None - Background				

Figures 4.34-4.36 showcase the imagery and results from the July 3, 2022 experiments. Right away it was apparent that the class 3R lasers were less bright in comparison to June 29, 2022 imagery. When looking at the class 2 laser imagery, they were very dim as well and were difficult to distinguish in the images. This indicates that class 2 lasers may not be a good option for future MAPLE field experiments due to their low power. When analyzing the class 3R images in the same manner as June 29, 2022, more noise is shown in the Intensity graphs. The main difference between the two night-time experiments was the case being left open on June 29, 2022 but closed on July 3, 2022. The polycarbonate windows that were installed on MAPLE could be the cause of dimmer lasers and would be good to investigate further for future MAPLE experiments.

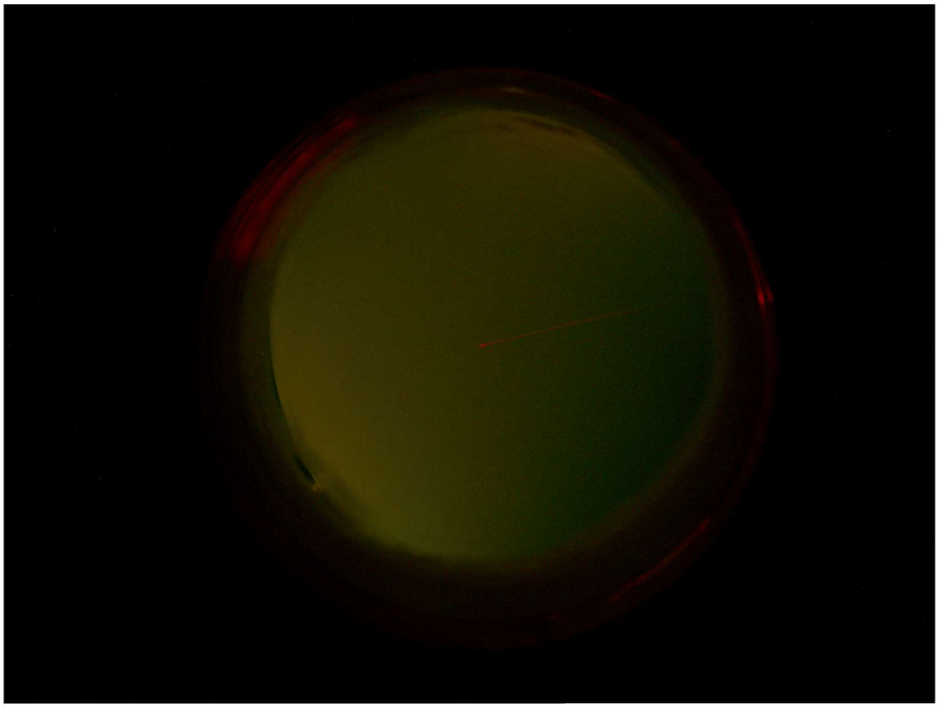

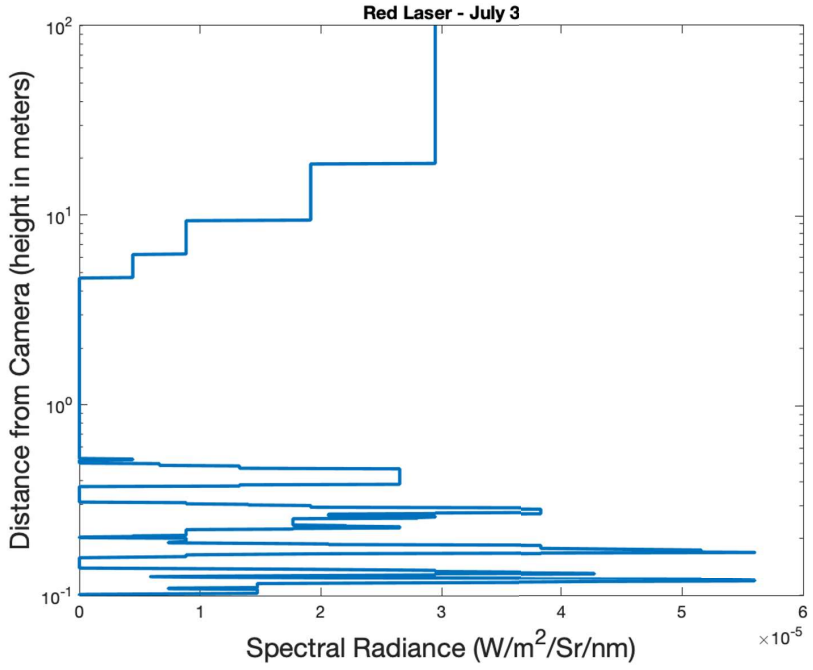

Figure 4.34: Top: The class 3R red laser being used during the night of July 3, 2022. Bottom: Normalized intensity as a function of distance from the camera is modelled based on the location of the laser in the top image. This night showed more noise compared to the June 29, 2022 experiments (Figure 4.20) and the laser was significantly less bright. The only change between the two days was the closing of the pelican case lid.

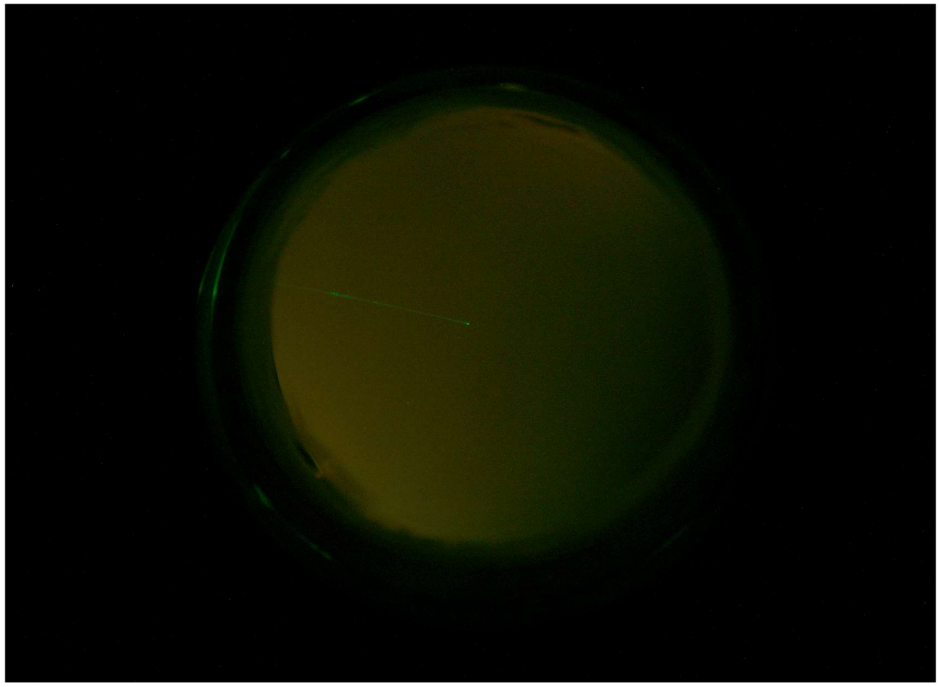

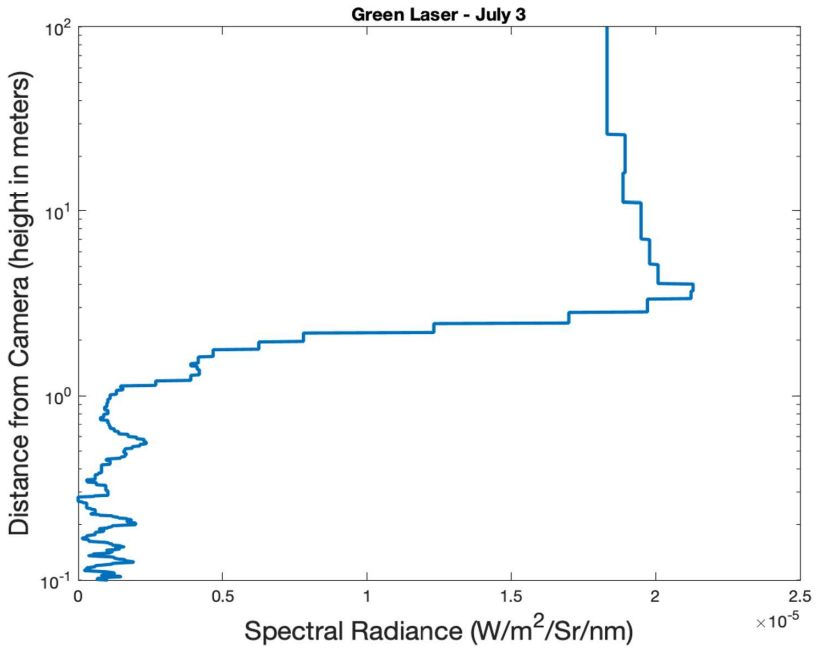

Figure 4.35: Similar to 4.34, but for the class 3R green laser. This example still had noise below 1 meter from the surface. A fog deck was measured 3 meters above MAPLE.

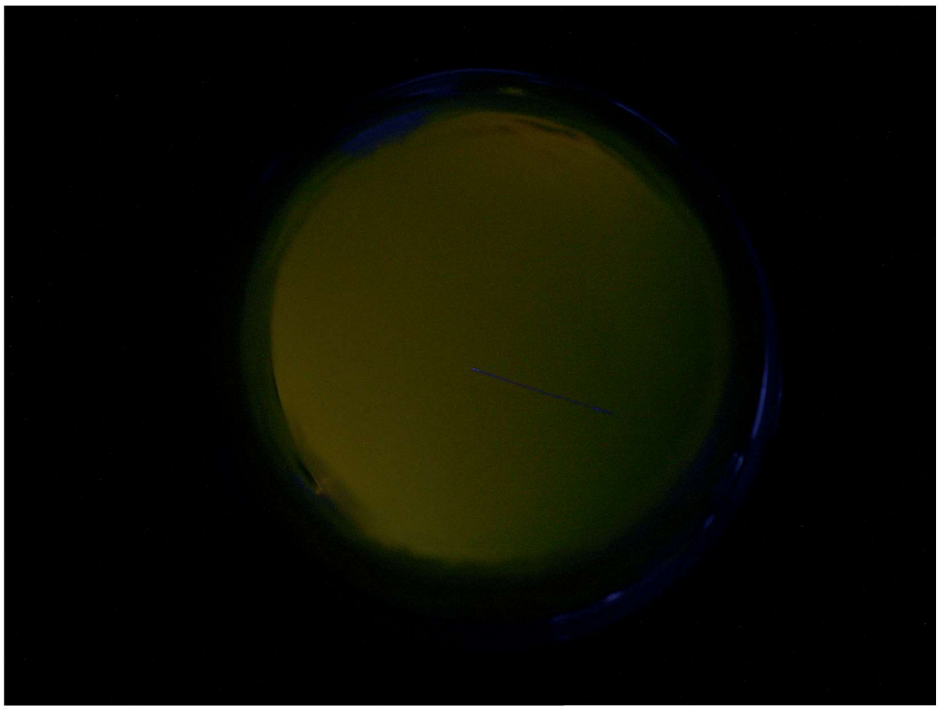

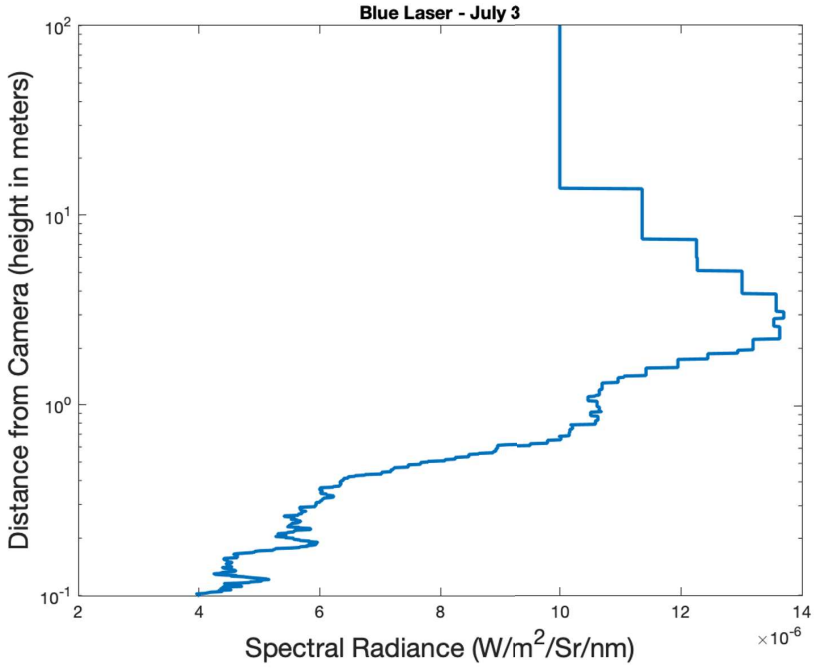

Figure 4.36: Similar to 4.34, but for the class 3R blue laser. Noise was still shown at altitudes close to the surface, yet a fog deck was still measureable at the same altitude as 4.35.

An analysis into the LWC was also done for this day in a similar manner as Section 4.3.2. The same set of figures (Spectral radiance, LWC, Optical depth and Transmittance) are shown in Figures 4.37-4.39. Unfortunately these graphs were unable to resolve any cloud decks in the LWC calculations and found the majority of the LWC to be at higher altitudes from the camera. This agreed with results from June 29, 2022 (Figures 4.24-4.25). The red laser results from both dates (Figure 4.23 and 4.37) both showed unreliable results which could be due to a couple of factors. The camera has an IR cutoff at 700 nm and thus transmittance of the red laser at 635 nm could be lower due to approaching the cutoff. Another factor is due to the spontaneous experiment of the nighttime measurements, we took our images within limits of a township and there is light pollution due to nearby streetlights. The orange tinge of these lights could be increasing scattering at those wavelengths and affecting how the camera images lasers near that similar wavelength. For a better verification on how MAPLE handles redder wavelengths, an environment with no light pollution would be best.

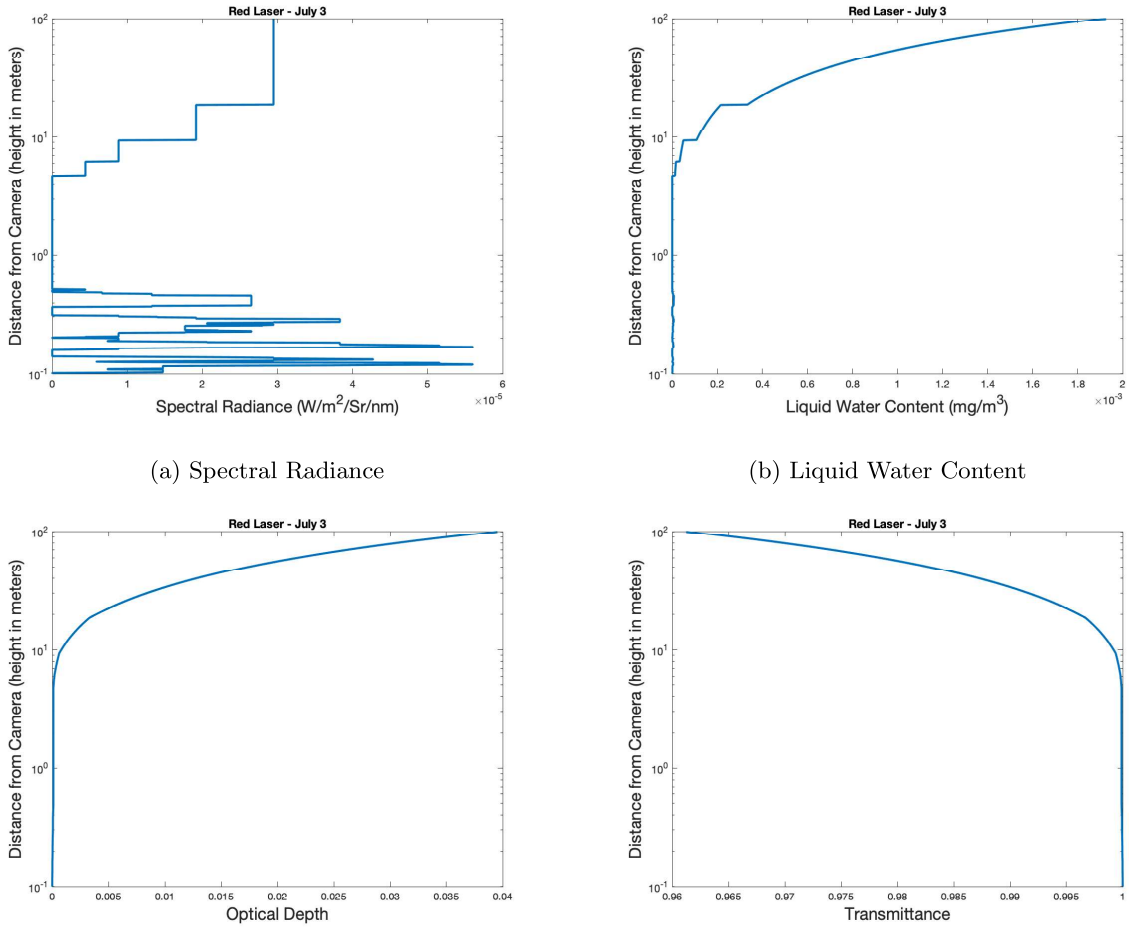

(a) Spectral Radiance

(b) Liquid Water Content

(c) Optical Depth

(d) Transmittance

Figure 4.37: Red laser LWC analysis with Spectral Radiance (a), Optical Depth (c), and Transmittance (d).

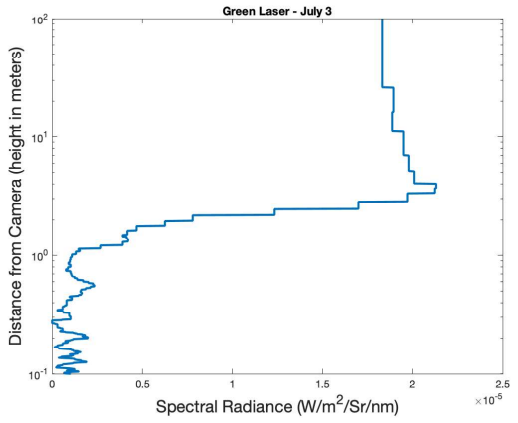

(a) Spectral Radiance

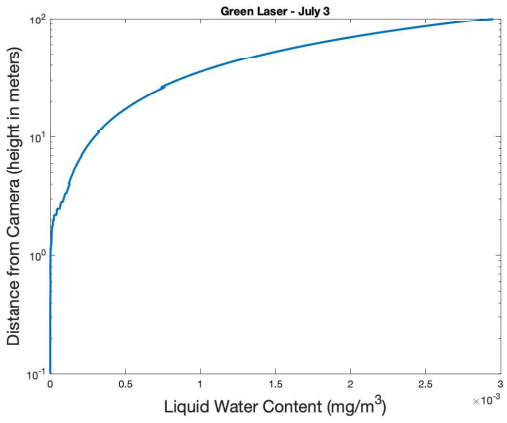

(b) Liquid Water Content

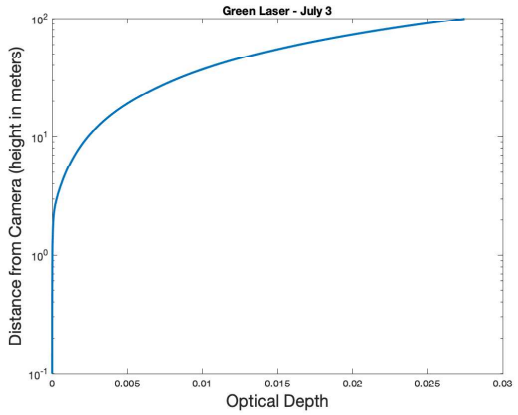

(c) Optical Depth

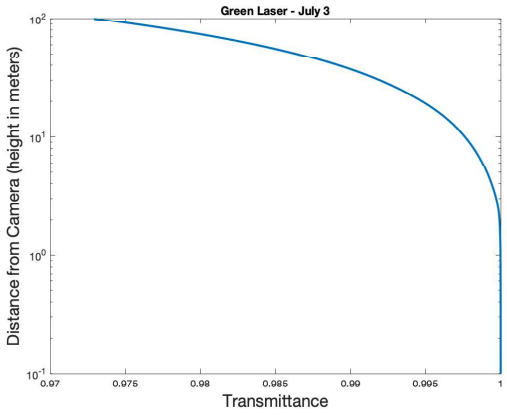

(d) Transmittance

Figure 4.38: Green laser LWC analysis with Spectral Radiance (a), Optical Depth (c), and Transmittance (d).

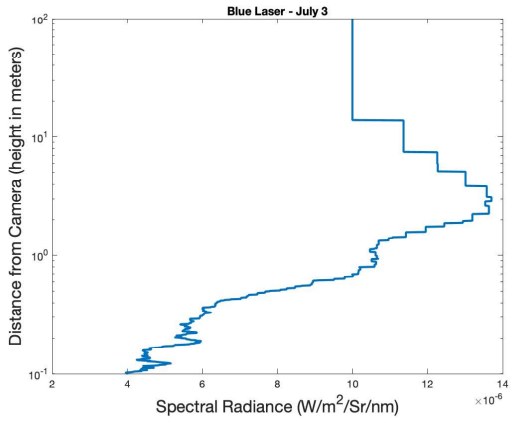

(a) Spectral Radiance

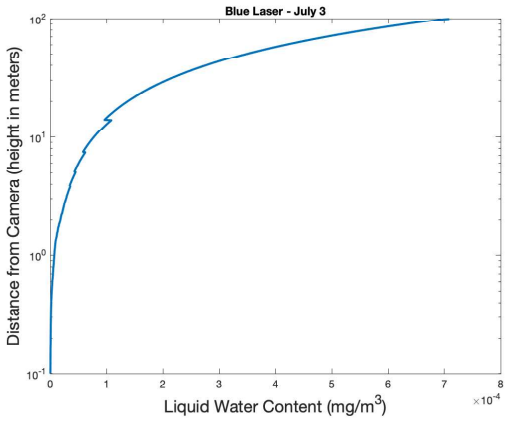

(b) Liquid Water Content

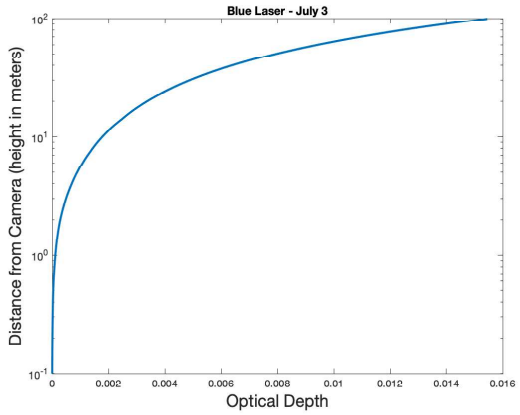

(c) Optical Depth

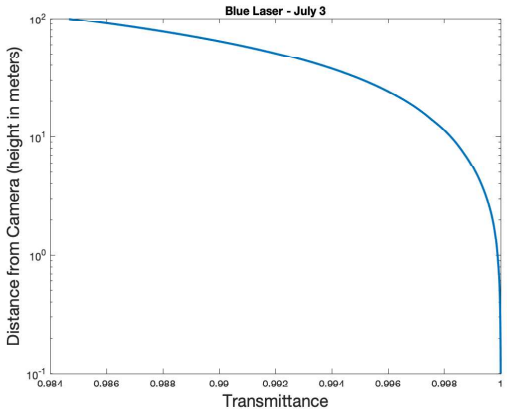

(d) Transmittance

Figure 4.39: Blue laser LWC analysis with Spectral Radiance (a), Optical Depth (c), and Transmittance (d).

4.3.5 Field Testing - July 4, 2022

Even though the two previous daytime experiments at the Argentia field site appeared to show null results, one last field day was planned due to the persistence of the thick fog from the night of July 3, 2022 into the morning of July 4, 2022. Both the Up and Side orientation were used with the class 3R lasers with a 500 microseconds exposure. The experimental matrix for this field day is shown in Table 4.11.

Table 4.11: Experimental matrix for July 4 daytime Argentia field site experiment. Both up and side orientation was used and background images were taken for both (run 1 and 10). Only the class 3R lasers were used to maximize the power within the fog to try to capture any scattering in the images.

				Laser in use, Wavelength [nm]				
Run Number	Laser Class	# of Frames	Orientation	405	450 (3R only)	520	532 (2 only)	635
1	N/A	10	Up	None - Background				
2	3R	10	Up		x	x		x
3	3R	10	Up			x		
4	3R	10	Up					x
5	3R	10	Up		x			
6	3R	10	Side		x	x		x
7	3R	10	Side			x		
8	3R	10	Side					x
9	3R	10	Side		x			
10	N/A	10	Side	None - Background				

Utilizing the same analysis procedure as June 30, 2022, background images were taken and subtracted to images with lasers in an effort to showcase any lasers. The background images are shown in Figure 4.40. Background-subtraction images and their corresponding run numbers are shown in the Up (Figure 4.41) and Side (Figure 4.42) orientations. The Sideways orientation did not appear to show any laser in subtracted

imagery, however, Figure 4.41 (top), shows a possible laser point in imagery in the Up, Green orientation. This was the only laser that produced a laser point in imagery which is promising. However, a lot more aerosols are still needed during daytime conditions to pull out the other lasers and produce a more defined green laser.

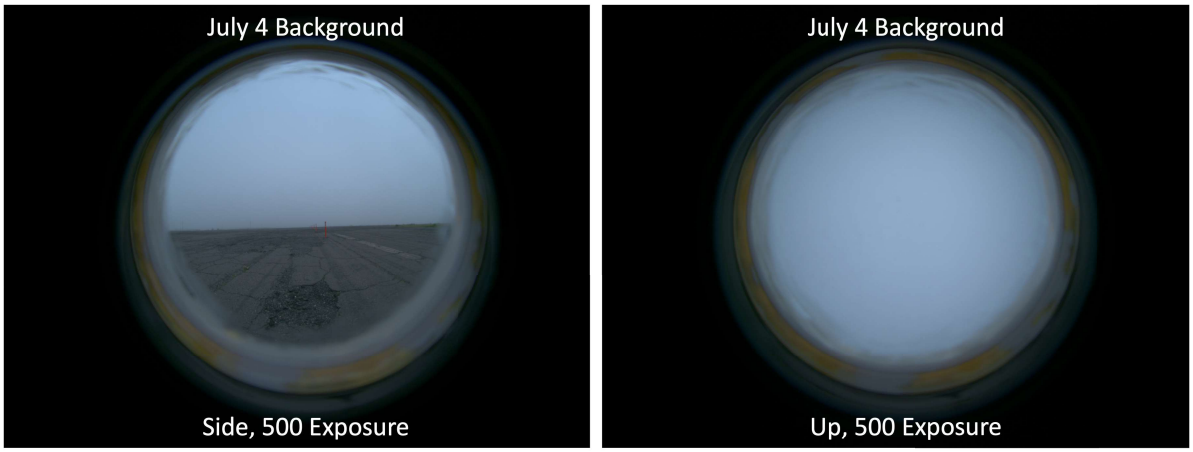

Figure 4.40: Background images taken in the Up and Side orientations for the July 4, 2022 Argentia daytime experiment.

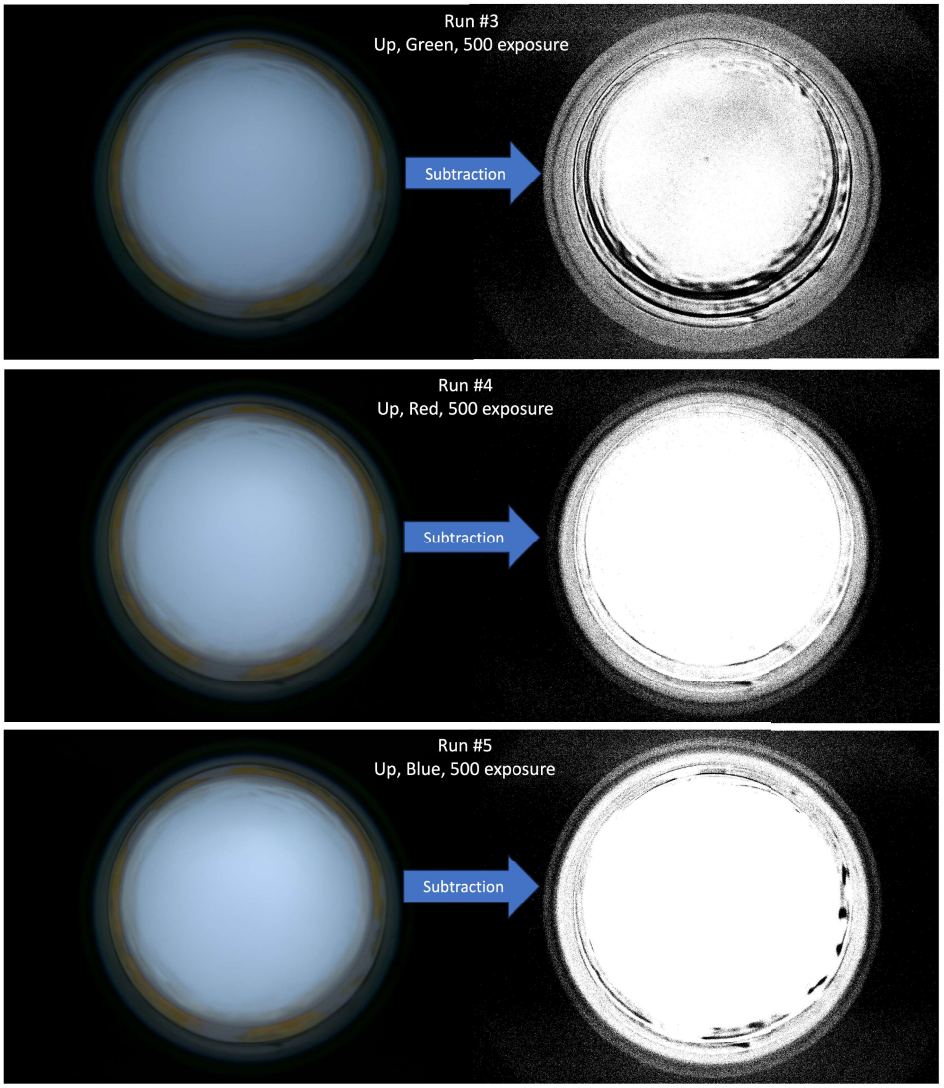

Figure 4.41: Raw (Left) and background-subtracted (Right) images for the runs laid out in Matrix 4.11. No laser beam was detected in any of the subtracted images, but a faint laser point is noticeable in the middle of the green, subtracted image (top). This day was foggier than the rest indicating that more aerosols on top of more power could be the solution to daytime measurements.

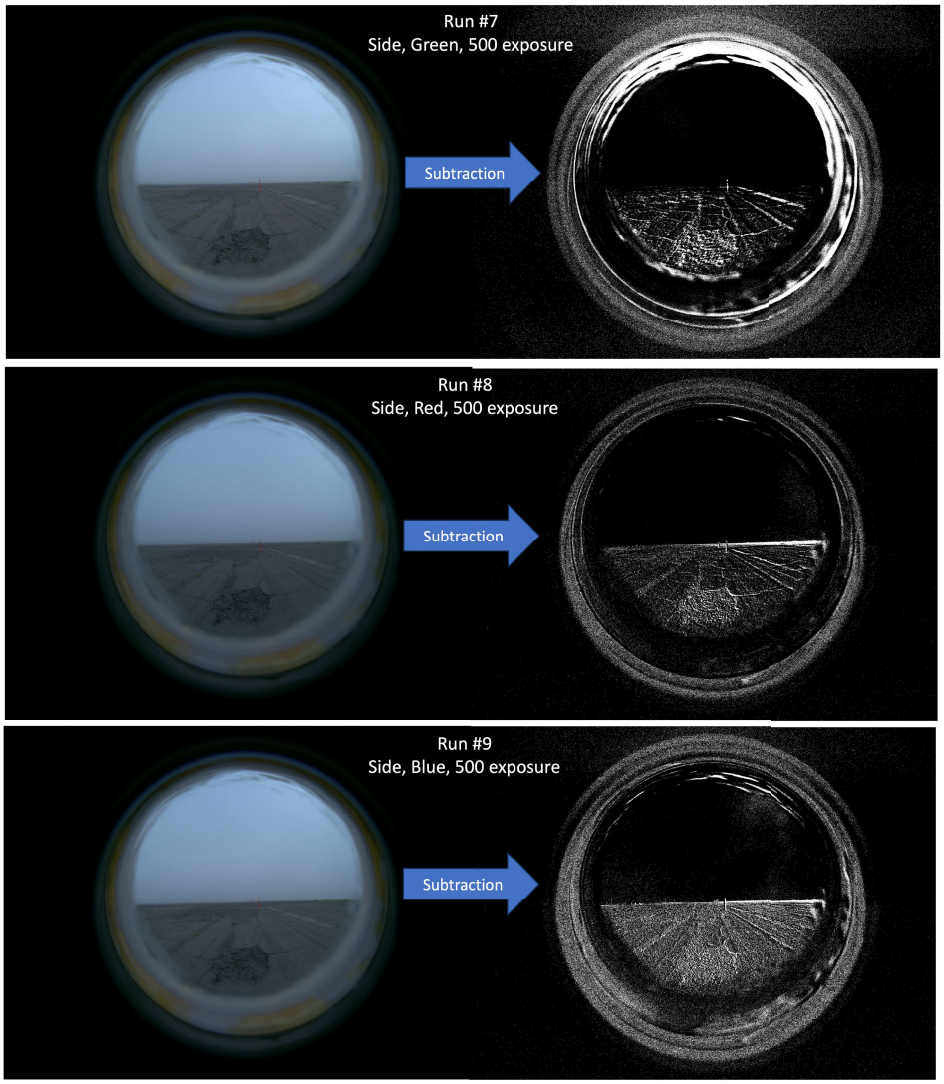

Figure 4.42: Similar to 4.41, but for the side orientation. No laser beam or points were deduced in these imagery which could be due to limited aerosols and/or too low power for the lasers.

4.3.6 Applying to Other Planetary Bodies

Based on field experiments from Newfoundland, MAPLE would need significant improvements before being deployed to another field site. However, we can still consider our preliminary results and what can it mean for other planetary bodies with condensable clouds. Good examples of other planets MAPLE could be applied to is Mars with water-ice clouds and Titan with methane clouds. Spectral radiance values have been

measured at both planets and can act as a starting point on the minimum radiance values needed to see the laser. To ensure that the laser would be visible in the varying conditions, we want our laser backscatter to be at least two times as powerful as any background radiance as seen by the camera. Working backwards based on found radiance values for Mars and Titan will let us determine what power the lasers need to be at to be visible by the MAPLE camera. Equation 4.13 highlights how the background and power of the laser will be used to determine a minimum laser strength for other planetary bodies. The conversion calculation based on Equation 4.1 is taken into account in Equation 4.13 which utilizes only radiance rather than spectral radiance.

$$\begin{aligned} (2 * (\frac{P_{laser}}{0.0001\text{m}^2 * \pi})) &= \text{Radiance} \\ \therefore P_{laser} &= \frac{\text{Radiance} \times 0.0001\text{m}^2 * \pi}{2} \end{aligned} \tag{4.13}$$

Equation 4.13 is used in three separate locations, Newfoundland daytime Mars and Titan. The background radiance from the Newfoundland night imagery is shown in Table 4.12 and represents the background portion of Equation 4.13. The Newfoundland daytime radiance is noted in Table 4.13. For Mars, Moores et al. (2011) measured average spectral radiance on multiple sols (example: Figure 2 in (Moores et al., 2011)) and can be used as a good starting position on what to expect for Mars. However, since those results are a spectral radiance then a 10 nm bandwidth is multiplied to convert back to radiance. A radiance value of 2E-05 was used for Mars from Moores et al. (2011). For Titan, Tomasko et al. (2005) measured spectral radiance at different altitudes above the surface (Figure 17). MAPLE would most likely be characterizing the lower part of the atmosphere that only the 5.5 km altitude is considered in Figure 17 from Tomasko et al. (2005). All three coloured lasers (red (635 nm), green (520 nm) and blue (450 nm)) were used to determine if the power changed significantly. Table 4.13 shows the results calculating the power needed for each coloured laser to be viewed at the environmental site.

Wavelength	**Background Radiance** ($W/m^2/Sr$)
Red (635 nm)	0.095
Green (520 nm)	0.831
Blue (450 nm)	0.601

Table 4.12: Background radiance as measured in the nighttime imagery on June 29, 2022. Since the lasers are visible in this imagery, these values can act as the background values in Equation 4.13 to measure the needed power for other planetary bodies or environments.

Environment	**Laser Wavelength**	**Radiance** ($W/m^2/Sr$)	**Power Needed (mW)**
Earth (NL) June 30 Day	Red (635 nm)	20.5	3.20
	Green (520 nm)	8.38	1.19
	Blue (450 nm)	5.73	0.81
Earth (NL) July 4 Day	Red (635 nm)	16.6	2.60
	Green (520 nm)	6.48	0.89
	Blue (450 nm)	4.04	0.54
Mars North Pole (Moores et al., 2011)	Red (635 nm)	2.00E-05	1.49E-02
	Green (520 nm)	2.00E-05	1.30E-01
	Blue (450 nm)	2.00E-05	9.44E-02
Titan (Tomasko et al., 2005)	Red (635 nm)	1.00E-02	0.013
	Green (520 nm)	7.00E-03	0.129
	Blue (450 nm)	5.00E-03	0.094

Table 4.13: The needed power for varying environments to ensure the different coloured (red, green, blue) lasers are seen against the background.

Investigating our results from Table 4.13 it appears that the daytime NL measurement need further

investigation. All the power values are lower than the lasers we used (4.5 mW) on the field which indicates they should have been visible in the imagery. However, none of the daytime imagery were able to deduce the laser, even when trying subtracting techniques. This indicates that a higher laser power is needed if being used on Earth in the day even though the calculation in Table 4.13 indicates otherwise. For results for Mars using Moores et al. (2011), low powered lasers could be possible at the Martian North pole. Red and Blue need the least amount of power, but all three could be considered and still be lower than the Phoenix lidar (40 W). Results for Titan show that low powered lasers could work in this kind of environment based on radiance from Tomasko et al. (2005).

Even though Table 4.13 indicates that MAPLE could be used on both Mars and Titan with lower powered lasers, more work should be done to clarify the math involved to ensure accurate results. The fact that the NL daytime values are lower than the ones used on the field site (4.5 mW) but were unable to be resolved in the imagery points to a further in-depth analysis needed to classify a minimum power for detection.

4.4 Conclusions

Field experiments done in Argentia, NL and Placentia, NL with MAPLE proved useful for determining minimum conditions for imaging low-cost lasers in a dense aerosol environment. A total of three day-time experiments were completed at the Argentia site, two night-time experiments at the Placentia (Hotel) site. All day-time experiments were unable to capture the lasers in imagery due to high background brightness within the fog due to increased scattering of sunlight. This led to impromptu night-time measurements that were able to resolve cloud decks above MAPLE using the class 3R lasers. Various lessons were learned from the experiments that can be used to expand MAPLE for further testing.

The biggest issue with our field site was more powerful lasers were needed for daytime imagery. The class 3R lasers performed well in night-time imagery but were not powerful enough for the day. The class 2 lasers were tested under night-time conditions but appeared to be too low powered to be identifiable in imagery. To expand the capabilities of MAPLE, higher powered lasers are required. This increases the power cost of MAPLE but would increase the number of measurements by including both day and night measurements.

To ensure MAPLE is low-cost, data volume must be considered. Each image from the Basler camera was 37MB each, enabling only 27 images for 1GB worth of data on the Raspberry Pi. This resulted in data constantly needing to be removed from the Raspberry Pi to make room for more experiments. Spacecraft memory relies on smaller values than due to their limited memory. For example, the Mars Science Laboratory (MSL) has only 2GB worth of flash memory, which is already eight times higher than the previous Mars Exploration Rover mission (NASA MSL website reference). Not only would be of interest on exploring how to compress imagery from the Basler camera but getting a larger SD card to enable larger onboard collection of images before needing to downlink onto a large hard drive for analysis.

More autonomy for the lasers and the camera would be useful for future field experiments. Current procedure requires the pelican case to be opened when changing lasers or transferring files from the Raspberry Pi. This could pose a risk for electronics within the case and inhibits MAPLE from being used remotely. The Basler camera used with MAPLE is also enabled to be fully coded via Python. This could be an explorable option to have MAPLE be fully remote while doing experiments. To further increase autonomy on MAPLE, the Onboard Rover Cloud Algorithm (ORCA) discussed in Chapter 3 could be implemented with the Basler camera since they both use Python. This would allow for the testing of ORCA with a dedicated meteorological station to determine how to improve ORCA for real-life settings.

Lastly, for future MAPLE field testing, better locations with more persistent foggy conditions could allow for a greater range of experiments to be completed. Fog would consistently dissolve before 10:00 on the tarmac but would still be visible in the bay for hours afterwards. It may be of interest to explore a boat as an option for MAPLE fog experiments to continue experiments for longer periods than on land. A good line-of-sight experiment could be set up on the coast pointing towards the ocean, however, safety has to be considered as higher class lasers would be needed for these experiments. Anything greater than class 3R becomes a significant eye hazard (Laser Safety Figure) and thus would be dangerous in any public areas. The Argentia port is so heavily used that it would have been unsafe to even use the class 3R lasers without a special permit. It would be of interest to find a good remote location to test MAPLE, such as utilizing a boat to navigate in foggy conditions or the high Arctic to capture Martian-like water-ice aerosols such as

diamond dust.

5 Future Work

5.1 Martian Aerosol Analysis with Surface Missions

To expand on work in Chapter 2, the continued analysis of wind direction and speed can be added to the current dataset to enable a longer look into wind behaviour over a Mars Year (MY). The Supra-Horizon Movie (SHM) taken by MSL could also be added for wind analysis as it is sunsafe midsol, which is a restricted time for the ZM due to its vertical pointing. This could add to dust wind analysis as midsol is the best time to capture dust activity.

Comparing the MSL and InSight data to data from other Mars missions, such as Perseverance, would allow further insight into the single cross-equatorial Hadley cell. With Perseverance and MSL operational at the same time, behaviour of water-ice clouds between the two landing sites could be compared and see if any seasonal patterns occur.

Another way to add to this Chapter would be to examine other Mars models (e.g. Neary and Daerden (2018), Spiga and Forget (2009) or Rafkin et al. (2001)) to see if results are the same or differ in comparison to the MarsWRF results. With the dust season very variable, it could be a good way to determine if aerosols observed during Perihelion are closer to the surface as dust clouds or above Aeolis Mons as possible water-ice clouds.

5.2 Investigating an Automated Analysis Approach for Aerosol Movement in Martian Surface Imagery

Chapter 3 can be expanded by testing ORCA with more MSL movies. The dataset from Campbell et al. (2020) only went up to MY 34 and thus movies from MY 35 and 36 could be added. ORCA also needs to be tested further to ignore common camera artifacts or lighting changes, which could expand its use for understand wind parameters in MSL movies.

Another parameter that could be implemented with ORCA is opacity from Kloos et al. (2016). This method takes the brightest and darkest spot of an image to calculate the opacity of observed aerosols. If ORCA could calculate this on top of wind parameters, it could be added for future missions and applied to any camera that can view the atmosphere, either Mars or another planetary body with condensable clouds.

5.3 Learning From Martian Surface Missions to Develop a Low-Cost Optical Meteorological Station

Expanding the Mars Panoramic camera and Laser Experiment (MAPLE) involves experimental studies within a lab to better characterize which lasers would be best for daytime observations. This can include simulating suspended aerosols in water to try to return particle size by shining the class 3R lasers into the water. This could also help understand if higher powered lasers would be better suited for MAPLE, especially with the polycarbonate windows that appear to dim the laser output.

It would be interesting to automate MAPLE more to ensure it could be fully remote while still returning atmospheric data. The Basler camera is fully functionable with Python programming and thus could be set up to take images at specific times or conditions. With ORCA also written in Python, combining these two projects would be a good way to test ORCA.

Lastly, taking MAPLE to a more Martian-like envrionment such as the high Arctic would best prepare MAPLE for Martian studies. The Arctic has diamond-dust ice particles that are similar to Mars water-ice particles, letting this location act as an analog Mars mission.

6 Conclusions

The Martian atmosphere has been studied using various methods to better understand various environmental parameters. Mars' exhibits two distinct seasons due to its high obliquity and ellipticity of its orbit. During Aphelion (furthest point from the Sun), cooler atmospheric temperatures allow for the formation of equatorial water-ice clouds known as the Aphelion Cloud Belt (ACB). The ACB is a consistently forming atmospheric phenomena (Clancy et al., 1996, Tamppari et al., 2003, Wang and Ingersoll, 2002) with a morning and afternoon diurnal pattern. On the other side of Mars' orbit during Perihelion, atmospheric temperatures are warmer, enabling dust lifting that can develop into dust devils and local, regional or global dust storms (Cantor, 2007, Cantor et al., 2001, Guzewich et al., 2019). These varying aerosols (water-ice and dust) can be studied at their respective seasons to understand local and regional atmospheric flow. Orbital data has the valuable advantage of studying the whole atmosphere at multiple locations, while surface vehicles can provide useful information on how local conditions affect surface-to-atmosphere interactions.

To fully understand the behaviour of the Martian atmosphere, both orbital and surface spacecraft must be considered. Orbiters are confined to observing the atmosphere above 10 km due to either obstructing terrain and thicker opacity associated with viewing the lower atmosphere (Kleinböhl et al., 2009). This restricts how much data can be returned about a vital part of the atmosphere and thus surface vehicles must be used. Previous missions such as the Phoenix lander (Moores et al., 2011) and Mars Science Laboratory (MSL) rover (Campbell et al., 2020, Cooper et al., 2019, Kloos et al., 2016; 2018, Moore et al., 2016, Moores et al., 2015b, Smith et al., 2020) demonstrated the importance of capturing local aerosol activity through cameras typically used for engineering purposes. However, mission operational constraints limits the number

of observations adding to the level of difficulty for acquiring surface Martian data. To limit gaps, Global Climate Models (GCMs) are used to simulate atmospheric conditions at various altitudes. However, GCMs also require Martian data for testing to validate the model is properly representing the environment. With 15-20 evenly spaced meteorological stations suggested as a minimum number for GCM verification (Haberle and Catling, 1996), more options for surface stations need to be explored for Mars. The goal of this dissertation is to examine Mars missions to determine advantages and limitations of camera-based observations and what can be done to expand these capabilities for Martian aerosol studies.

Five Mars Years (MYs) of atmospheric movies taken by MSL have been analyzed for wind movement as observed by aerosol movement. Wind directions within the ACB season showed strong Easterly winds that was also observed through movies taken at the InSight landing site, slightly north of MSL. This indicates that both sites are observing the same atmospheric flow, most likely caused by the strong cross-equatorial Hadley cell observed during Aphelion (Haberle et al., 1993). Within Perihelion, MSL movies showed more variable wind directions that could be attributed to dust at lower altitudes. However, atmospheric movies are taken less often during this season which could affect finding accurate wind results. Modelled wind results at varying altitudes above MSL's landing location, Gale Crater, was also included in this analysis for a further comparison. ACB wind directions from atmospheric movies seemed more likely at altitudes >20 km, further leading to aerosols being well above the crater to only be affected by large-scale circulation rather than the strong small-scale circulation measured near the surface by MSL (Newman et al., 2017, Viúdez-Moreiras et al., 2019). This agrees with previous altitude calculations for MSL (Campbell et al., 2020). The amount of information returned from the atmospheric dataset from MSL have been able to help understand equatorial water-ice cloud patterns, indicating the usefulness of these type of measurements. However, mission constraints such as data volume and frequency of observations do limit how much could be returned. Therefore it is of interest to determine if there is a low-cost way of using these movies to return the same wind analysis.

Using a set of previously analyzed atmospheric movies from MSL, an algorithm has been tested and determined to be a good stepping stone for an automated wind analysis. In collaboration with a team

at Curtin university, the Onboard Cloud Rover Algorithm (ORCA) incorporates Computer Vision and Machine Learning to measure wind direction and speed within a series of images. It was tested with data from Campbell et al. (2020) that measured wind movement from MSL atmospheric movies through manual methods. ORCA performed well with movies that had strong, consistent aerosol movement. Movies that had variable lighting conditions, camera artifacts or multiple cloud decks seemed to confuse ORCA and thus more training is needed for the algorithm to better recognize these features. If ORCA could be implemented on future missions with cameras, it could automatically calculate the wind direction and speed and simply return a string of values. This would be significantly less data than current methods that must downlink every image back to Earth before being analyzed by a human operator. Since data volume is a concern with every mission, ORCA could be a low-cost option to allow for more wind data to be returned, furthering our understanding of the Martian atmosphere.

The high cost associated with building, sending and landing spacecraft on the Martian surface has inhibited the ability to study how the lower atmosphere behaves from the surface. Some costs cannot be avoided yet others, such as complexity and size, can be explored to determine if a lower cost version would be a suitable solution for future missions. To do this, the Mars Atmospheric Panoramic camera and Laser Experiment (MAPLE) was created using a panoramic camera and multiple lasers to mimic observations previously done by the MSL and Phoenix missions. Phoenix showed that taking images of the onboard lidar shining through the atmosphere could return aerosol properties such as ice-water content (Moores et al., 2011). Class 3R continuous-wave lasers were utilized on MAPLE that had 10x less power than the Phoenix lidar and were still able to return the height of fog decks when tested in real-life conditions. Field site testing in Argentia, Newfoundland enabled an accessible setting in a dense aerosol environment. Even though the class 3R lasers had troubles being visible in imagery during the day, night time measurements showed promising results. However, more improvements are needed for MAPLE to further validate its usability as either a standalone optical meteorological station or a possible instrument on a larger mission.

Wind direction and speed have been successful measured using imagery from the Martian surface to help explain the behaviour of aloft aerosols in the Aphelion (water-ice) and Perihelion (dust) seasons. The

similarity of wind directions as seen by both MSL and InSight help point towards large-scale circulation being a significant factor on equatorial water-ice clouds. However, the limited amount of images returned for manual analysis indicates that lower cost options should be explored. Automation of wind analysis using ORCA was shown to be successful to reproduce wind direction and speed manually calculated for Martian movies with consistent movement. Further low-cost options were explored with MAPLE by showcasing the ability to measure the height of fog decks using lower powered class 3R lasers during nighttime foggy conditions with a panoramic camera. MAPLE highlights different parameters such as size and power that can become low-cost to maximize the amount of returnable science from a simple optical meteorological station.

Bibliography

(2019). HiRISE Views NASA's InSight and Curiosity on Mars - NASA. Section: The Solar System.

Anderson, R. (2010). Geologic mapping and characterization of Gale Crater and implications for its potential as a Mars Science Laboratory landing site. *The Mars Journal*, 5:76–128.

Appelbaum, J. and Flood, D. J. (1990). Solar radiation on Mars. *Solar Energy*, 45(6):353–363.

Balme, M. and Greeley, R. (2006). Dust devils on Earth and Mars. *Reviews of Geophysics*, 44(3). _eprint: https://onlinelibrary.wiley.com/doi/pdf/10.1029/2005RG000188.

Banerdt, W. B., Smrekar, S. E., Banfield, D., Giardini, D., Golombek, M., Johnson, C. L., Lognonné, P., Spiga, A., Spohn, T., Perrin, C., Stähler, S. C., Antonangeli, D., Asmar, S., Beghein, C., Bowles, N., Bozdag, E., Chi, P., Christensen, U., Clinton, J., Collins, G. S., Daubar, I., Dehant, V., Drilleau, M., Fillingim, M., Folkner, W., Garcia, R. F., Garvin, J., Grant, J., Grott, M., Grygorczuk, J., Hudson, T., Irving, J. C. E., Kargl, G., Kawamura, T., Kedar, S., King, S., Knapmeyer-Endrun, B., Knapmeyer, M., Lemmon, M., Lorenz, R., Maki, J. N., Margerin, L., McLennan, S. M., Michaut, C., Mimoun, D., Mittelholz, A., Mocquet, A., Morgan, P., Mueller, N. T., Murdoch, N., Nagihara, S., Newman, C., Nimmo, F., Panning, M., Pike, W. T., Plesa, A.-C., Rodriguez, S., Rodriguez-Manfredi, J. A., Russell, C. T., Schmerr, N., Siegler, M., Stanley, S., Stutzmann, E., Teanby, N., Tromp, J., van Driel, M., Warner, N., Weber, R., and Wieczorek, M. (2020). Initial results from the InSight mission on Mars. *Nature Geoscience*, 13(3):183–189. Number: 3 Publisher: Nature Publishing Group.

Banfield, D., Rodriguez-Manfredi, J. A., Russell, C. T., Rowe, K. M., Leneman, D., Lai, H. R., Cruce,

P. R., Means, J. D., Johnson, C. L., Mittelholz, A., Joy, S. P., Chi, P. J., Mikellides, I. G., Carpenter, S., Navarro, S., Sebastian, E., Gomez-Elvira, J., Torres, J., Mora, L., Peinado, V., Lepinette, A., Hurst, K., Lognonné, P., Smrekar, S. E., Banerdt, W. B., and The TWINS Team (2018). InSight Auxiliary Payload Sensor Suite (APSS). *Space Science Reviews*, 215(1):4.

BaslerAG (2023). acA4024-29uc.

Benson, J. L., Bonev, B. P., James, P. B., Shan, K. J., Cantor, B. A., and Caplinger, M. A. (2003). The seasonal behavior of water ice clouds in the Tharsis and Valles Marineris regions of Mars: Mars Orbiter Camera Observations. *Icarus*, 165:34–52. ADS Bibcode: 2003Icar..165...34B.

Campbell, C. L., Kling, A. M., Guzewich, S. D., Smith, C. L., Kloos, J. L., Lemmon, M. T., Moore, C. A., Cooper, B. A., Haberle, R. M., and Moores, J. E. (2020). Estimating the altitudes of Martian water-ice clouds above the Mars Science Laboratory rover landing site. *Planetary and Space Science*, 182:104785.

Campbell, C. L., Meka, S., Marrable, D., Rohl, A. L., Chai, K., Benedix, G. K., Smith, C. L., and Moores, J. E. (2021). A self-supervised learning based approach to analyze Martian water–ice cloud properties for planetary atmospheric applications. *Acta Astronautica*, 181:1–13.

Cantor, B. A. (2007). MOC observations of the 2001 Mars planet-encircling dust storm. *Icarus*, 186(1):60–96.

Cantor, B. A., James, P. B., Caplinger, M., and Wolff, M. J. (2001). Martian dust storms: 1999 Mars Orbiter Camera observations. *Journal of Geophysical Research: Planets*, 106(E10):23653–23687. _eprint: https://onlinelibrary.wiley.com/doi/pdf/10.1029/2000JE001310.

Choi, D. S., Banfield, D., Gierasch, P. J., and Showman, A. P. (2007). Velocity and Vorticity Measurements of Jupiter's Great Red Spot Using Automated Cloud Feature Tracking. *Icarus*, 188(1):35–46. arXiv:1301.6119 [astro-ph].

Clancy, R. T., Grossman, A. W., Wolff, M. J., James, P. B., Rudy, D. J., Billawala, Y. N., Sandor, B. J., Lee, S. W., and Muhleman, D. O. (1996). Water Vapor Saturation at Low Altitudes around Mars Aphelion: A Key to Mars Climate? *Icarus*, 122(1):36–62.

Clancy, R. T., Sandor, B. J., Wolff, M. J., Christensen, P. R., Smith, M. D., Pearl, J. C., Conrath, B. J., and Wilson, R. J. (2000). An intercomparison of ground-based millimeter, MGS TES, and Viking atmospheric temperature measurements: Seasonal and interannual variability of temperatures and dust loading in the global Mars atmosphere. *Journal of Geophysical Research: Planets*, 105(E4):9553–9571. _eprint: https://onlinelibrary.wiley.com/doi/pdf/10.1029/1999JE001089.

Cooper, B. A., Moores, J. E., Ellison, D. J., Kloos, J. L., Smith, C. L., Guzewich, S. D., and Campbell, C. L. (2019). Constraints on Mars Aphelion Cloud Belt phase function and ice crystal geometries. *Planetary and Space Science*, 168:62–72.

Cros, S., Sébastien, N., Liandrat, O., and Schmutz, N. (2014). Cloud pattern prediction from geostationary meteorological satellite images for solar energy forecasting. In *Remote Sensing of Clouds and the Atmosphere XIX; and Optics in Atmospheric Propagation and Adaptive Systems XVII*, volume 9242, page 924202. SPIE.

de Météorologie Dynamique, L. L. (2008). Martian Seasons and Solar Longitude Ls.

Facts, L. S. (2023). Laser classification table - Laser Safety Facts.

Forget, F., Hourdin, F., Fournier, R., Hourdin, C., Talagrand, O., Collins, M., Lewis, S. R., Read, P. L., and Huot, J.-P. (1999). Improved general circulation models of the Martian atmosphere from the surface to above 80 km. *Journal of Geophysical Research: Planets*, 104(E10):24155–24175. _eprint: https://onlinelibrary.wiley.com/doi/pdf/10.1029/1999JE001025.

Francis, R., Moores, J., McIsaac, K., Choi, D., and Osinski, G. (2014). Observations of wind direction by automated analysis of images from Mars and the MSL rover. *Acta Astronautica*, 94(2):776–783.

Golombek, M., Williams, N., Warner, N. H., Parker, T., Williams, M. G., Daubar, I., Calef, F., Grant, J., Bailey, P., Abarca, H., Deen, R., Ruoff, N., Maki, J., McEwen, A., Baugh, N., Block, K., Tamppari, L., Call, J., Ladewig, J., Stoltz, A., Weems, W. A., Mora-Sotomayor, L., Torres, J., Johnson, M., Kennedy, T., and Sklyanskiy, E. (2020). Location and Setting of the Mars InSight

Lander, Instruments, and Landing Site. *Earth and Space Science*, 7(10):e2020EA001248. _eprint: https://onlinelibrary.wiley.com/doi/pdf/10.1029/2020EA001248.

Grotzinger, J. P., Crisp, J., Vasavada, A. R., Anderson, R. C., Baker, C. J., Barry, R., Blake, D. F., Conrad, P., Edgett, K. S., Ferdowski, B., Gellert, R., Gilbert, J. B., Golombek, M., Gómez-Elvira, J., Hassler, D. M., Jandura, L., Litvak, M., Mahaffy, P., Maki, J., Meyer, M., Malin, M. C., Mitrofanov, I., Simmonds, J. J., Vaniman, D., Welch, R. V., and Wiens, R. C. (2012). Mars Science Laboratory Mission and Science Investigation. *Space Science Reviews*, 170(1):5–56.

Guzewich, S. D., Lemmon, M., Smith, C. L., Martínez, G., de Vicente-Retortillo, , Newman, C. E., Baker, M., Campbell, C., Cooper, B., Gómez-Elvira, J., Harri, A.-M., Hassler, D., Martin-Torres, F. J., McConnochie, T., Moores, J. E., Kahanpää, H., Khayat, A., Richardson, M. I., Smith, M. D., Sullivan, R., de la Torre Juarez, M., Vasavada, A. R., Viúdez-Moreiras, D., Zeitlin, C., and Zorzano Mier, M.-P. (2019). Mars Science Laboratory Observations of the 2018/Mars Year 34 Global Dust Storm. *Geophysical Research Letters*, 46(1):71–79. _eprint: https://onlinelibrary.wiley.com/doi/pdf/10.1029/2018GL080839.

Gómez-Elvira, J., Armiens, C., Carrasco, I., Genzer, M., Gómez, F., Haberle, R., Hamilton, V. E., Harri, A.-M., Kahanpää, H., Kemppinen, O., Lepinette, A., Martín Soler, J., Martín-Torres, J., Martínez-Frías, J., Mischna, M., Mora, L., Navarro, S., Newman, C., de Pablo, M. A., Peinado, V., Polkko, J., Rafkin, S. C. R., Ramos, M., Rennó, N. O., Richardson, M., Rodríguez-Manfredi, J. A., Romeral Planelló, J. J., Sebastián, E., de la Torre Juárez, M., Torres, J., Urquí, R., Vasavada, A. R., Verdasca, J., and Zorzano, M.-P. (2014). Curiosity's rover environmental monitoring station: Overview of the first 100 sols. *Journal of Geophysical Research: Planets*, 119(7):1680–1688. _eprint: https://onlinelibrary.wiley.com/doi/pdf/10.1002/2013JE004576.

Haberle, R. M. (1997). MARS: ATMOSPHEREMars: Atmosphere. In *Encyclopedia of Planetary Science*, Encyclopedia of Earth Science, pages 432–441. Springer Netherlands, Dordrecht.

Haberle, R. M. (2003). PLANETARY ATMOSPHERES | Mars. In Holton, J. R., editor, *Encyclopedia of Atmospheric Sciences*, pages 1745–1755. Academic Press, Oxford.

Haberle, R. M. (2012). Meteorological predictions for the REMS experiment on MSL. *Mars J.*

Haberle, R. M. and Catling, D. C. (1996). A Micro-Meteorological mission for global network science on Mars: rationale and measurement requirements. *Planetary and Space Science*, 44(11):1361–1383.

Haberle, R. M., Clancy, R. T., Forget, F., Smith, M. D., and Zurek, R. W., editors (2017). *The Atmosphere and Climate of Mars*. Cambridge Planetary Science. Cambridge University Press, Cambridge.

Haberle, R. M., Gómez-Elvira, J., de la Torre Juárez, M., Harri, A.-M., Hollingsworth, J. L., Kahanpää, H., Kahre, M. A., Lemmon, M., Martín-Torres, F. J., Mischna, M., Moores, J. E., Newman, C., Rafkin, S. C. R., Rennó, N., Richardson, M. I., Rodríguez-Manfredi, J. A., Vasavada, A. R., Zorzano-Mier, M.-P., and Teams, R. S. (2014). Preliminary interpretation of the REMS pressure data from the first 100 sols of the MSL mission. *Journal of Geophysical Research: Planets*, 119(3):440–453. _eprint: https://onlinelibrary.wiley.com/doi/pdf/10.1002/2013JE004488.

Haberle, R. M., Pollack, J. B., Barnes, J. R., Zurek, R. W., Leovy, C. B., Murphy, J. R., Lee, H., and Schaeffer, J. (1993). Mars atmospheric dynamics as simulated by the NASA Ames General Circulation Model: 1. The zonal-mean circulation. *Journal of Geophysical Research: Planets*, 98(E2):3093–3123. _eprint: https://onlinelibrary.wiley.com/doi/pdf/10.1029/92JE02946.

Hinson, D. P., Simpson, R. A., Twicken, J. D., Tyler, G. L., and Flasar, F. M. (1999). Initial results from radio occultation measurements with Mars Global Surveyor. *Journal of Geophysical Research: Planets*, 104(E11):26997–27012. _eprint: https://onlinelibrary.wiley.com/doi/pdf/10.1029/1999JE001069.

Horinouchi, T., Murakami, S.-y., Kouyama, T., Ogohara, K., Yamazaki, A., Yamada, M., and Watanabe, S. (2017). Image velocimetry for clouds with relaxation labeling based on deformation consistency. *Measurement Science and Technology*, 28(8):085301. Publisher: IOP Publishing.

Jakosky, B. M. and Farmer, C. B. (1982). The seasonal and global behavior of water vapor in the Mars atmosphere: Complete global results of the Viking Atmospheric Water Detector Experiment. *Journal of Geophysical Research: Solid Earth*, 87(B4):2999–3019. _eprint: https://onlinelibrary.wiley.com/doi/pdf/10.1029/JB087iB04p02999.

Kahre, M. A., Murphy, J. R., and Haberle, R. M. (2006). Modeling the Martian dust cycle and surface dust reservoirs with the NASA Ames general circulation model. *Journal of Geophysical Research: Planets*, 111(E6). _eprint: https://onlinelibrary.wiley.com/doi/pdf/10.1029/2005JE002588.

Kelechava, B. (2023). ANSI Z136.1-2022: Safe Use of Lasers - ANSI Blog.

Kleinböhl, A., Schofield, J. T., Kass, D. M., Abdou, W. A., Backus, C. R., Sen, B., Shirley, J. H., Lawson, W. G., Richardson, M. I., Taylor, F. W., Teanby, N. A., and McCleese, D. J. (2009). Mars Climate Sounder limb profile retrieval of atmospheric temperature, pressure, and dust and water ice opacity. *Journal of Geophysical Research (Planets)*, 114:E10006. ADS Bibcode: 2009JGRE..11410006K.

Kloos, J. L., Moores, J. E., Lemmon, M., Kass, D., Francis, R., de la Torre Juárez, M., Zorzano, M.-P., and Martín-Torres, F. J. (2016). The first Martian year of cloud activity from Mars Science Laboratory (sol 0–800). *Advances in Space Research*, 57(5):1223–1240.

Kloos, J. L., Moores, J. E., Whiteway, J. A., and Aggarwal, M. (2018). Interannual and Diurnal Variability in Water Ice Clouds Observed from MSL Over Two Martian Years. *Journal of Geophysical Research (Planets)*, 123:233–245. ADS Bibcode: 2018JGRE..123..233K.

Lemmon, M., Guzewich, S., Battalio, J., Malin, M., Vicente-Retortillo, A., Zorzano, M.-P., Martín-Torres, J., Sullivan, R., Maki, J., Smith, M., and Bell, J. (2024). The Mars Science Laboratory record of optical depth measurements via solar imaging. *Icarus*, 408:115821.

Lemmon, M. T., Smith, P. H., Shinohara, C., Tanner, R., Woida, P., Shaw, A., Hughes, J., Reynolds, R., Woida, R., Penegor, J., Oquest, C., Hviid, S. F., Madsen, M. B., Olsen, M., Leer, K., Drube, L., Morris,

R. V., and Britt, D. T. (2008). The Phoenix Surface Stereo Imager (SSI) Investigation. page 2156. Conference Name: 39th Annual Lunar and Planetary Science Conference ADS Bibcode: 2008LPI....39.2156L.

Lemmon, M. T., Toledo, D., Apestigue, V., Arruego, I., Wolff, M. J., Patel, P., Guzewich, S., Colaprete, A., Vicente-Retortillo, , Tamppari, L., Montmessin, F., De La Torre Juarez, M., Maki, J., McConnochie, T., Brown, A., and Bell, J. F. (2022). Hexagonal Prisms Form in Water-Ice Clouds on Mars, Producing Halo Displays Seen by Perseverance Rover. *Geophysical Research Letters*, 49(17):e2022GL099776.

Lemmon, M. T., Wolff, M. J., Bell, J. F., Smith, M. D., Cantor, B. A., and Smith, P. H. (2015). Dust aerosol, clouds, and the atmospheric optical depth record over 5 Mars years of the Mars Exploration Rover mission. *Icarus*, 251:96–111.

Lorenz, R. D., Nakamura, Y., and Murphy, J. R. (2017). Viking-2 Seismometer Measurements on Mars: PDS Data Archive and Meteorological Applications. *Earth and Space Science*, 4(11):681–688. _eprint: https://onlinelibrary.wiley.com/doi/pdf/10.1002/2017EA000306.

Maki, J., Thiessen, D., Pourangi, A., Kobzeff, P., Litwin, T., Scherr, L., Elliott, S., Dingizian, A., and Maimone, M. (2012). The Mars Science Laboratory Engineering Cameras. *Space Science Reviews*, 170(1):77–93.

Maki, J. N., Bell III, J. F., Herkenhoff, K. E., Squyres, S. W., Kiely, A., Klimesh, M., Schwochert, M., Litwin, T., Willson, R., Johnson, A., Maimone, M., Baumgartner, E., Collins, A., Wadsworth, M., Elliot, S. T., Dingizian, A., Brown, D., Hagerott, E. C., Scherr, L., Deen, R., Alexander, D., and Lorre, J. (2003). Mars Exploration Rover Engineering Cameras. *Journal of Geophysical Research: Planets*, 108(E12). _eprint: https://onlinelibrary.wiley.com/doi/pdf/10.1029/2003JE002077.

Maki, J. N., Golombek, M., Deen, R., Abarca, H., Sorice, C., Goodsall, T., Schwochert, M., Lemmon, M., Trebi-Ollennu, A., and Banerdt, W. B. (2018). The Color Cameras on the InSight Lander. *Space Science Reviews*, 214(6):105.

Maki, J. N., Gruel, D., McKinney, C., Ravine, M. A., Morales, M., Lee, D., Willson, R., Copley-Woods, D., Valvo, M., Goodsall, T., McGuire, J., Sellar, R. G., Schaffner, J. A., Caplinger, M. A., Shamah, J. M., Johnson, A. E., Ansari, H., Singh, K., Litwin, T., Deen, R., Culver, A., Ruoff, N., Petrizzo, D., Kessler, D., Basset, C., Estlin, T., Alibay, F., Nelessen, A., and Algermissen, S. (2020). The Mars 2020 Engineering Cameras and Microphone on the Perseverance Rover: A Next-Generation Imaging System for Mars Exploration. *Space Science Reviews*, 216(8):137.

Malin, M. C. and Edgett, K. S. (2001). Mars Global Surveyor Mars Orbiter Camera: Interplanetary cruise through primary mission. *Journal of Geophysical Research: Planets*, 106(E10):23429–23570. _eprint: https://onlinelibrary.wiley.com/doi/pdf/10.1029/2000JE001455.

Martin, L. J. and Zurek, R. W. (1993). An analysis of the history of dust activity on Mars. *Journal of Geophysical Research: Planets*, 98(E2):3221–3246. _eprint: https://onlinelibrary.wiley.com/doi/pdf/10.1029/92JE02937.

Meyer, M. B., Jiusto, J. E., and Lala, G. G. (1980). Measurements of Visual Range and Radiation-Fog (Haze) Microphysics. *Journal of the Atmospheric Sciences*, 37(3):622–629.

Moore, C. A., Moores, J. E., Lemmon, M. T., Rafkin, S. C. R., Francis, R., Pla-García, J., Haberle, R. M., Zorzano, M.-P., Martín-Torres, F. J., and Burton, J. R. (2016). A full martian year of line-of-sight extinction within Gale Crater, Mars as acquired by the MSL Navcam through sol 900. *Icarus*, 264:102–108.

Moores, J. E., Komguem, L., Whiteway, J. A., Lemmon, M. T., Dickinson, C., and Daerden, F. (2011). Observations of near-surface fog at the Phoenix Mars landing site. *Geophysical Research Letters*, 38(4). _eprint: https://onlinelibrary.wiley.com/doi/pdf/10.1029/2010GL046315.

Moores, J. E., Lemmon, M. T., Kahanpää, H., Rafkin, S. C. R., Francis, R., Pla-Garcia, J., Bean, K., Haberle, R., Newman, C., Mischna, M., Vasavada, A. R., de la Torre Juárez, M., Rennó, N., Bell, J., Calef, F., Cantor, B., Mcconnochie, T. H., Harri, A.-M., Genzer, M., Wong, M. H., Smith, M. D., Martín-Torres, F. J., Zorzano, M.-P., Kemppinen, O., and McCullough, E. (2015a). Observational evidence of a

suppressed planetary boundary layer in northern Gale Crater, Mars as seen by the Navcam instrument onboard the Mars Science Laboratory rover. *Icarus*, 249:129–142.

Moores, J. E., Lemmon, M. T., Rafkin, S. C. R., Francis, R., Pla-Garcia, J., de la Torre Juárez, M., Bean, K., Kass, D., Haberle, R., Newman, C., Mischna, M., Vasavada, A., Rennó, N., Bell, J., Calef, F., Cantor, B., Mcconnochie, T. H., Harri, A.-M., Genzer, M., Wong, M., Smith, M. D., Javier Martín-Torres, F., Zorzano, M.-P., Kemppinen, O., and McCullough, E. (2015b). Atmospheric movies acquired at the Mars Science Laboratory landing site: Cloud morphology, frequency and significance to the Gale Crater water cycle and Phoenix mission results. *Advances in Space Research*, 55(9):2217–2238.

Neary, L. and Daerden, F. (2018). The GEM-Mars general circulation model for Mars: Description and evaluation. *Icarus*, 300:458–476.

Newman, C. E., Gómez-Elvira, J., Marin, M., Navarro, S., Torres, J., Richardson, M. I., Battalio, J. M., Guzewich, S. D., Sullivan, R., Torre, M. d. l., Vasavada, A. R., and Bridges, N. T. (2017). Winds measured by the Rover Environmental Monitoring Station (REMS) during the Mars Science Laboratory (MSL) rover's Bagnold Dunes Campaign and comparison with numerical modeling using MarsWRF. *Icarus*, 291:203–231.

Newman, C. E., Lewis, S. R., Read, P. L., and Forget, F. (2002). Modeling the Martian dust cycle, 1. Representations of dust transport processes. *Journal of Geophysical Research: Planets*, 107(E12):6–1–6–18. _eprint: https://onlinelibrary.wiley.com/doi/pdf/10.1029/2002JE001910.

Pelican (2023). 1450 Protector Case.

Pitt, J. E. and Pitt., R. D. (2015). Argentia | The Canadian Encyclopedia.

Pla-Garcia, J., Rafkin, S. C. R., Kahre, M., Gomez-Elvira, J., Hamilton, V. E., Navarro, S., Torres, J., Marín, M., and R. Vasavada, A. (2016). The meteorology of Gale crater as determined from rover environmental monitoring station observations and numerical modeling. Part I: Comparison of model simulations with observations. *Icarus*, 280:103–113.

Rafkin, S. C. R., Haberle, R. M., and Michaels, T. I. (2001). The Mars Regional Atmospheric Modeling System: Model Description and Selected Simulations. *Icarus*, 151(2):228–256.

Rafkin, S. C. R., Pla-Garcia, J., Kahre, M., Gomez-Elvira, J., Hamilton, V. E., Marín, M., Navarro, S., Torres, J., and Vasavada, A. (2016). The meteorology of Gale Crater as determined from Rover Environmental Monitoring Station observations and numerical modeling. Part II: Interpretation. *Icarus*, 280:114–138.

Richardson, M. I., Toigo, A. D., and Newman, C. E. (2007). PlanetWRF: A general purpose, local to global numerical model for planetary atmospheric and climate dynamics. *Journal of Geophysical Research: Planets*, 112(E9). _eprint: https://onlinelibrary.wiley.com/doi/pdf/10.1029/2006JE002825.

Richardson, M. I. and Wilson, R. J. (2002). A topographically forced asymmetry in the martian circulation and climate. *Nature*, 416(6878):298–301. Number: 6878 Publisher: Nature Publishing Group.

Rodriguez-Manfredi, J. A., de la Torre Juárez, M., Alonso, A., Apéstigue, V., Arruego, I., Atienza, T., Banfield, D., Boland, J., Carrera, M. A., Castañer, L., Ceballos, J., Chen-Chen, H., Cobos, A., Conrad, P. G., Cordoba, E., del Río-Gaztelurrutia, T., de Vicente-Retortillo, A., Domínguez-Pumar, M., Espejo, S., Fairen, A. G., Fernández-Palma, A., Ferrándiz, R., Ferri, F., Fischer, E., García-Manchado, A., García-Villadangos, M., Genzer, M., Giménez, S., Gómez-Elvira, J., Gómez, F., Guzewich, S. D., Harri, A.-M., Hernández, C. D., Hieta, M., Hueso, R., Jaakonaho, I., Jiménez, J. J., Jiménez, V., Larman, A., Leiter, R., Lepinette, A., Lemmon, M. T., López, G., Madsen, S. N., Mäkinen, T., Marín, M., Martín-Soler, J., Martínez, G., Molina, A., Mora-Sotomayor, L., Moreno-Álvarez, J. F., Navarro, S., Newman, C. E., Ortega, C., Parrondo, M. C., Peinado, V., Peña, A., Pérez-Grande, I., Pérez-Hoyos, S., Pla-García, J., Polkko, J., Postigo, M., Prieto-Ballesteros, O., Rafkin, S. C. R., Ramos, M., Richardson, M. I., Romeral, J., Romero, C., Runyon, K. D., Saiz-Lopez, A., Sánchez-Lavega, A., Sard, I., Schofield, J. T., Sebastian, E., Smith, M. D., Sullivan, R. J., Tamppari, L. K., Thompson, A. D., Toledo, D., Torrero, F., Torres, J., Urquí, R., Velasco, T., Viúdez-Moreiras, D., Zurita, S., and The MEDA team (2021). The Mars Environmental Dynamics Analyzer, MEDA. A Suite of Environmental Sensors for the Mars 2020 Mission. *Space Science Reviews*, 217(3):48.

Schofield, J. T., Barnes, J. R., Crisp, D., Haberle, R. M., Larsen, S., Magalhaes, J. A., Murphy, J. R., Seiff, A., and Wilson, G. (1997). The Mars Pathfinder Atmospheric Structure Investigation/Meteorology. *Science*, 278:1752. ADS Bibcode: 1997Sci...278.1752S.

Smith, C. L., Lemmon, M., Moores, J. E., Guzewich, S. D., McConnochie, T. H., Newman, C. E., Khayat, A. S. J., Battalio, M., Moore, C. A., and Ellison, D. (2020). The Line-of-Sight Extinction Record at Gale Crater as Observed by MSL's Mastcam and Navcam through 2,500 Sols. *Journal of Geophysical Research: Planets*, 125(11):e2020JE006465. _eprint: https://onlinelibrary.wiley.com/doi/pdf/10.1029/2020JE006465.

Smith, D. E., Zuber, M. T., Frey, H. V., Garvin, J. B., Head, J. W., Muhleman, D. O., Pettengill, G. H., Phillips, R. J., Solomon, S. C., Zwally, H. J., Banerdt, W. B., Duxbury, T. C., Golombek, M. P., Lemoine, F. G., Neumann, G. A., Rowlands, D. D., Aharonson, O., Ford, P. G., Ivanov, A. B., Johnson, C. L., McGovern, P. J., Abshire, J. B., Afzal, R. S., and Sun, X. (2001). Mars Orbiter Laser Altimeter: Experiment summary after the first year of global mapping of Mars. *Journal of Geophysical Research: Planets*, 106(E10):23689–23722. _eprint: https://onlinelibrary.wiley.com/doi/pdf/10.1029/2000JE001364.

Smith, M. D. (2004). Interannual variability in TES atmospheric observations of Mars during 1999–2003. *Icarus*, 167(1):148–165.

Smith, M. D., Wolff, M. J., Lemmon, M. T., Spanovich, N., Banfield, D., Budney, C. J., Clancy, R. T., Ghosh, A., Landis, G. A., Smith, P., Whitney, B., Christensen, P. R., and Squyres, S. W. (2004). First Atmospheric Science Results from the Mars Exploration Rovers Mini-TES. *Science*, 306(5702):1750–1753. Publisher: American Association for the Advancement of Science.

Smith, P. H., Bell, III, J. F., Bridges, N. T., Britt, D. T., Gaddis, L., Greeley, R., Keller, H. U., Herkenhoff, K. E., Jaumann, R., Johnson, J. R., Kirk, R. L., Lemmon, M., Maki, J. N., Malin, M. C., Murchie, S. L., Oberst, J., Parker, T. J., Reid, R. J., Sablotny, R., Soderblom, L. A., Stoker, C., Sullivan, R., Thomas, N.,

Tomasko, M. G., Ward, W., and Wegryn, E. (1997). Results from the Mars Pathfinder Camera. *Science*, 278:1758. ADS Bibcode: 1997Sci...278.1758S.

Spiga, A., Banfield, D., Teanby, N. A., Forget, F., Lucas, A., Kenda, B., Rodriguez Manfredi, J. A., Widmer-Schnidrig, R., Murdoch, N., Lemmon, M. T., Garcia, R. F., Martire, L., Karatekin, , Le Maistre, S., Van Hove, B., Dehant, V., Lognonné, P., Mueller, N., Lorenz, R., Mimoun, D., Rodriguez, S., Beucler, , Daubar, I., Golombek, M. P., Bertrand, T., Nishikawa, Y., Millour, E., Rolland, L., Brissaud, Q., Kawamura, T., Mocquet, A., Martin, R., Clinton, J., Stutzmann, , Spohn, T., Smrekar, S., and Banerdt, W. B. (2018). Atmospheric Science with InSight. *Space Science Reviews*, 214(7):109.

Spiga, A. and Forget, F. (2009). A new model to simulate the Martian mesoscale and microscale atmospheric circulation: Validation and first results. *Journal of Geophysical Research: Planets*, 114(E2). _eprint: https://onlinelibrary.wiley.com/doi/pdf/10.1029/2008JE003242.

Tamppari, L. K., Zurek, R. W., and Paige, D. A. (2003). Viking-era diurnal water-ice clouds. *Journal of Geophysical Research: Planets*, 108(E7). _eprint: https://onlinelibrary.wiley.com/doi/pdf/10.1029/2002JE001911.

Thomas, P. and Gierasch, P. J. (1985). Dust Devils on Mars. *Science*, 230(4722):175–177. Publisher: American Association for the Advancement of Science.

ThorLabs (2024). Pulsed Lasers, Introduction to Power and Energy Calculations.

Tillman, J. E., Johnson, N. C., Guttorp, P., and Percival, D. B. (1993). The Martian annual atmospheric pressure cycle: Years without great dust storms. *Journal of Geophysical Research: Planets*, 98(E6):10963–10971. _eprint: https://onlinelibrary.wiley.com/doi/pdf/10.1029/93JE01084.

Tomasko, M. G., Archinal, B., Becker, T., Bézard, B., Bushroe, M., Combes, M., Cook, D., Coustenis, A., De Bergh, C., Dafoe, L. E., Doose, L., Douté, S., Eibl, A., Engel, S., Gliem, F., Grieger, B., Holso, K., Howington-Kraus, E., Karkoschka, E., Keller, H. U., Kirk, R., Kramm, R., Küppers, M., Lanagan, P.,

Lellouch, E., Lemmon, M., Lunine, J., McFarlane, E., Moores, J., Prout, G. M., Rizk, B., Rosiek, M., Rueffer, P., Schröder, S. E., Schmitt, B., See, C., Smith, P., Soderblom, L., Thomas, N., and West, R. (2005). Rain, winds and haze during the Huygens probe's descent to Titan's surface. *Nature*, 438(7069):765–778.

Tyler, Jr., D. and Barnes, J. R. (2013). Mesoscale Modeling of the Circulation in the Gale Crater Region: An Investigation into the Complex Forcing of Convective Boundary Layer Depths. *International Journal of Mars Science and Exploration*, 8:58–77. ADS Bibcode: 2013IJMSE...8...58T.

Vasavada, A. R. (2022). Mission Overview and Scientific Contributions from the Mars Science Laboratory Curiosity Rover After Eight Years of Surface Operations. *Space Science Reviews*, 218(3):14.

Vasavada, A. R., Chen, A., Barnes, J. R., Burkhart, P. D., Cantor, B. A., Dwyer-Cianciolo, A. M., Fergason, R. L., Hinson, D. P., Justh, H. L., Kass, D. M., Lewis, S. R., Mischna, M. A., Murphy, J. R., Rafkin, S. C. R., Tyler, D., and Withers, P. G. (2012). Assessment of Environments for Mars Science Laboratory Entry, Descent, and Surface Operations. *Space Science Reviews*, 170(1):793–835.

Viúdez-Moreiras, D., Gómez-Elvira, J., Newman, C. E., Navarro, S., Marin, M., Torres, J., and de la Torre-Juárez, M. (2019). Gale surface wind characterization based on the Mars Science Laboratory REMS dataset. Part I: Wind retrieval and Gale's wind speeds and directions. *Icarus*, 319:909–925.

Wang, H. and Ingersoll, A. P. (2002). Martian clouds observed by Mars Global Surveyor Mars Orbiter Camera. *Journal of Geophysical Research: Planets*, 107(E10):8–1–8–16. _eprint: https://onlinelibrary.wiley.com/doi/pdf/10.1029/2001JE001815.

Whelley, P. L. and Greeley, R. (2008). The distribution of dust devil activity on Mars. *Journal of Geophysical Research: Planets*, 113(E7). _eprint: https://onlinelibrary.wiley.com/doi/pdf/10.1029/2007JE002966.

Whiteway, J., Daly, M., Carswell, A., Duck, T., Dickinson, C., Komguem, L., and Cook, C. (2008). Lidar on the Phoenix mission to Mars. *Journal of Geophysical Research: Planets*, 113(E3):2007JE003002.

Whiteway, J. A., Komguem, L., Dickinson, C., Cook, C., Illnicki, M., Seabrook, J., Popovici, V., Duck, T. J., Davy, R., Taylor, P. A., Pathak, J., Fisher, D., Carswell, A. I., Daly, M., Hipkin, V., Zent, A. P., Hecht,

M. H., Wood, S. E., Tamppari, L. K., Renno, N., Moores, J. E., Lemmon, M. T., Daerden, F., and Smith, P. H. (2009). Mars Water-Ice Clouds and Precipitation. *Science*, 325(5936):68–70. Publisher: American Association for the Advancement of Science.

Williams, D. (2023). Mars Fact Sheet.

Williams, D. (2024). Earth Fact Sheet.

Wolfe, C. A. and Lemmon, M. T. (2023). Using engineering cameras on mars rovers and landers to retrieve atmospheric dust optical depth. *Planetary and Space Science*, 235:105741.

Zaher, A., Thil, S., Nou, J., Traoré, A., and Grieu, S. (2017). Comparative study of algorithms for cloud motion estimation using sky-imaging data. *IFAC-PapersOnLine*, 50(1):5934–5939.